HETEROCTRUCTURES AND HYPERSPECTRAL MICROSCOPY OF LEAD HALIDE PEROVSKITE SEMICONDUCTORS

by

CHRIS R. ROY

A dissertation submitted in partial fulfillment of

the requirements for the degree of

DOCTOR OF PHILOSOPHY

(CHEMISTRY)

at the

UNIVERSITY OF WISCONSIN–MADISON

2024

Date of final oral examination: December 15th, 2023

The dissertation is approved by the following members of the Final Oral Committee:

Song Jin – Professor of Chemistry

John C. Wright – Professor of Chemistry

Robert J. Hamers – Professor of Chemistry

Randall H. Goldsmith – Professor of Chemistry

Acknowledgements

As I look over this all this work, I am struck by how many people have helped bring it to what it is here, and how many intangible lessons it must have taken to give me the persistence to complete it all.

I would first like to thank my primary advisor, Professor Song Jin, for his constant attention to and advocacy for my work. When I was choosing potential advisors, I thought you would help me grow as a student by pushing me toward goals and holding me to the facts of the matter. At times through my studies, that guess felt more accurate than I had prepared for, but even in the hardest moments, I felt that your critiques stemmed from your passion toward making my work the best that it could be. At the end of it, I certainly feel that I have grown thanks to your advice and support.

I thank my second advisor, Professor John Wright, for his endless enthusiasm and curiosity toward my work. It is refreshing to see someone with such intuitive questions about physical problems, and your encouragement of rigorous troubleshooting brought my work to a standard of quality that I can be proud of.

I would also like to extend my thanks to my third committee member, Professor Robert Hamers, for his consideration and feedback during the milestone examinations of my Ph.D. Your questions and feedback helped me develop a sense of how to communicate ideas to researchers beyond my immediate field. I also have Professor Randy Goldsmith to thank for taking the time under extraordinary circumstances to serve as a fourth committee member and for attending my defense.

I have other collaborators to thank as well, most of all Dr. Zihua Zhu at Pacific Northwest National Laboratory, without whom I would be scrambling for explanations of confusing spectroscopic data. Your expertise in ToF-SIMS has lent indispensable information to all three of my major works. I would also like to thank Professor Martin Zanni for the insightful collaborations we've had between our groups. I am thankful for Dr. Dan Kohler's ever-present technical help and advice in the Wright Group. The number of times you've patiently heard out some stupid idea I've had, only to follow with carefully considered, supportive feedback is remarkable. You set an example to all of what a professional, supportive, and capable teammate looks like.

I have many colleagues and alumni to thank from both of my research groups. From the Jin Group, I thank my mentors Dr. Lianna Dang, Dr. Dongxu Pan, Dr. Yuzhou Zhao and Dr. Matt Hautzinger. Lianna's friendliness and candid advice was a welcoming introduction to the group, and I also thank her for her wonderful corner desk. Dongxu and Matt showed me the ropes of halide perovskite synthesis, providing me with entertaining discussions of goings-on and potpourri along the way. Yuzhou will forever be recognized as the technical whiz of the Jin Group, and I have benefited greatly from his countless contraptions and his friendly advice. I would like to thank members of the perovskite subgroup who I've worked with closely. Kristel Forlano and Willa Mihalyi-Koch have both been adept learners of spectroscopic techniques and have taught me how to be a better learner through teaching. I am also grateful for the camaraderie we've had in our day-to-day life in the big office. I'm thankful for the many fellow students and alumni who I've had the pleasure of working with in the Jin Group, including Dr. Nitish Mathur, Dr. Hongyuan Sheng, Dr. David Roberts, Dr. Natalia Spitha, Dr. Ming-Yu Kuo, Dr. Jaeyong Park, Dr. Mandi Wang, Katelyn Michael, Emily Reasoner, Rui Wang, Yueai Lin, Jãán Andrews, Chris Triggs, Gerardo Quintana Cintron, Yareslie Cruz Rivera, Kaylin Xu, Anneke Moeller, Richard Botzoc,

Jalianet Román Matías, and Abayọmi Awoyọmi. Lastly, I'd like to thank my former colleague from my cohort Dr. Dominic Ross. You were a great friend in the early years of our time in graduate school. When we joined the same group I was happy to carry on the Jin Group tradition of the buddy system with you, and I am thankful for the advice you gave along the way as we grew together.

From the Wright Group, I would like to thank Dr. Darien Morrow, who was a mentor and a friend during my first couple years of grad school. I always enjoyed our discussions about science and life, and I look forward to seeing you again in my next chapter in Pittsburgh. I would like to thank David Lafayette and Jason Scheeler for our excellent discussions of spectroscopy, collaborations, nonsense, and beer. I would also like to thank Ryan McDonnell for his literary insights and Northeastern sensibilities. In a world of Midwesterners, it's refreshing to hear someone throw a friendly roasting into a conversation, and I hope we can engage in a (*almost* uncivil) Wawa vs. Sheetz debate when I return to Madison. I also have Wright Group colleagues and alumni to thank including Dr. Kyle Sunden, Dr. Kent Meyer, Kelson Oram, James Harris, and Peter Cruz Parrilla, for your considerate feedback and for keeping your laughs under your breath as they watch a materials chemist play spectroscopist.

Within the program, I have countless friends to thank. I do not think a Ph.D. would have been possible if I had not been surrounded by so many wonderful people every single day. I would like to thank the original occupants of "The Cove" in the (old) TA office for commiserating about course deadlines busy schedules during our first year – you know who you are. I would also like to thank my bike friends in the department, Dr. Zachary Armstrong, Dr. Eli Larson, Dr. Jake Melby, Dr. Sidney Dicke, Dr. Benson Anderson, and Dr. Trent Peters-Clark, for the miles and the smiles. I am thankful for the never-ending group of friends who were kind enough to host events and bring

people together, including Kathy Nickson, Dr. Gina Roesch, Lauren Ehehalt, John Pavek, Dr. Rebecca Schultz, Dr. Lydia Perkins, and Dr. Ryan Allen.

In my third year of graduate school, my life was made much better by moving in with some of my best friends. Dr. Dylan Holst, Dr. Nathan Loud, Dr. Daniel Salgueiro, and Dr. Jonas Widness have brought countless moments and laughs that will live with me forever. Special thanks to Jonas for sticking it out with me from the beginning, and special thanks to Nate for sticking it out with me to the end.

I also have my friends outside the department to thank. My undergraduate friends Marzbed Margossian, Justin Esiason, Eric Smith, and Gray Fisher have made me feel appreciated by keeping in touch and visiting, and I am looking forward to being slightly closer to home and seeing you all soon.

I have my partner, Susan Maloney, to thank for making every day of the past three years that much better. As you begin your own Ph.D. journey, I recognize how much your love and support have levelled my anxieties and driven me to continue in my academic journey, and I look forward to showing you the same love and support as you move toward an amazing future with me alongside you.

Most importantly, I have my parents, Jen and Rob, and my step-parents, Scot and Tammy, to thank for raising a healthy, proud, and grateful son. You've done more for me than I can probably remember to bring me to where I am today, but most importantly you fed the curiosities of a nerdy kid and allowed him to become a real scientist.

– Chris Roy, 2023-01-20, Madison, WI

Table of Contents

Table of Main Text Figures

Chapter 1 . Introduction

1.1. Lead Halide Perovskite Semiconductors for Next Generation Optoelectronics

Lead halide perovskites (LHPs) are a class of direct bandgap semiconductor materials that show promise to greatly advance optoelectronics – technologies that mediate interactions between electricity and light. LHPs as a class of materials are unified by an ABX_3 structural motif (A is a monovalent cation, B is a divalent metal – typically Pb or Sn, X is a halide), which crystallizes as a cubic network of corner-sharing $[BX_6]^{4-}$ octahedra. The metal halide network contains large cubic cavities known as A-sites, which are typically occupied by small monovalent cations like Cs, methylammonium, or formamidinium (Figure 1.1a). The LHP lattice can be subject to broad structural substitutions and alloying of all three lattice sites.[1,2] Alloying of halides in particular allows the continuous tuning of LHPs' band gaps across the entire visible spectrum and the facile preparation of optoelectronic materials that can interact with all visible wavelengths.[3]

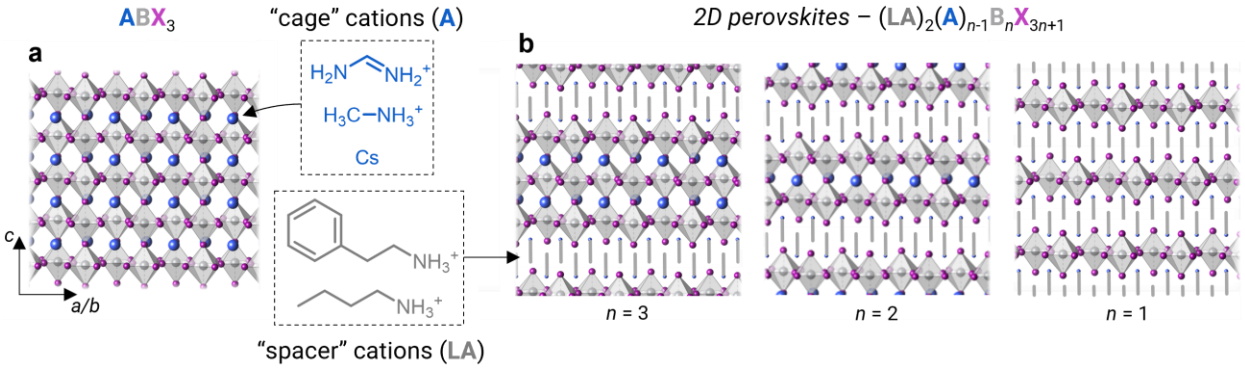

Figure 1.1. Halide perovskite semiconductors. **(a)** Perovskite structural motif. **(b)** A series of two-dimensional (2D) perovskite structures of different layer thickness (n).

A much broader family of structures is accessed when large monocations (LA) are substituted at the A-site, yielding layered two-dimensional (2D) LHPs with the formula $(LA)_2(A)_{n-1}Pb_nX_{3n+1}$.

In the 2D LHP structures, LA cations function as "spacers" separating isolated two-dimensional slabs of perovskite and transforming the $APbX_3$ lattice into a bulk multiple quantum wells structure (Figure 1.1b). 2D LHPs are among the most tunable semiconductor materials discovered to-date. Alongside the compositional flexibility inherited from 3D LHPs, there is an ever-expanding array of spacer cations that can template the perovskite sublattice, leading to electronic and structural distortions that can modulate band gap,[4] exciton binding energy,[5] emission bandwidth,[6] and optical non-linearity.[7,8] The exciton binding energy of the direct bandgap 2D LHPs can also be tuned over a range of 100s of meV by changing the thickness – and correspondingly the quantum confinement – of the perovskite layer, which is indexed in units of $[PbX_6]^{4-}$ octahedra by the stoichiometric coefficient n.[9,10]

LHPs gained enormous attention when they were first demonstrated as a light absorbing layer in a solar cell,[11] which have now approached record efficiencies and are on track to supplement established solar materials like Si.[12,13] Since then, 3D and 2D LHPs have also been successfully used in a variety of optoelectronic devices ranging from LEDs to lasers to ionizing radiation detectors.[14–16] A unique combination of physical characteristics lends LHPs the potential to outperform state-of-the-art materials in many optoelectronic devices. LHPs typically have high absorption coefficients,[17,18] high photoluminescence quantum yields,[19] long carrier propagation lengths,[20,21] and the ability to retain good performance characteristics in morphologies with high defect concentrations such as polycrystalline thin films – a property commonly referred to as "defect tolerance".[22,23]

Alongside LHPs' successes, there is no shortage of challenges facing the design of LHP devices. The most significant challenges center around LHPs chemical stability, which is compromised by multiple forms of ion migration and thermodynamic instabilities that lead to

degradation of LHP devices. Migration of A-site cations from LHPs can induce decomposition of the LHP material and degrade peripheral layers of devices,[24,25] whereas thermodynamic instability of halide alloys combine with facile ion mobility to induce the separation of homogeneous halide alloys into heterogeneous halide domains.[26,27] 2D LHPs have helped with these challenges, as the organic sublattice helps slow the migration of mobile ions in the LHP lattice and increase the formation energy of the 2D phases,[28,29] but developing a rational picture of the chemical behavior of 2D LHPs is made difficult by the many interfaces and microenvironments present in film-based devices incorporating 2D LHPs.

1.2. Interfaces of Two-Dimensional (2D) Lead Halide Perovskites

LHP devices are typically prepared as large-area thin films because their fabrication can be made cheap and scalable,[30] but the polycrystalline morphology of LHP thin films poses major challenges to device design. Grain boundaries,[31,32] localized defects,[33] and phase inhomogeneities can lead to adverse physical and chemical behavior that is detrimental to device performance.[34] Problems associated with film heterogeneity are compounded in 2D LHP films, which add an additional layer of complexity due to the possibility of varying *n* thickness. A central theme in the preparation of 2D LHP films is controlling *n*-phase purity,[35] as heterogeneous phase distributions in 2D LHP films can form local energy gradients that deviate global carrier transport in the device.[36] The propagation of carriers across heterogeneous 2D LHP materials is primarily governed by their band alignment, which is largely a function of *n*. A typical *n* series of 2D LHPs have a type-I (straddling) band alignment relative to its conjugate phases,[37] leading to funneling of charge carriers into the narrowest bandgap domains of 2D LHP films (Figure 1.2a, left). Type-II (staggered) band alignments are less common but also possible in interfaces with different metal

sites,[38] or through simultaneous modulation of X and *n*,[39] which shifts both band edges in a common direction.

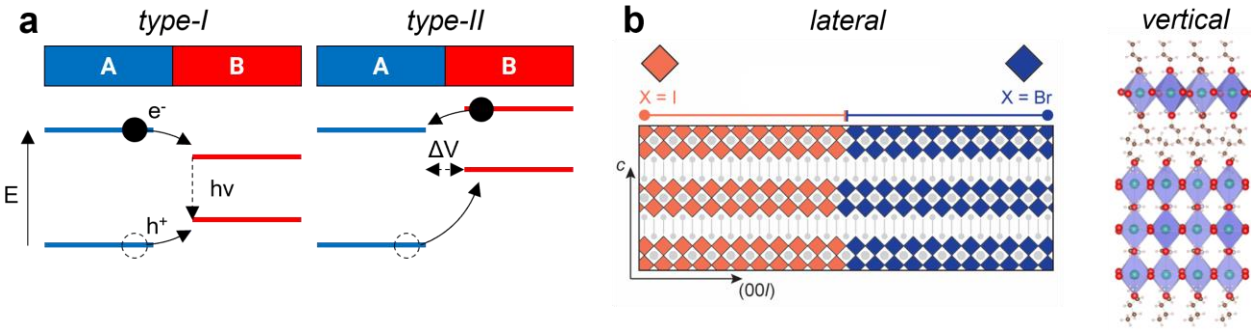

Figure 1.2. Band alignment and orientation of halide perovskite heterojunctions. **(a)** Comparison of type-I vs type-II band alignments facilitating carrier recombination or carrier separation (recombination, LEDs, lasers) (rectification, photovoltaics, sensors). **(b)** Lattice depictions of lateral vs vertical heterojunctions.

The complexity of phase heterogeneity is compounded by the orientation of interfaces of 2D LHPs. The anisotropic structure of 2D LHPs means that two distinct interface orientations are possible (Figure 1.2b): "lateral" heterojunctions of 2D LHPs, which are bound along the layer planes,[38,40] and "vertical" heterojunctions that are arranged as a layer-by-layer stack.[39,41] The conductivity of 2D LHPs is highly anisotropic due to the insulating nature of the spacer cation, making the performance of optoelectronic devices highly dependent on layer orientation in the device architecture.[42] Poor control of orientation or phase in a 2D LHP device can make the origins of performance changes nebulous, and the microanalysis of LHP thin films is limited by the small length scale of certain inhomogeneities and the 3D heterogeneity of the polycrystalline matrix.

Furthermore, even when the morphology of LHP thin films is well-controlled, the chemical and structural landscape of many LHP films is difficult to disentangle using device and

macroscopic ensemble measurements alone. The polycrystalline matrix of a LHP thin film has distinct interfaces along all three spatial dimensions, and a very minor proportion of the matrix can ultimately govern the global behavior of a device.[33,34] While great progress has been made in understanding this matrix using an array of optical and electron microscopies, the exploration of morphologies beyond device-compatible films could be useful to enhance the understanding of the underlying interfaces that drive LHP devices.

1.3. Deconstructing 2D Lead Halide Perovskite Interfaces with Hyperspectral Microscopy

An alternative way to understand the driving mechanisms of LHP devices is to conceptually reconstruct them from their constituent interfaces. Monocrystalline and exactly oriented interfaces of 2D and 3D LHPs have been prepared via solution-phase epitaxy,[38,42] vapor deposition,[43,44] and mechanical assembly,[39] but such systems are typically not large enough to be integrated into a device and directly measured. Instead, proxies can be measured to gauge the potential performance of an equivalent interface within a device. Photoluminescence (PL) spectroscopy is an effective proxy for many device performance characteristics, as PL quantum yield directly translates to the efficiency of light-emitting devices, and the radiative recombination efficiency of a material is indirectly connected to the performance of light harvesting devices through detailed balance.[45,46] Transmittance and reflectance microscopies provide additional information on chemical composition by distinguishing the onsets of band edge absorption in different semiconductor materials. Additional methods like second harmonic generation are a sensitive probe of structure due to its distinct interaction mediated by the symmetry-governed second-order non-linear optical susceptibility ($\chi^{(2)}$). Combining measurements of these physical properties with the spatial resolution of a microscope allows the spatial structure of physical properties to be visualized.

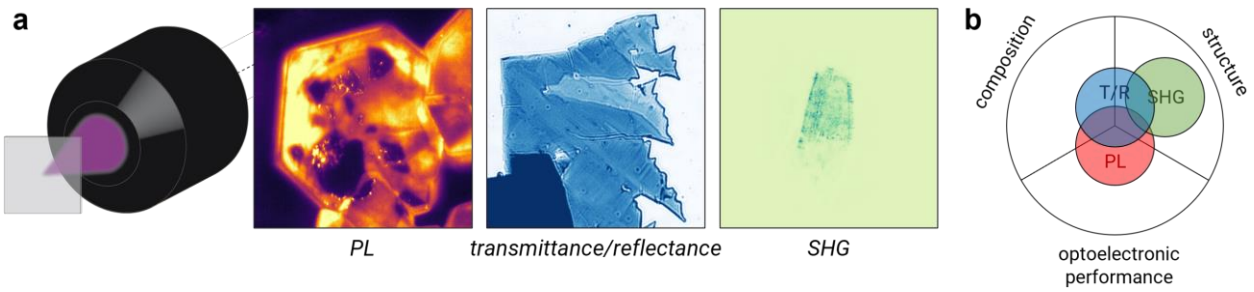

Figure 1.3. Hyperspectral widefield microscopy of halide perovskites. **(a)** Spectral microscope images of LHP micromaterials configured to isolate distinct measurable properties. **(b)** Scheme of parameter spaces explored by different widefield spectral imaging techniques.

By preparing high-quality 2D LHP materials and their interfaces then visualizing the spatial structure of their properties with microscopy, chemical behavior becomes apparent that would be masked in an ensemble. Revealing new chemical behavior offers new mechanisms to design performant and stable devices. The following chapters serve as case studies of how microanalysis can be employed to reconstruct complex interfaces of 2D LHP materials and discover useful chemical properties. Chapter 2 investigates the intrinsic phase behavior of mixed-halide 2D LHPs using high-quality microcrystals and hyperspectral imaging, revealing immiscibility behavior that emerges at the 2D limit and cannot easily be identified using conventional ensemble measurements. Chapter 3 illustrates how halide immiscibility toward the 2D limit can be used to easily fabricate sharp lateral halide heterojunctions by leveraging the intrinsic phase thermodynamics and ion diffusion properties of 2D LHPs. Finally, Chapter 4 demonstrates the merging of high-quality 3D and 2D LHPs into atomically precise heterostructures though mechanical assembly, providing a more detailed understanding of diffusion dynamics that degrade 3D/2D passivated absorbers in LHP solar cells and revealing stable alternatives.

1.4. References

(1) McMeekin David P.; Sadoughi Golnaz; Rehman Waqaas; Eperon Giles E.; Saliba Michael; Hörantner Maximilian T.; Haghighirad Amir; Sakai Nobuya; Korte Lars; Rech Bernd; Johnston Michael B.; Herz Laura M.; Snaith Henry J. A Mixed-Cation Lead Mixed-Halide Perovskite Absorber for Tandem Solar Cells. *Science* **2016**, *351* (6269), 151–155.

(2) Yang, Z.; Rajagopal, A.; Chueh, C.-C.; Jo, S. B.; Liu, B.; Zhao, T.; Jen, A. K.-Y. Stable Low-Bandgap Pb–Sn Binary Perovskites for Tandem Solar Cells. *Adv. Mater.* **2016**, *28* (40), 8990–8997.

(3) Manser, J. S.; Christians, J. A.; Kamat, P. V. Intriguing Optoelectronic Properties of Metal Halide Perovskites. *Chem. Rev.* **2016**, *116* (21), 12956–13008.

(4) Hautzinger, M. P.; Pan, D.; Pigg, A. K.; Fu, Y.; Morrow, D. J.; Leng, M.; Kuo, M.-Y.; Spitha, N.; Lafayette, D. P.; Kohler, D. D.; Wright, J. C.; Jin, S. Band Edge Tuning of Two-Dimensional Ruddlesden–Popper Perovskites by A Cation Size Revealed through Nanoplates. *ACS Energy Lett.* **2020**, *5* (5), 1430–1437.

(5) Passarelli, J. V.; Mauck, C. M.; Winslow, S. W.; Perkinson, C. F.; Bard, J. C.; Sai, H.; Williams, K. W.; Narayanan, A.; Fairfield, D. J.; Hendricks, M. P.; Tisdale, W. A.; Stupp, S. I. Tunable Exciton Binding Energy in 2D Hybrid Layered Perovskites through Donor–Acceptor Interactions within the Organic Layer. *Nat. Chem.* **2020**, *12* (8), 672–682.

(6) Smith, M. D.; Karunadasa, H. I. White-Light Emission from Layered Halide Perovskites. *Acc. Chem. Res.* **2018**, *51* (3), 619–627.

(7) Li, X.; Hoffman, J. M.; Kanatzidis, M. G. The 2D Halide Perovskite Rulebook: How the Spacer Influences Everything from the Structure to Optoelectronic Device Efficiency. *Chem. Rev.* **2021**, *121* (4), 2230–2291.

(8) Smith, M. D.; Connor, B. A.; Karunadasa, H. I. Tuning the Luminescence of Layered Halide Perovskites. *Chem. Rev.* **2019**, *119* (5), 3104–3139.

(9) Even, J.; Pedesseau, L.; Katan, C. Understanding Quantum Confinement of Charge Carriers in Layered 2D Hybrid Perovskites. *Chem. Phys. Phys. Chem.* **2014**, *15* (17), 3733–3741.

(10) Katan, C.; Mercier, N.; Even, J. Quantum and Dielectric Confinement Effects in Lower-Dimensional Hybrid Perovskite Semiconductors. *Chem. Rev.* **2019**, *119* (5), 3140–3192.

(11) Kojima, A.; Teshima, K.; Shirai, Y.; Miyasaka, T. Organometal Halide Perovskites as Visible-Light Sensitizers for Photovoltaic Cells. *J. Am. Chem. Soc.* **2009**, *131* (17), 6050–6051.

(12) *Best Research-Cell Efficiency Chart*. https://www.nrel.gov/pv/cell-efficiency.html.

(13) Al-Ashouri Amran; Köhnen Eike; Li Bor; Magomedov Artiom; Hempel Hannes; Caprioglio Pietro; Márquez José A.; Morales Vilches Anna Belen; Kasparavicius Ernestas; Smith

Joel A.; Phung Nga; Menzel Dorothee; Grischek Max; Kegelmann Lukas; Skroblin Dieter; Gollwitzer Christian; Malinauskas Tadas; Jošt Marko; Matič Gašper; Rech Bernd; Schlatmann Rutger; Topič Marko; Korte Lars; Abate Antonio; Stannowski Bernd; Neher Dieter; Stolterfoht Martin; Unold Thomas; Getautis Vytautas; Albrecht Steve. Monolithic Perovskite/Silicon Tandem Solar Cell with >29% Efficiency by Enhanced Hole Extraction. *Science* **2020**, *370* (6522), 1300–1309.

(14) Lin, K.; Xing, J.; Quan, L. N.; de Arquer, F. P. G.; Gong, X.; Lu, J.; Xie, L.; Zhao, W.; Zhang, D.; Yan, C.; Li, W.; Liu, X.; Lu, Y.; Kirman, J.; Sargent, E. H.; Xiong, Q.; Wei, Z. Perovskite Light-Emitting Diodes with External Quantum Efficiency Exceeding 20 per Cent. *Nature* **2018**, *562* (7726), 245–248.

(15) Zhu, H.; Fu, Y.; Meng, F.; Wu, X.; Gong, Z.; Ding, Q.; Gustafsson, M. V.; Trinh, M. T.; Jin, S.; Zhu, X.-Y. Lead Halide Perovskite Nanowire Lasers with Low Lasing Thresholds and High Quality Factors. *Nat. Mater.* **2015**, *14* (6), 636–642.

(16) Wei, H.; Fang, Y.; Mulligan, P.; Chuirazzi, W.; Fang, H.-H.; Wang, C.; Ecker, B. R.; Gao, Y.; Loi, M. A.; Cao, L.; Huang, J. Sensitive X-Ray Detectors Made of Methylammonium Lead Tribromide Perovskite Single Crystals. *Nat. Photon.* **2016**, *10* (5), 333–339.

(17) Leguy, A. M. A.; Hu, Y.; Campoy-Quiles, M.; Alonso, M. I.; Weber, O. J.; Azarhoosh, P.; van Schilfgaarde, M.; Weller, M. T.; Bein, T.; Nelson, J.; Docampo, P.; Barnes, P. R. F. Reversible Hydration of $CH_3NH_3PbI_3$ in Films, Single Crystals, and Solar Cells. *Chem. Mater.* **2015**, *27* (9), 3397–3407.

(18) Song, B.; Hou, J.; Wang, H.; Sidhik, S.; Miao, J.; Gu, H.; Zhang, H.; Liu, S.; Fakhraai, Z.; Even, J.; Blancon, J.-C.; Mohite, A. D.; Jariwala, D. Determination of Dielectric Functions and Exciton Oscillator Strength of Two-Dimensional Hybrid Perovskites. *ACS Materials Lett.* **2021**, *3* (1), 148–159.

(19) Braly, I. L.; deQuilettes, D. W.; Pazos-Outón, L. M.; Burke, S.; Ziffer, M. E.; Ginger, D. S.; Hillhouse, H. W. Hybrid Perovskite Films Approaching the Radiative Limit with over 90% Photoluminescence Quantum Efficiency. *Nat. Photon.* **2018**, *12* (6), 355–361.

(20) Stranks, S. D.; Eperon, G. E.; Grancini, G.; Menelaou, C.; Alcocer, M. J. P.; Leijtens, T.; Herz, L. M.; Petrozza, A.; Snaith, H. J. Electron-Hole Diffusion Lengths Exceeding 1 Micrometer in an Organometal Trihalide Perovskite Absorber. *Science* **2013**, *342* (6156), 341.

(21) Deng, S.; Shi, E.; Yuan, L.; Jin, L.; Dou, L.; Huang, L. Long-Range Exciton Transport and Slow Annihilation in Two-Dimensional Hybrid Perovskites. *Nat. Commun.* **2020**, *11* (1), 664.

(22) Yin, W.-J.; Shi, T.; Yan, Y. Unusual Defect Physics in $CH_3NH_3PbI_3$ Perovskite Solar Cell Absorber. *Appl. Phys. Lett.* **2014**, *104* (6), 063903.

(23) Kang, J.; Wang, L.-W. High Defect Tolerance in Lead Halide Perovskite $CsPbBr_3$. *J. Phys. Chem. Lett.* **2017**, *8* (2), 489–493.

(24) Yuan, Y.; Huang, J. Ion Migration in Organometal Trihalide Perovskite and Its Impact on Photovoltaic Efficiency and Stability. *Acc. Chem. Res.* **2016**, *49* (2), 286–293.

(25) Mathew, P. S.; Kamat, P. V. Cation Migration in Physically Paired 2D and 3D Lead Halide Perovskite Films. *Adv. Optical Mater.* **2023**, 2300957.

(26) Draguta, S.; Sharia, O.; Yoon, S. J.; Brennan, M. C.; Morozov, Y. V.; Manser, J. S.; Kamat, P. V.; Schneider, W. F.; Kuno, M. Rationalizing the Light-Induced Phase Separation of Mixed Halide Organic–Inorganic Perovskites. *Nat. Commun.* **2017**, *8* (1), 200.

(27) Brennan, M. C.; Draguta, S.; Kamat, P. V.; Kuno, M. Light-Induced Anion Phase Segregation in Mixed Halide Perovskites. *ACS Energy Lett.* **2018**, *3* (1), 204–213.

(28) Huang, Z.; Proppe, A. H.; Tan, H.; Saidaminov, M. I.; Tan, F.; Mei, A.; Tan, C.-S.; Wei, M.; Hou, Y.; Han, H.; Kelley, S. O.; Sargent, E. H. Suppressed Ion Migration in Reduced-Dimensional Perovskites Improves Operating Stability. *ACS Energy Lett.* **2019**, *4* (7), 1521–1527.

(29) Cho, J.; DuBose, J. T.; Le, A. N. T.; Kamat, P. V. Suppressed Halide Ion Migration in 2D Lead Halide Perovskites. *ACS Materials Lett.* **2020**, *2* (6), 565–570.

(30) Li, Z.; Klein, T. R.; Kim, D. H.; Yang, M.; Berry, J. J.; van Hest, M. F. A. M.; Zhu, K. Scalable Fabrication of Perovskite Solar Cells. *Nat. Rev. Mater.* **2018**, *3* (4), 1–20.

(31) Nie, W.; Tsai, H.; Asadpour, R.; Blancon, J.-C.; Neukirch, A. J.; Gupta, G.; Crochet, J. J.; Chhowalla, M.; Tretiak, S.; Alam, M. A.; Wang, H.-L.; Mohite, A. D. High-Efficiency Solution-Processed Perovskite Solar Cells with Millimeter-Scale Grains. *Science* **2015**, *347* (6221), 522.

(32) Niu, T.; Lu, J.; Munir, R.; Li, J.; Barrit, D.; Zhang, X.; Hu, H.; Yang, Z.; Amassian, A.; Zhao, K.; Liu, S. (Frank). Stable High-Performance Perovskite Solar Cells via Grain Boundary Passivation. *Adv. Mater.* **2018**, *30* (16), 1706576.

(33) Doherty, T. A. S.; Winchester, A. J.; Macpherson, S.; Johnstone, D. N.; Pareek, V.; Tennyson, E. M.; Kosar, S.; Kosasih, F. U.; Anaya, M.; Abdi-Jalebi, M.; Andaji-Garmaroudi, Z.; Wong, E. L.; Madéo, J.; Chiang, Y.-H.; Park, J.-S.; Jung, Y.-K.; Petoukhoff, C. E.; Divitini, G.; Man, M. K. L.; Ducati, C.; Walsh, A.; Midgley, P. A.; Dani, K. M.; Stranks, S. D. Performance-Limiting Nanoscale Trap Clusters at Grain Junctions in Halide Perovskites. *Nature* **2020**, *580* (7803), 360–366.

(34) Frohna, K.; Anaya, M.; Macpherson, S.; Sung, J.; Doherty, T. A. S.; Chiang, Y.-H.; Winchester, A. J.; Orr, K. W. P.; Parker, J. E.; Quinn, P. D.; Dani, K. M.; Rao, A.; Stranks, S. D. Nanoscale Chemical Heterogeneity Dominates the Optoelectronic Response of Alloyed Perovskite Solar Cells. *Nat. Nanotechnol.* **2021**.

(35) Gu, H.; Xia, J.; Liang, C.; Chen, Y.; Huang, W.; Xing, G. Phase-Pure Two-Dimensional Layered Perovskite Thin Films. *Nat. Rev. Mater.* **2023**, *8* (8), 533–551.

(36) Yuan, M.; Quan, L. N.; Comin, R.; Walters, G.; Sabatini, R.; Voznyy, O.; Hoogland, S.; Zhao, Y.; Beauregard, E. M.; Kanjanaboos, P.; Lu, Z.; Kim, D. H.; Sargent, E. H. Perovskite Energy Funnels for Efficient Light-Emitting Diodes. *Nat. Nanotechnol.* **2016**, *11* (10), 872–877.

(37) Zhong, X.; Ni, X.; Sidhik, S.; Li, H.; Mohite, A. D.; Brédas, J.-L.; Kahn, A. Direct Characterization of Type-I Band Alignment in 2D Ruddlesden–Popper Perovskites. *Adv. Energy Mater.* **2022**, *17*, 2202333.

(38) Shi, E.; Yuan, B.; Shiring, S. B.; Gao, Y.; Akriti; Guo, Y.; Su, C.; Lai, M.; Yang, P.; Kong, J.; Savoie, B. M.; Yu, Y.; Dou, L. Two-Dimensional Halide Perovskite Lateral Epitaxial Heterostructures. *Nature* **2020**, *580* (7805), 614–620.

(39) Pan, D.; Fu, Y.; Spitha, N.; Zhao, Y.; Roy, C. R.; Morrow, D. J.; Kohler, D. D.; Wright, J. C.; Jin, S. Deterministic Fabrication of Arbitrary Vertical Heterostructures of Two-Dimensional Ruddlesden–Popper Halide Perovskites. *Nat. Nanotechnol.* **2021**, *16* (2), 159–165.

(40) Roy, C. R.; Pan, D.; Wang, Y.; Hautzinger, M. P.; Zhao, Y.; Wright, J. C.; Zhu, Z.; Jin, S. Anion Exchange of Ruddlesden–Popper Lead Halide Perovskites Produces Stable Lateral Heterostructures. *J. Am. Chem. Soc.* **2021**, *143* (13), 5212–5221.

(41) Fu, Y.; Zheng, W.; Wang, X.; Hautzinger, M. P.; Pan, D.; Dang, L.; Wright, J. C.; Pan, A.; Jin, S. Multicolor Heterostructures of Two-Dimensional Layered Halide Perovskites That Show Interlayer Energy Transfer. *J. Am. Chem. Soc.* **2018**, *140* (46), 15675–15683.

(42) Kuo, M.-Y.; Spitha, N.; Hautzinger, M. P.; Hsieh, P.-L.; Li, J.; Pan, D.; Zhao, Y.; Chen, L.-J.; Huang, M. H.; Jin, S.; Hsu, Y.-J.; Wright, J. C. Distinct Carrier Transport Properties Across Horizontally vs Vertically Oriented Heterostructures of 2D/3D Perovskites. *J. Am. Chem. Soc.* **2021**, *143* (13), 4969–4978.

(43) Wang, Y.; Shi, Y.; Xin, G.; Lian, J.; Shi, J. Two-Dimensional van Der Waals Epitaxy Kinetics in a Three-Dimensional Perovskite Halide. *Cryst. Growth Des.* **2015**, *15* (10), 4741–4749.

(44) Xing, J.; Liu, X. F.; Zhang, Q.; Ha, S. T.; Yuan, Y. W.; Shen, C.; Sum, T. C.; Xiong, Q. Vapor Phase Synthesis of Organometal Halide Perovskite Nanowires for Tunable Room-Temperature Nanolasers. *Nano Lett.* **2015**, *15* (7), 4571–4577.

(45) Shockley, W.; Queisser, H. J. Detailed Balance Limit of Efficiency of p-n Junction Solar Cells. *J. Appl. Phys.* **1961**, *32* (3), 510–519.

(46) Green, M. A. Radiative Efficiency of State-of-the-Art Photovoltaic Cells. *Prog. Photovolt.: Res. Appl.* **2012**, *20* (4), 472–476.

Chapter 2 . Intrinsic Halide Immiscibility in Two-Dimensional Mixed-Halide Ruddlesden–Popper Perovskites[a]

2.1. Introduction

Halide alloying of lead halide perovskites (LHPs) allows their defect-tolerant optoelectronic properties to be tailored to precise optoelectronic applications by tuning their bandgaps from ~1.6 eV in pure iodide LHPs to ~3.1 eV in pure chloride LHPs.[1–3] I/Br mixed-halide LHPs in particular are pushing the frontier of perovskite photovoltaics, by engineering the bandgaps to enable perovskite/Si and other tandem cells that are rapidly approaching efficiencies of 30%.[4–7] Though halides are readily miscible under standard conditions in LHPs, photoinduced phase separation – a reversible process in which homogeneously alloyed domains of mixed-halide LHPs diverge into near-phase-pure halide domains under illumination – complicates the stability of alloyed LHPs.[8–11] In the widely studied I/Br mixed-halide LHPs, phase separation is understood to occur because of a "miscibility gap" that emerges in the I/Br phase diagram under illumination,[12,13] which drives spontaneous formation of I-rich and Br-rich domains via facile anion migration that is exacerbated by polarons in the soft lattice.[14,15] Separation of halide domains hinders the photovoltaic and optoelectronic performance of many devices due to the funneling of charge carriers and energy into the iodide-rich domains of the heterogeneous mixture.[14,16–18]

Similar challenges of ion migration and phase separation also exist in 2D Ruddlesden–Popper lead halide perovskites (RPPs), which have found their own success as solar absorbers,[19,20] passivating layers in LHP solar cells,[21,22] light-emitting diodes,[23,24] and as emerging systems for the

[a] This chapter was originally published as an article (*ACS Energy Lett.* **2022**, *7*(10), 3423-3431.) in collaboration with Yadong Zhou, Daniel D. Kohler, Zihua Zhu, John C. Wright, and Song Jin.

study of novel physics in van der Waals heterostructures.[25–27] RPPs consist of quasi-2D perovskite slabs separated by bilayers of large "spacer" cations (LA). The RPP formula $(LA)_2(A)_{n-1}Pb_nX_{3n+1}$ is a function of the thickness of the perovskite slabs indexed by the parameter n (in units of PbX_6^{2-} octahedra),[28] which inversely correlates to the degree of quantum confinement of the inorganic sublayers. The wide selection of spacer cations and relaxed structural tolerances compared to 3D LHPs present a vast landscape of chemical and structural tunability rarely seen in high-performance semiconductors,[29–31] and the relative hydrophobicity of organic spacer cations improves the environmental resilience of RPPs relative to 3D LHPs.[32] Photoinduced phase separation is understood to be kinetically slowed in mixed-halide RPPs (and in similar layered Dion–Jacobson mixed-halide perovskites),[33,34] and the ion migration kinetics are further influenced by n and the choice of spacer cation.[35–37] Existing studies of mixed-halide RPPs mostly presume that they are fully miscible under standard conditions and that phase separation only occurs under perturbations like light or heat,[38–41] with most attention turned toward the influence of structural parameters on phase separation kinetics.

But there are signs that halides may even be immiscible in RPPs under standard conditions. Ion migration in RPPs has been directly investigated in I/Br diffusion couples prepared as mechanically assembled van der Waals heterostructures.[42,43] Photoluminescence (PL) spectra of the evolving diffusion couples at elevated temperature showed discrete emission peaks trading off in intensity, rather than the continuous shifting and broadening of PL to be expected from a fully miscible phase system abiding by Vergard's law.[8] The discrete peaks instead suggest that only a small set of halide stoichiometries were present during the interdiffusion process. There were similar signs in our recent work exploring the use of anion exchange with HBr vapor to prepare lateral I/Br heterojunctions from pure-I RPP microplates.[44] X-ray diffraction (XRD) patterns of

samples undergoing exchange revealed that only near-pure-I or near-pure-Br phases were present over the course of the reaction in $n < 3$ RPP phases, with no signs of alloy formation at the junction in optical images. We concluded that such results could only be explained if the I/Br phase system was immiscible under the ambient exchange reaction conditions. These findings drove us to investigate the I/Br phase system of RPPs more carefully, paying attention to the thermodynamically favored phase landscape in ambient conditions without incorporating photoinduced phase separation.

Here we present a rigorous and systematic study of the I/Br phase behaviors under standard conditions for three representative $n = 1$ and $n = 2$ RPP phases: $(PEA)_2PbX_4$, $(HA)_2PbX_4$, and $(HA)_2(FA)Pb_2X_7$ (PEA is phenethylammonium, HA is *n*-hexylammonium, and FA is formamidinium) using solution-grown microplates. For brevity, we refer to these phases as $n = 1$ PEA, $n = 1$ HA, and $n = 2$ HA-FA, respectively. X-ray diffraction and time-of-flight secondary ion mass spectrometry (ToF-SIMS) imaging reveal phase separation and microscale heterogeneity of halide domains in RRPs with certain mixed I/Br ratios prior to any photoinduced phase separation, suggesting that halide phase separation is an intrinsic thermodynamic outcome in RPPs near the 2D limit. Such phase separation can easily be overlooked using routine characterization methods like PL and optical microscopy, but spectral imaging of mixed-halide microplates can accurately identify heterogeneous halide phase speciation with accessible high-throughput instrumentation.

2.2. Exploring Binary I/Br Phase Systems of R–P Lead Halide Perovskites

To identify the innate speciation of halides in RPPs in absence of perturbations like light or heat, we synthesized mixed-halide RPP microplates by modifying an established synthesis in aqueous hydrohalic acid (HX) solution.[26,28,44] This synthesis allows precise control over the ratio

of HBr to HI in the two-component HX solution, enabling fine iteration (<1%) across compositional ranges of interest in the I/Br phase diagram (see Experimental details in the SI). We chose halide-free precursor salts (lead(II) oxide, formamidinium acetate) to ensure that HX is the only significant halide source during synthesis, and the excess concentration of halides relative to other precursors ensured the phase purity of $n > 1$ RPPs was not affected by the relative amount of I vs. Br in solution. The mixed-halide RPPs precipitate from a moderate supersaturation condition as numerous few-to-single grain microplates that are large enough (~25-250 μm along their longest axes) to exhibit the macroscopic crystalline morphology of the mixed-halide phases, while also yielding enough objects to identify variance among individual crystals of a given phase. Figure 2.1 shows characteristics of microplates precipitated from HX solutions of varying Br% for the three RPP parent phases. Note that the halide percentages stated throughout this work are the compositions of the precursor solutions, not necessarily the precipitates, which may deviate greatly from the halide content of the precursor solution due to differing growth kinetics between I vs. Br analogues of the same phase.

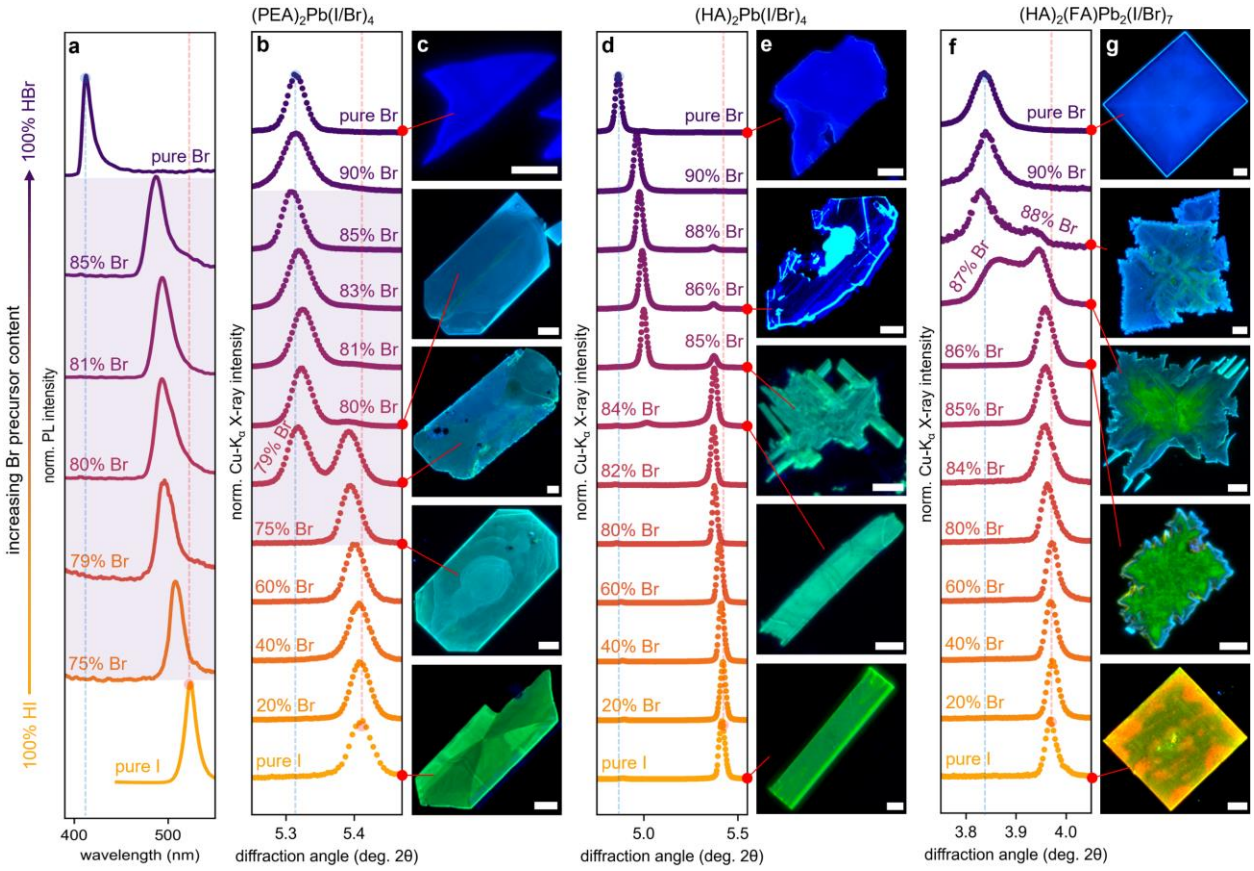

Figure 2.1. Exploring the I/Br phase behaviors in lead halide RPPs. **(a)** PL spectra of n = 1 PEA-Pb-I/Br microplates grown from aqueous precursor solutions of increasing Br% under low excitation power (20 μW/cm^2). Equivalent spectra for n = 1 HA and n = 2 HA-FA phases are provided in Figure A1.3. **(b,d,f)** XRD patterns of mixed-halide RPP microplates centered on the (002) reflections of each phase: n = 1 PEA-Pb-I/Br **(b)**, n = 1 HA-Pb-I/Br **(d)**, n = 2 HA-FA-Pb-I/Br **(f)**, collected prior to light exposure. The shaded patterns in the n = 1 PEA phase system (b) were collected from the same samples measured in (a). **(c,e,g)** True-color PL images of representative microplates from selected compositions of XRD samples in (b,d,f), emphasizing changes around the crossover points of the I/Br phase systems. The correspondence between the PL images and XRD patterns are marked by red dots and lines. All scale bars are 10 μm.

Importantly, there is a disagreement in the apparent phase information obtained from photoluminescence (PL) measurements and X-ray diffraction (XRD) patterns, as evidenced by comparing PL spectra obtained from mixed-halide $n = 1$ PEA microplates (Figure 2.1a) and the same samples' XRD patterns prior to light exposure (Figure 2.1b). Iterating by small Br% increments across a small range of the I/Br system leads to little change in PL emission wavelength or broadness, which remain close to the emission wavelength of the pure-I $n = 1$ PEA phase despite the high Br% of the precursor solution. If we were to assume that halides are fully miscible in absence of light (as in 3D LHPs), this result would not be surprising given the small range of the mixed-halide ratios that was examined, and the near-I emission wavelength could be attributed to growth kinetics favoring iodide incorporation into the alloy. However, XRD patterns of microplate samples from the same composition range paint a fundamentally different picture: two discrete (002) reflections at angles near the pure-I and pure-Br analogues of the parent RPP phase trade off in intensity with little to no shifting as the Br% increases. At 79% Br, the tandem reflections suggest an immiscible I/Br phase system with a distinct "crossover point", at which two discrete halide phases trade off in proportion in a lever rule fashion. The XRD (collected prior to light exposure) and the PL (collected at a low excitation irradiance of 20 $\mu W/cm^2$) should both measure the properties of the mixed-halide phases in absence of photoinduced halide phase separation, therefore this discrepancy shows that PL emission alone is not a reliable tool for the identification of halide phase separation in mixed-halide samples. Characterization using PL images of the microplates in the XRD samples (Figure 2.1c) can suffer from the same shortcoming as PL spectra. Aside from minor changes in hue, there is no obvious indication of heterogeneous halide speciation in the microplates, and the emission color is consistent from plate to plate across a given sample (Figure A1.4).

In other 2D RPP phases, however, signs of heterogeneity are obvious beyond XRD patterns. This is seen in $n = 1$ HA microplates and $n = 2$ HA-FA microplates around their crossover points of I/Br composition (Figure 2.1d-g). In the $n = 1$ HA case, there is a notable change in PL color from seafoam green to violet as the crossover point (84-86 Br%) is passed (Figure 2.1e). This change is accompanied by a significant change in crystal morphology as the growth habit of the microplates more closely resemble the pure-Br phase. But the microplates grown from the 85% Br solution near the middle of the crossover point have a uniquely complex morphology not observed toward either limit of the binary phase system, which we believe may be the result of a "frustrated" growth regime between two competing phases with different habits. In the $n = 2$ HA-FA case (Figure 2.1g), the heterogeneity of halide composition is even more obvious in PL images, with a near-pure-Br phase emitting blue light overtaking the light-green emission of a near-pure-I phase as the Br% of the growth solution is increased. The morphology of the products at the crossover point (86-88 Br%) have a unique dendritic character that is not seen in either phase-pure analogue, and there is a notable transition in crystal morphology and PL emission beyond the crossover range implied by the XRD patterns (Figure A1.5). We also confirmed that this morphology change is not resultant of n phase impurities through XRD patterns across an extended range, which show no signs of $n = 1$ or $n \geq 3$ (00l) reflections in the $n = 2$ HA-FA sample (Figure A1.6). The $n = 1$ HA and $n = 2$ HA-FA examples suggest that not only are multiple discrete halide phases coprecipitating at crossover points of the I/Br phase system, but they also grow among one-another as distinct domains within a common object.

2.3. Complications of Measuring Multi-Halide Speciation with PL

To further illustrate the disconnect in apparent phase information obtained from PL spectroscopy and XRD, we employed confocal PL mapping to visualize the different halide phases

in a crossover point sample. We focus the discussion on an $n = 2$ HA-FA microplate from a mixed-halide sample that should be bromide-rich according to the relative proportion of Br vs. I (002) peaks in the XRD pattern (Figure 2.2a). The angles of the (002) reflections suggest that there should be a nearly pure Br phase and a moderately alloyed intermediate phase, but this is not reflected in PL spectra from microplates in the same sample (Figure 2.2b). Instead, PL shows the presence of a nearly pure *iodide* phase and an intermediate peak that may correspond to the discrete alloy.

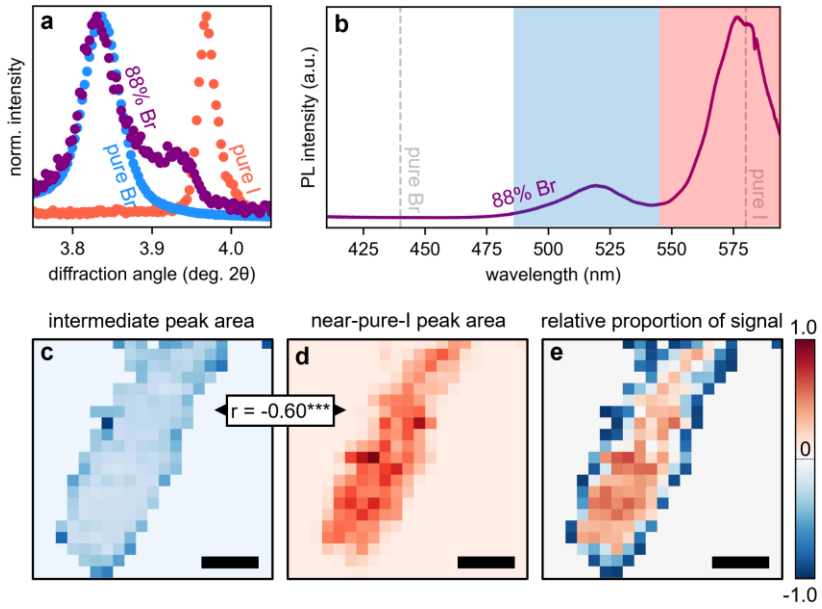

Figure 2.2. Coexistence of multiple phases in individual mixed-halide RPP microplates. **(a)** XRD pattern centered at the (002) reflections of a mixed-halide $n = 2$ HA-FA microplate sample prepared from an 88% Br precursor solution in comparison to phase-pure analogues. **(b)** Confocal PL spectrum from a single mixed-halide microplate taken from the XRD sample shown in (a). **(c,d)** PL intensity maps of the same mixed-halide RPP microplate producing the spectrum in (b) corresponding to the integrated signal from shaded regions of the PL spectrum in (b). **(e)** Relative proportion of total PL intensity between the two peaks mapped in (c) and (d). All scale bars are 10 μm.

Comparing maps at the two emission peaks shows localization of emission from each peak in contrasting regions of a single microplate (Figure 2.2c, d). The map of the intermediate peak shows significant emission throughout the entire microplate that is most intense around the edges, whereas the map for near-pure-I emission is mostly localized toward the center. The areas of the two peaks are significantly anticorrelated in the x-y plane (r = -0.60, $p < 0.0001$), which would be expected of a substitutional relationship between the phases responsible for the emission. The difference in each peak's localization is emphasized when the relative proportion of each peak's normalized x-y signal are compared (Figure 2.2e), highlighting the separated speciation of the two emission features. Aside from the clear lateral variance in each peaks' proportion, the coexistence of emission from both peaks in the center implies that two distinct phases may be layered on top of one-another.

Despite its frequent use in the phase characterization of halide alloys, PL spectra are known to favor the emission of narrower bandgap components of heterogeneous mixed-halide LHPs through several mechanisms. Photon recycling likely contributes to the iodide-favored emission, as the narrower bandgap I-rich domains can re-absorb the emission from the wider bandgap Br-rich domains before the emitted light can escape the crystal.[45,46] Photon recycling would be even more prevalent in the scenario where narrower bandgap phases constitute the upper layers of the crystallite, as the emission across the entire plane of a microplate would be uniformly biased toward I-rich emission. This mechanism could also be partially responsible for the emission bias of the intermediate peak toward the microplate edges, as well as the blue edges apparent in many of the PL photographs. As light emitted from wider bandgap phases is refracted and reabsorbed through the crystal, rays that meet the microcrystal edges could be scattered by the edge and other boundaries, allowing bluer light to escape the structure. We could also attribute the dominance of

iodide PL to concentration quenching effects that are historically known to occur in materials with similar relative donor-acceptor concentrations.[47–50] Such donor-acceptor interactions are evident in studies of photoinduced phase separation in I/Br LHPs, where the PL emission of I-rich domains dominates the total emission of the sample over time as carriers become trapped in the potential wells of the narrower bandgap I-rich regions of the sample.[8,10]

Additionally, photoinduced phase separation could convolve the results measured via PL. To investigate this possibility, we performed a photostability experiment with high time resolution on individual mixed-halide n = 2 HA-FA microplates, in which we emulated the excitation conditions used for confocal PL mapping and optical microscope PL imaging (Figure A1.7). The results showed that photoinduced phase separation occurs over hundreds of ms when the laser excitation source is focused to a microscopic spot, but occurs over minutes under the diffuse UV light used for PL optical imaging. These results show that if care is not taken to minimize collection time or excitation power, a steady state of phase separation could already be reached by the time a spectra or images are acquired, falsely implying the presence of different chemical phases than what a sample initially was. In this work, we ensured light exposure times for all spectra and imaging experiments fell well within the onset window of phase separation indicated by the photostability measurements.

These phenomena together explain the near-I emission from n = 1 PEA mixed-halide microplates at the I/Br crossover point despite evidence of a Br-rich phase from XRD (Figure 2.1a, b). This explanation is only possible if multiple phases are coprecipitating as separate domains within the same crystallite, but structural characterization techniques more direct and accurate than PL are necessary to understand the layer-to-layer speciation of halide domains in these structures.

2.4. Distinct Forms of Halide Heterogeneity in Mixed-Halide R–P Perovskites

Time-of-flight secondary ion mass spectrometry (ToF-SIMS) provides 3-dimensional chemical imaging of the mixed-halide microplates with few-nanometer depth resolution. We used SIMS to examine mixed-halide $n = 2$ HA-FA microplates at the crossover point of the I/Br phase system. AFM topography of the microplates collected prior to SIMS analysis shows that the depth resolution of the SIMS analysis is within 5 nm (Figure A1.8), which suggests that compositional changes across very few perovskite layers can be resolved. Among the four microplates analyzed via SIMS (Figure 2.3 and Figure A1.9), two key forms of halide speciation were identified. The first form, highlighted in Figure 2.3a_1-f_1, consists of halide composition that uniformly changes as a function of depth. The I vs. Br SIMS signals show little variation in the x-y plane of the plate, except at defects, which appear to be iodide rich. Interestingly, while defects in the bulk of the microplate are iodide-rich, the edges seem bromide rich, possibly explaining the more intense blue emission toward the edges of the microplate observed in the PL image (Figure 2.3b_1). Substantial changes in halide composition occur along the depth axis. This is emphasized by comparing the relative amount of each halide signal in a depth section of the microplate (Figure 2.3e_1), which reveals an iodide-rich surface domain separated from a bromide-rich subsurface. The tradeoff in I vs. Br intensity occurs continuously through the depth of the plate (Figure A1.10), with iodide-rich and bromide-rich regions localized toward the upper and lower extrema of the microplate's depth, respectively (Figure 2.3f_1). This change in composition from layer-to-layer is difficult to identify from optical information alone, as the only significant changes in color of the microplate appear to be from etaloning between the reflective substrate and the microplate surface ~170 nm above (Figure 2.3a_1). We are confident this halide speciation is not a result of photoinduced phase segregation. We performed photostability experiments on equivalent $n = 2$ HA-FA microplates,

where we found that the exposure necessary to acquire PL images induced almost no phase separation (Figure A1.7). The little phase separation that did occur over such short timescales is reversible over seconds and has an I-rich spatial distribution that does not correspond to that depicted by the SIMS data. Additionally, the distribution of I vs. Br along the depth of the sample is opposite of what has been reported after UV light exposure at the surface of mixed-halide RPP thin films,[51] and the total exposure of the sample to UV light during imaging was orders of magnitude less than reported examples of illumination that resulted in photoinduced phase separation (see Experimental Methods in the SI).[35,51]

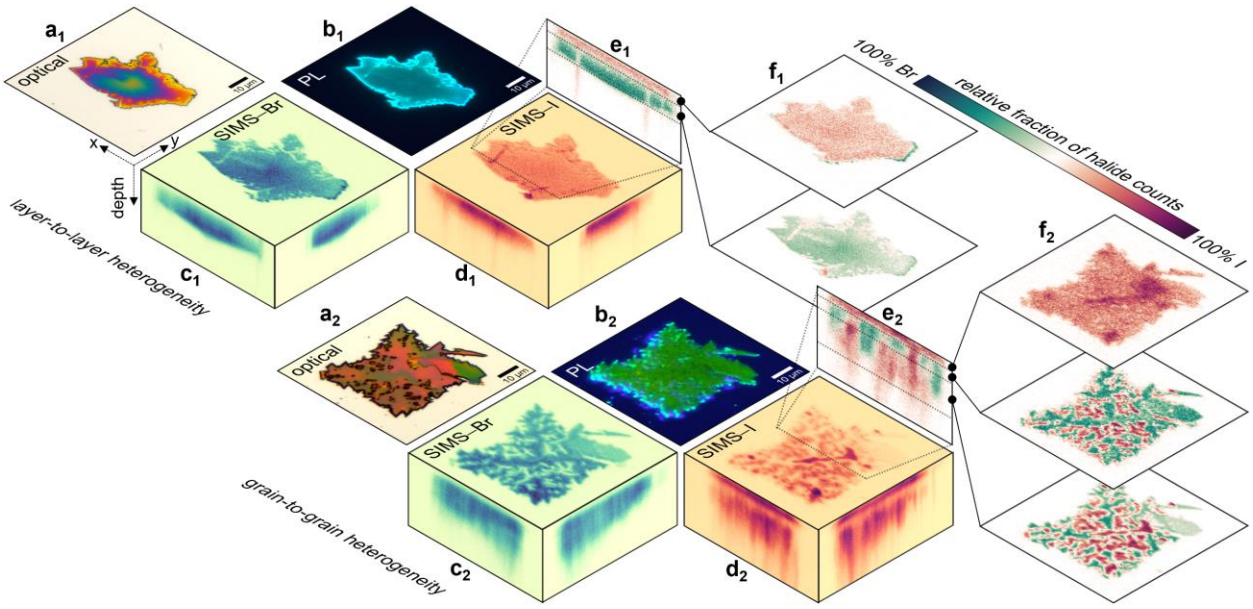

Figure 2.3. Chemical imaging of intrinsic halide domains in two mixed-halide RPP microplates using ToF-SIMS. **(a)** Contrast-enhanced optical microscope images and **(b)** the corresponding true-color PL images collected under minimal light exposure (< 5 mW/cm^2, < 30 s exposure) of mixed-halide $n = 2$ HA-FA microplates grown at the crossover point of the I/Br phase system. All scale bars are 10 μm. **(c, d)** Sums along axes of ToF-SIMS halide counts for bromide **(c)** and iodide **(d)** (note that the depth axis is not to-scale with x-y). **(e)** Relative I/Br% of total halide signal in a depth cross-section of the microplates depicted in (c) & (d). The dashed traces in (d) are the regions

from which the cross-sections were extracted. **(f)** Relative I/Br% of total halide signal from depth sections of the microplates depicted in (c) & (d). The dashed lines in (e) partition the depth sections imaged in (f).

The second form of halide speciation exhibits more complex grain-to-grain heterogeneity (Figure 2.3a_2-f_2). Whereas optical and PL images of a thicker mixed-halide microplate (~680 nm height according to AFM, Figure A1.8) only show minor signs of contrast in hue (Figure 2.3a_2 & b_2), separated halide domains are immediately apparent along all 3 spatial dimensions when the I and Br SIMS signals are compared (Figure 2.3c_2 & d_2). A depth cross-section at a core region of the microplate shows 3 significant subdomains of depth (Figure 2.3e_2). When the relative percentage of I vs. Br signals is analyzed in each subdomain (Figure 2.3f_2), the 3D heterogeneity is fully visualized. At the surface the iodide-rich phase is dominant, whereas the subsurface has a 3D multi-halide grain structure that varies both in the x-y plane and as a function of depth. The two subsurface domains imaged in the lower two panes of Figure 2.3f_2 show the emergence of iodide-rich veins beneath a multi-halide midsection containing a bromide-rich core. Despite the drastic variance of halide composition in all three spatial dimensions, the PL emission from the bulk of the microplate appears uniform (Figure 2.3b_2), and the PL and SIMS data have no tangible correlation from point-to-point (Spearman's $\rho = 0.09$***, Figure A1.11). illustrating how emission bias toward narrower bandgap phases greatly muddles the interpretation of halide phase separation in mixed-halide RPPs.

2.5. Identifying Multi-Halide Phase Separation Using Spectral Imaging

Accurate ToF-SIMS imaging of halides cannot be extended to every sample due to the accessibility and throughput of the technique, but routine methods of characterization such as optical and PL microscopy cannot alone provide a reliable understanding of the phase separation

in mixed-halide samples. XRD reveals the thermodynamic outcomes of a halide phase system but cannot reveal microscale halide heterogeneity in individual crystallites. This discrepancy motivated us to find an approach for phase identification in mixed-halide RPPs that is both convenient and more accurate than the existing routine methods. Using the ToF-SIMS data as a reference for the expected halide distributions in mixed-halide RPP microplates, we used a custom-built hyperspectral microscope (see Experimental Methods in the SI) to study the same type of mixed-halide n = 2 HA-FA samples as those analyzed with SIMS to look for matching spatial distributions in spectral images of transmittance in individual microplates.

Transmittance spectra from individual n = 2 HA-FA microplates in Figure 2.4a show three key spectral signatures at 440 nm, 480 nm, and 570 nm that are associated with three discrete halide phases. The absorption onsets from the band edges of the three phases are sequentially revealed as the Br% of the growth solution increases. The 570 nm absorption edge, which we assign to a nearly pure iodide-rich phase, diminishes as the relative proportion of iodide phase in the sample decreases, but the 480 nm absorption onset remains in the 87% Br sample, revealing it to be associated with the band edge absorbance of an intermediate alloy phase. This feature is close in wavelength to the intermediate PL peak observed from another mixed-halide n = 2 HA-FA microplate near the I/Br crossover point (Figure 2.2). Increasing the Br% further reveals the band edge absorption onset from a near-pure-Br phase in a sample prepared from an 88 Br% solution, revealing all three discrete halide phases expected from the XRD patterns of the samples (Figure A1.12).

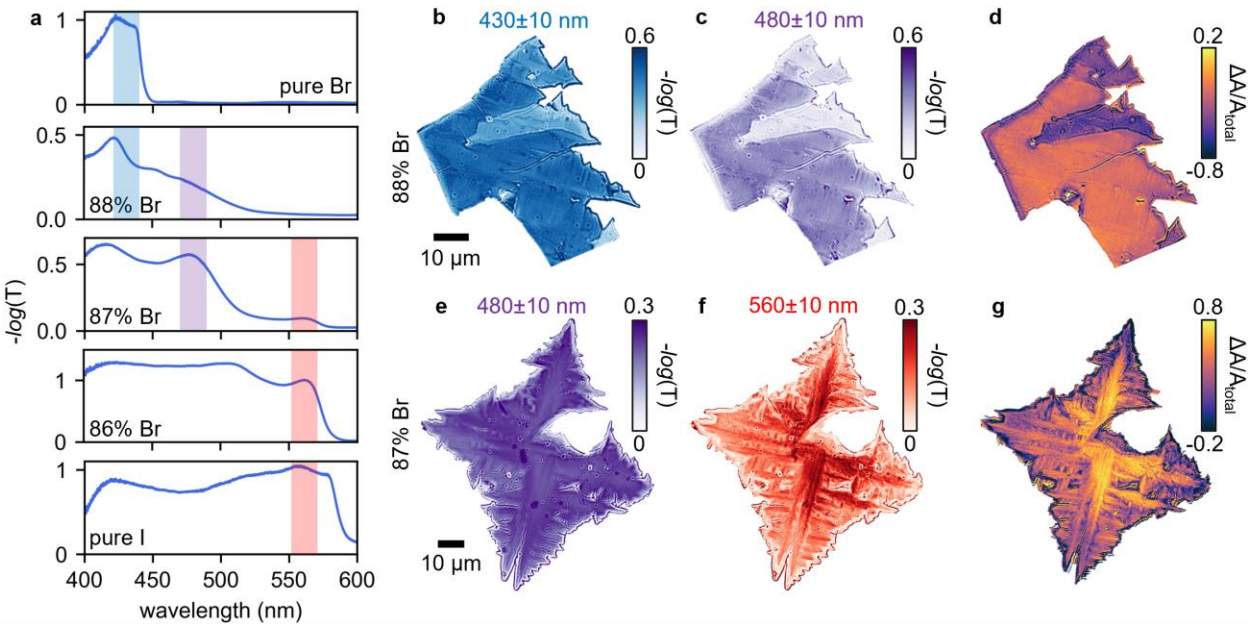

Figure 2.4. Spectral identification of halide domains in two mixed-halide n = 2 HA-FA microplates. **(a)** Micro-transmittance spectra collected from individual mixed-halide microplates grown around the crossover point of the I/Br phase system, compared to their phase-pure analogues. **(b,c,e,f)** Spectral images of transmittance in two representative mixed-halide microplates at band edge absorption wavelengths of each halide phase (±10 nm), corresponding to highlighted spectral ranges in (a). **(d,g)** Difference in -*log*(T) at the two wavelength ranges imaged in (b,c/e,f) normalized to the sum of signal from both wavelength ranges.

With absorption onsets associated with all three phases identified, we can visualize the spatial distribution of each halide phase by imaging microplates using incident light filtered around each phase's band edge absorption onset (see Experimental Methods). Figure 2.4b & c show spectral images of transmittance in a mixed-halide n = 2 HA-FA microplate that has a distinct step edge from the growth of one microplate layer on top of another. The transmittance in the region of the near-pure-Br absorption onset is uniform across the microplate, except for a higher transmittance middle section where the upper layers of the plate are absent (Figure 2.4b). Imaging

at wavelengths correspondent to the alloy phase absorption onset show that the same middle section is almost completely transmissive (Figure 2.4c), as opposed to the uniform presence of alloy absorption in regions of the microplate where the upper layer is present. The contrast in transmittance is emphasized by computing the difference of -*log*(T) between each wavelength range and normalizing it to the sum of -*log*(T) at both wavelengths (Figure 2.4d). Since the contrast is normalized to the total signal, it is a quantity invariant with respect to sample thickness, which is demonstrated by imaging a pure-I microplate with varying thickness at multiple wavelengths (Figure A1.13). The contrast image visualizes the layer-to-layer halide heterogeneity in the microplate as revealed by SIMS examples, with a uniform I/Br alloy layer grown on top of a near-pure-Br layer.

A microplate with complex halide heterogeneity that appears to be similar to the second type of SIMS example (Figure 2.3a_2-f_2) is imaged in Figure 2.4e & f. Imaging transmittance at the onset wavelength of the intermediate alloy phase (480±10 nm) shows a relatively uniform distribution across the plane of the microplate (Figure 2.4e), with only minor changes that may be associated with varying thickness, but transmittance at the near-pure-I band edge (560±10 nm) reveals obvious localization of an I-rich phase toward core regions of the microplate (Figure 2.4f). The separation of halide domains is further emphasized by mapping the contrast between each absorbance feature (Figure 2.4g), which reveals iodide-rich veins closely resembling those mapped in SIMS analysis.

The examples shown in Figure 2.4 demonstrate how spectral imaging is both high-throughput and accurate in identifying heterogeneous halide speciation in individual crystallites, but there are some important considerations during spectral imaging analysis. Complications may arise when the sample is exceedingly thick, as the optical density may become too high to

effectively distinguish between the absorption of multiple above-band features. In this scenario reflectance spectroscopy can serve as a complementary technique. Reflectance spectra from the surface of microplates contain features that correspond to band edge absorption features identified in transmittance spectra (Figure A1.14),[52] presenting an alternative approach to distinguish the presence of distinct phases at the surface of the crystallite. Reflectance also aids in the identification of layer-to-layer heterogeneity in cases where the entire plane of the microplate is uniformly covered by multiple phases. In thinner samples (on the order of hundreds of nm), overlaying layers of distinct phases can exhibit spectral fringes due to etaloning between the adjacent layers. Etaloning oscillations are most apparent in reflectance spectra, and their diminishment or modulation can reveal absorption onsets from higher bandgap phases that are distinguishable from above-bandgap absorption of the narrowest bandgap phase (Figure A1.15).

2.6. Conclusion

Through careful studies of $n = 1$ and $n = 2$ I/Br mixed-halide RPP phases, we showed that halide domain separation in RPPs can be an inherent outcome of halide immiscibility at ambient conditions without photoinduced phase separation. This innate phase separation, revealed by XRD patterns at the crossover points of the I/Br phase systems, can easily be overlooked due to misleading phase information deduced from common characterization methods like PL and optical microscopy, but can be clearly elucidated using ToF-SIMS chemical imaging. We further show how spectral imaging can reliably identify halide domain morphology in individual crystallites of mixed-halide RPP phases. The low temperature gradient and mild supersaturation conditions used for crystal growth in this study suggest that halide domain separation is the thermodynamically favored outcome at room temperature for RPPs, and such phase immiscibility explains the success in creating sharp halide heterojunctions in $n = 1$ and $n = 2$ RPPs.[44,53] However, homogeneous halide

alloys may still be attainable, and may have already been attained in some reported mixed-halide RPPs,[40,54] but such results are likely accessible through kinetically controlled growth pathways that depend on synthesis conditions. The intrinsic phase separation of halide domains in mixed-halide RPPs revealed in this study demands a shift in approach from 3D to 2D as more mixed-halide RPPs are utilized in optoelectronic devices, while also painting a unique halide phase landscape that offers intrinsic multi-halide speciation previously inaccessible to 3D mixed-halide LHPs. The spectral imaging techniques demonstrated here also provide a readily accessible optical method to accurately identify halide phase separation in mixed-halide perovskite materials.

2.7. References

(1) Manser, J. S.; Christians, J. A.; Kamat, P. V. Intriguing Optoelectronic Properties of Metal Halide Perovskites. *Chem. Rev.* **2016**, *116* (21), 12956–13008.

(2) Zhu, H.; Fu, Y.; Meng, F.; Wu, X.; Gong, Z.; Ding, Q.; Gustafsson, M. V.; Trinh, M. T.; Jin, S.; Zhu, X.-Y. Lead Halide Perovskite Nanowire Lasers with Low Lasing Thresholds and High Quality Factors. *Nat. Mater.* **2015**, *14* (6), 636–642.

(3) Sutter-Fella, C. M.; Li, Y.; Amani, M.; Ager, J. W.; Toma, F. M.; Yablonovitch, E.; Sharp, I. D.; Javey, A. High Photoluminescence Quantum Yield in Band Gap Tunable Bromide Containing Mixed Halide Perovskites. *Nano Lett.* **2016**, *16* (1), 800–806.

(4) McMeekin D. P.; Sadoughi G.; Rehman W.; Eperon G. E.; Saliba M.; Hörantner M. T.; Haghighirad A.; Sakai N.; Korte L.; Rech B.; Johnston M. B.; Herz L. M.; Snaith H. J. A Mixed-Cation Lead Mixed-Halide Perovskite Absorber for Tandem Solar Cells. *Science* **2016**, *351* (6269), 151–155.

(5) Eperon G. E.; Leijtens T.; Bush K. A.; Prasanna R.; Green T.; Wang J. T-W.; McMeekin D. P.; Volonakis G.; Milot R. L.; May R.; Palmstrom A.; Slotcavage D. J.; Belisle R. A.; Patel J. B.; Parrott E. S.; Sutton R. J.; Ma W.; Moghadam F.; Conings B.; Babayigit A.; Boyen H-G.; Bent S.; Giustino F.; Herz L. M.; Johnston M. B.; McGehee M. D.; Snaith H. J. Perovskite-Perovskite Tandem Photovoltaics with Optimized Band Gaps. *Science* **2016**, *354* (6314), 861–865.

(6) Bush, K. A.; Palmstrom, A. F.; Yu, Z. J.; Boccard, M.; Cheacharoen, R.; Mailoa, J. P.; McMeekin, D. P.; Hoye, R. L. Z.; Bailie, C. D.; Leijtens, T.; Peters, I. M.; Minichetti, M. C.; Rolston, N.; Prasanna, R.; Sofia, S.; Harwood, D.; Ma, W.; Moghadam, F.; Snaith, H. J.;

Buonassisi, T.; Holman, Z. C.; Bent, S. F.; McGehee, M. D. 23.6%-Efficient Monolithic Perovskite/Silicon Tandem Solar Cells with Improved Stability. *Nat. Energy* **2017**, *2* (4), 17009.

(7) Al-Ashouri, A.; Köhnen, E.; Li, B.; Magomedov, A.; Hempel, H.; Caprioglio, P.; Márquez, J. A.; Morales Vilches, A. B.; Kasparavicius, E.; Smith, J. A.; Phung, N.; Menzel, D.; Grischek, M.; Kegelmann, L.; Skroblin, D.; Gollwitzer, C.; Malinauskas, T.; Jošt, M.; Matič, G.; Rech, B.; Schlatmann, R.; Topič, M.; Korte, L.; Abate, A.; Stannowski, B.; Neher, D.; Stolterfoht, M.; Unold, T.; Getautis, V.; Albrecht, S.. Monolithic Perovskite/Silicon Tandem Solar Cell with >29% Efficiency by Enhanced Hole Extraction. *Science* **2020**, *370*, 1300–1309.

(8) Hoke, E. T.; Slotcavage, D. J.; Dohner, E. R.; Bowring, A. R.; Karunadasa, H. I.; McGehee, M. D. Reversible Photo-Induced Trap Formation in Mixed-Halide Hybrid Perovskites for Photovoltaics. *Chem. Sci.* **2015**, *6* (1), 613–617.

(9) Brennan, M. C.; Draguta, S.; Kamat, P. V.; Kuno, M. Light-Induced Anion Phase Segregation in Mixed Halide Perovskites. *ACS Energy Lett.* **2018**, *3* (1), 204–213.

(10) Knight, A. J.; Wright, A. D.; Patel, J. B.; McMeekin, D. P.; Snaith, H. J.; Johnston, M. B.; Herz, L. M. Electronic Traps and Phase Segregation in Lead Mixed-Halide Perovskite. *ACS Energy Lett.* **2019**, *4* (1), 75–84.

(11) Knight, A. J.; Borchert, J.; Oliver, R. D. J.; Patel, J. B.; Radaelli, P. G.; Snaith, H. J.; Johnston, M. B.; Herz, L. M. Halide Segregation in Mixed-Halide Perovskites: Influence of A-Site Cations. *ACS Energy Lett.* **2021**, *6* (2), 799–808.

(12) Wang, X.; Ling, Y.; Lian, X.; Xin, Y.; Dhungana, K. B.; Perez-Orive, F.; Knox, J.; Chen, Z.; Zhou, Y.; Beery, D.; Hanson, K.; Shi, J.; Lin, S.; Gao, H. Suppressed Phase Separation of Mixed-Halide Perovskites Confined in Endotaxial Matrices. *Nat. Commun.* **2019**, *10* (1), 695.

(13) Chen, Z.; Brocks, G.; Tao, S.; Bobbert, P. A. Unified Theory for Light-Induced Halide Segregation in Mixed Halide Perovskites. *Nat. Commun.* **2021**, *12* (1), 2687.

(14) Bischak, C. G.; Hetherington, C. L.; Wu, H.; Aloni, S.; Ogletree, D. F.; Limmer, D. T.; Ginsberg, N. S. Origin of Reversible Photoinduced Phase Separation in Hybrid Perovskites. *Nano Lett.* **2017**, *17* (2), 1028–1033.

(15) Limmer, D. T.; Ginsberg, N. S. Photoinduced Phase Separation in the Lead Halides Is a Polaronic Effect. *J. Chem. Phys.* **2020**, *152* (23), 230901.

(16) Knight, A. J.; Herz, L. M. Preventing Phase Segregation in Mixed-Halide Perovskites: A Perspective. *Energy Environ. Sci.* **2020**, *13* (7), 2024–2046.

(17) Yin, X.; Guo, Y.; Liu, J.; Que, W.; Ma, F.; Xu, K. Photoinduced Phase Segregation Leading to Evident Open-Circuit Voltage Loss in Efficient Inorganic $CsPbIBr_2$ Solar Cells. *J. Phys. Chem. Lett.* **2020**, *11* (17), 7035–7041.

(18) Frohna, K.; Anaya, M.; Macpherson, S.; Sung, J.; Doherty, T. A. S.; Chiang, Y.-H.; Winchester, A. J.; Orr, K. W. P.; Parker, J. E.; Quinn, P. D.; Dani, K. M.; Rao, A.; Stranks, S. D. Nanoscale Chemical Heterogeneity Dominates the Optoelectronic Response of Alloyed Perovskite Solar Cells. *Nat. Nanotechnol.* **2022**, *17*, 190–196.

(19) Smith, I. C.; Hoke, E. T.; Solis-Ibarra, D.; McGehee, M. D.; Karunadasa, H. I. A Layered Hybrid Perovskite Solar-Cell Absorber with Enhanced Moisture Stability. *Angew. Chem. Int. Ed.* **2014**, *53* (42), 11232–11235.

(20) Tsai, H.; Nie, W.; Blancon, J.-C.; Stoumpos, C. C.; Asadpour, R.; Harutyunyan, B.; Neukirch, A. J.; Verduzco, R.; Crochet, J. J.; Tretiak, S.; Pedesseau, L.; Even, J.; Alam, M. A.; Gupta, G.; Lou, J.; Ajayan, P. M.; Bedzyk, M. J.; Kanatzidis, M. G.; Mohite, A. D. High-Efficiency Two-Dimensional Ruddlesden–Popper Perovskite Solar Cells. *Nature* **2016**, *536* (7616), 312–316.

(21) Grancini, G.; Roldán-Carmona, C.; Zimmermann, I.; Mosconi, E.; Lee, X.; Martineau, D.; Narbey, S.; Oswald, F.; De Angelis, F.; Graetzel, M.; Nazeeruddin, M. K. One-Year Stable Perovskite Solar Cells by 2D/3D Interface Engineering. *Nat. Commun.* **2017**, *8* (1), 15684.

(22) Gharibzadeh, S.; Abdollahi Nejand, B.; Jakoby, M.; Abzieher, T.; Hauschild, D.; Moghadamzadeh, S.; Schwenzer, J. A.; Brenner, P.; Schmager, R.; Haghighirad, A. A.; Weinhardt, L.; Lemmer, U.; Richards, B. S.; Howard, I. A.; Paetzold, U. W. Record Open-Circuit Voltage Wide-Bandgap Perovskite Solar Cells Utilizing 2D/3D Perovskite Heterostructure. *Adv. Energy Mater.* **2019**, *9* (21), 1803699.

(23) Yuan, M.; Quan, L. N.; Comin, R.; Walters, G.; Sabatini, R.; Voznyy, O.; Hoogland, S.; Zhao, Y.; Beauregard, E. M.; Kanjanaboos, P.; Lu, Z.; Kim, D. H.; Sargent, E. H. Perovskite Energy Funnels for Efficient Light-Emitting Diodes. *Nat. Nanotechnol.* **2016**, *11* (10), 872–877.

(24) Yuan, S.; Cui, L.-S.; Dai, L.; Liu, Y.; Liu, Q.-W.; Sun, Y.-Q.; Auras, F.; Anaya, M.; Zheng, X.; Ruggeri, E.; Yu, Y.-J.; Qu, Y.-K.; Abdi-Jalebi, M.; Bakr, O. M.; Wang, Z.-K.; Stranks, S. D.; Greenham, N. C.; Liao, L.-S.; Friend, R. H. Efficient and Spectrally Stable Blue Perovskite Light-Emitting Diodes Employing a Cationic π-Conjugated Polymer. *Adv. Mater.* **2021**, *33* (45), 2103640.

(25) Shi, E.; Gao, Y.; Finkenauer, B. P.; Akriti; Coffey, A. H.; Dou, L. Two-Dimensional Halide Perovskite Nanomaterials and Heterostructures. *Chem. Soc. Rev.* **2018**, *47* (16), 6046–6072.

(26) Pan, D.; Fu, Y.; Spitha, N.; Zhao, Y.; Roy, C. R.; Morrow, D. J.; Kohler, D. D.; Wright, J. C.; Jin, S. Deterministic Fabrication of Arbitrary Vertical Heterostructures of Two-Dimensional Ruddlesden–Popper Halide Perovskites. *Nat. Nanotechnol.* **2021**, *16* (2), 159–165.

(27) Karpińska, M.; Jasiński, J.; Kempt, R.; Ziegler, J. D.; Sansom, H.; Taniguchi, T.; Watanabe, K.; Snaith, H. J.; Surrente, A.; Dyksik, M.; Maude, D. K.; Kłopotowski, Ł.;

Chernikov, A.; Kuc, A.; Baranowski, M.; Plochocka, P. Interlayer Excitons in $MoSe_2$/2D Perovskite Hybrid Heterostructures – the Interplay between Charge and Energy Transfer. *Nanoscale* **2022**, *14* (22), 8085–8095.

(28) Stoumpos, C. C.; Cao, D. H.; Clark, D. J.; Young, J.; Rondinelli, J. M.; Jang, J. I.; Hupp, J. T.; Kanatzidis, M. G. Ruddlesden–Popper Hybrid Lead Iodide Perovskite 2D Homologous Semiconductors. *Chem. Mater.* **2016**, *28* (8), 2852–2867.

(29) Li, X.; Hoffman, J. M.; Kanatzidis, M. G. The 2D Halide Perovskite Rulebook: How the Spacer Influences Everything from the Structure to Optoelectronic Device Efficiency. *Chem. Rev.* **2021**, *121* (4), 2230–2291.

(30) Fu, Y.; Hautzinger, M. P.; Luo, Z.; Wang, F.; Pan, D.; Aristov, M. M.; Guzei, I. A.; Pan, A.; Zhu, X.; Jin, S. Incorporating Large A Cations into Lead Iodide Perovskite Cages: Relaxed Goldschmidt Tolerance Factor and Impact on Exciton–Phonon Interaction. *ACS Cent. Sci.* **2019**, *5* (8), 1377–1386.

(31) Hautzinger, M. P.; Pan, D.; Pigg, A. K.; Fu, Y.; Morrow, D. J.; Leng, M.; Kuo, M.-Y.; Spitha, N.; Lafayette, D. P.; Kohler, D. D.; Wright, J. C.; Jin, S. Band Edge Tuning of Two-Dimensional Ruddlesden–Popper Perovskites by A Cation Size Revealed through Nanoplates. *ACS Energy Lett.* **2020**, *5* (5), 1430–1437.

(32) Christians, J. A.; Miranda Herrera, P. A.; Kamat, P. V. Transformation of the Excited State and Photovoltaic Efficiency of $CH_3NH_3PbI_3$ Perovskite upon Controlled Exposure to Humidified Air. *J. Am. Chem. Soc.* **2015**, *137* (4), 1530–1538.

(33) Cho, J.; DuBose, J. T.; Le, A. N. T.; Kamat, P. V. Suppressed Halide Ion Migration in 2D Lead Halide Perovskites. *ACS Materials Lett.* **2020**, *2* (6), 565–570.

(34) Wang, Y.-R.; Senocrate, A.; Mladenović, M.; Dučinskas, A.; Kim, G. Y.; Rothlisberger, U.; Milić, J. V.; Moia, D.; Grätzel, M.; Maier, J. Photo De-Mixing in Dion-Jacobson 2D Mixed Halide Perovskites. *Adv. Energy Mater.* **2022**, 2200768.

(35) Cho, J.; Mathew, P. S.; DuBose, J. T.; Kamat, P. V. Photoinduced Halide Segregation in Ruddlesden–Popper 2D Mixed Halide Perovskite Films. *Adv. Mater.* **2021**, *33*, 2105585.

(36) Jiang, F.; Pothoof, J.; Muckel, F.; Giridharagopal, R.; Wang, J.; Ginger, D. S. Scanning Kelvin Probe Microscopy Reveals That Ion Motion Varies with Dimensionality in 2D Halide Perovskites. *ACS Energy Lett.* **2021**, *6* (1), 100–108.

(37) Mathew, P. S.; DuBose, J. T.; Cho, J.; Kamat, P. V. Spacer Cations Dictate Photoinduced Phase Segregation in 2D Mixed Halide Perovskites. *ACS Energy Lett.* **2021**, *6* (7), 2499–2501.

(38) Seitz, M.; Meléndez, M.; York, P.; Kurtz, D. A.; Magdaleno, A. J.; Alcázar-Cano, N.; Kshirsagar, A. S.; Gangishetty, M. K.; Delgado-Buscalioni, R.; Congreve, D. N.; Prins, F. Halide

Mixing Inhibits Exciton Transport in Two-Dimensional Perovskites Despite Phase Purity. *ACS Energy Lett.* **2022**, *7* (1), 358–365.

(39) Ahmad, S.; Baumberg, J. J.; Vijaya Prakash, G. Structural Tunability and Switchable Exciton Emission in Inorganic-Organic Hybrids with Mixed Halides. *J. Appl. Phys.* **2013**, *114* (23), 233511.

(40) Lanty, G.; Jemli, K.; Wei, Y.; Leymarie, J.; Even, J.; Lauret, J.-S.; Deleporte, E. Room-Temperature Optical Tunability and Inhomogeneous Broadening in 2D-Layered Organic–Inorganic Perovskite Pseudobinary Alloys. *J. Phys. Chem. Lett.* **2014**, *5* (22), 3958–3963.

(41) Wright, N. E.; Qin, X.; Xu, J.; Kelly, L. L.; Harvey, S. P.; Toney, M. F.; Blum, V.; Stiff-Roberts, A. D. Influence of Annealing and Composition on the Crystal Structure of Mixed-Halide, Ruddlesden–Popper Perovskites. *Chem. Mater.* **2022**, *34* (7), 3109–3122.

(42) Akriti; Shi, E.; Shiring, S. B.; Yang, J.; Atencio-Martinez, C. L.; Yuan, B.; Hu, X.; Gao, Y.; Finkenauer, B. P.; Pistone, A. J.; Yu, Y.; Liao, P.; Savoie, B. M.; Dou, L. Layer-by-Layer Anionic Diffusion in Two-Dimensional Halide Perovskite Vertical Heterostructures. *Nat. Nanotechnol.* **2021**, *16*, 584–591.

(43) Akriti; Zhang, S.; Lin, Z.-Y.; Shi, E.; Finkenauer, B. P.; Gao, Y.; Pistone, A. J.; Ma, K.; Savoie, B. M.; Dou, L. Quantifying Anionic Diffusion in 2D Halide Perovskite Lateral Heterostructures. *Adv. Mater.* **2021**, *33* (51), 2105183.

(44) Roy, C. R.; Pan, D.; Wang, Y.; Hautzinger, M. P.; Zhao, Y.; Wright, J. C.; Zhu, Z.; Jin, S. Anion Exchange of Ruddlesden–Popper Lead Halide Perovskites Produces Stable Lateral Heterostructures. *J. Am. Chem. Soc.* **2021**, *143* (13), 5212–5221.

(45) Motti, S. G.; Crothers, T.; Yang, R.; Cao, Y.; Li, R.; Johnston, M. B.; Wang, J.; Herz, L. M. Heterogeneous Photon Recycling and Charge Diffusion Enhance Charge Transport in Quasi-2D Lead-Halide Perovskite Films. *Nano Lett.* **2019**, *19* (6), 3953–3960.

(46) deQuilettes, D. W.; Frohna, K.; Emin, D.; Kirchartz, T.; Bulovic, V.; Ginger, D. S.; Stranks, S. D. Charge-Carrier Recombination in Halide Perovskites. *Chem. Rev.* **2019**, *119* (20), 11007–11019.

(47) Dexter, D. L. A Theory of Sensitized Luminescence in Solids. *J. Chem. Phys.* **1953**, *21* (5), 836–850.

(48) Inokuti, M.; Hirayama, F. Influence of Energy Transfer by the Exchange Mechanism on Donor Luminescence. *J. Chem. Phys.* **1965**, *43* (6), 1978–1989.

(49) Van Uitert, L. G.; Johnson, L. F. Energy Transfer between Rare-earth Ions. *J. Chem. Phys.* **1966**, *44* (9), 3514–3522.

(50) Gandrud, W. B.; Moos, H. W. Rare-Earth Infrared Lifetimes and Exciton Migration Rates in Trichloride Crystals. *J. Chem. Phys.* **1968**, *49* (5), 2170–2182.

(51) Liu, Y.; Wang, M.; Ievlev, A. V.; Ahmadi, A.; Keum, J. K.; Ahmadi, M.; Hu, B.; Ovchinnikova, O. S. Photoinduced Iodide Repulsion and Halides-Demixing in Layered Perovskites. *Materials Today Nano* **2022**, *18*, 100197.

(52) Pankove, J. I. *Optical Processes in Semiconductors*; Dover Publications, 2012.

(53) Shi, E.; Yuan, B.; Shiring, S. B.; Gao, Y.; Akriti; Guo, Y.; Su, C.; Lai, M.; Yang, P.; Kong, J.; Savoie, B. M.; Yu, Y.; Dou, L. Two-Dimensional Halide Perovskite Lateral Epitaxial Heterostructures. *Nature* **2020**, *580* (7805), 614–620.

(54) Lanzetta, L.; Marin-Beloqui, J. M.; Sanchez-Molina, I. S.; Ding, D.; Haque, S. A. Two-Dimensional Organic Tin Halide Perovskites with Tunable Visible Emission and Their Use in Light-Emitting Devices. *ACS Energy Lett.* **2017**, *2* (7), 1662-1668.

Chapter 3. Utilizing Halide Immiscibility to Fabricate Lateral Halide Heterojunctions in Ruddlesden–Popper Lead Halide Perovskites[a]

3.1. Introduction

Lead halide perovskites (LHPs) have found many promising applications in solution-processable photovoltaics, light-emitting diodes (LEDs), and other optoelectronic devices[1–3] owing to their high optical densities, long charge carrier diffusion lengths, and superb defect-tolerant performance.[4,5] The most studied three-dimensional (3D) LHPs have the formula of $APbX_3$, where A is a monovalent cation and X is a halide. They readily form solid solutions of halide ions continuously spanning from the narrow band gap (~1.6 eV) iodide LHPs to wide band gap chloride LHPs (~2.9 eV).[2,6] Building on such tunable semiconductor materials, one would have envisioned the fabrication of semiconductor heterostructures that can allow the manipulation of charge carriers and serve as the foundations for high performance optoelectronic devices, analogous to heterostructures based on III-V semiconductors.[7] However, halide-based $APbX_3/APbBX'_3$ heterojunctions have been shown to interdiffuse to form alloyed $APb(X/X')_3$ spontaneously over time at room temperature, which is accelerated under extrinsic perturbations such as higher temperatures or illumination.[8–10] Moreover, mixed halide 3D LHPs could phase separate into thermodynamically favorable phases with different halide (or A cation) compositions under excitation.[11–14] Such facile anion diffusion and instability have prevented the studies and applications of halide perovskite heterostructures.

---

[a] This chapter was originally published as an article (*J. Am. Chem. Soc.* **2021**, *143*(13), 5212-5221.) in collaboration with Dongxu Pan, Yining Wang, Matthew P. Hautzinger, Yuzhou Zhao, John C. Wright, Zihua Zhu, and Song Jin.

Ruddlesden–Popper perovskites (RPPs)[15] could be more promising building blocks for making heterostructures than 3D perovskites. RPPs are a family of quasi-2D layered semiconductors with the general formula $(LA)_2(A)_{n-1}Pb_nX_{3n+1}$, consisting of n layers of inorganic corner-sharing Pb-X octahedra separated by bilayers of large organic spacer cations (LA) like *n*-butylammonium (BA). RPPs have better environmental resilience than 3D perovskites,[16] yet also exhibit more tunable optoelectronic properties through controllable quantum confinement of the Pb-X sheets (n value),[17,18] the structural and electronic characteristics of the spacer cations,[19,20] and to a lesser degree the A-site cations.[21,22] RPPs' utility in photovoltaics,[16,23] LEDs,[24,25] and photodetectors has been demonstrated with performance competitive with—and at times superior to—3D LHPs.[3,26] The layered crystal structures of RPPs lead to anisotropic physical behaviors different from 3D LHPs, such as strongly confined excitons[15,18] and anisotropic carrier mobility.[23,27] More importantly, the layered structures make the ion diffusion behaviors in RPPs substantially different from those in 3D perovskites and dependent on lattice directions.[28–32] Specifically, the organic spacer cations appear to impede anion diffusion across RPP layers.

Such structural attributes of RPPs have recently enabled the preparation of "vertical" van der Waals heterostructures of RPPs by mechanical stacking[33] or direct growth,[34] but "lateral" heterostructures within the inorganic layers of RPPs are more challenging. Recently, lateral halide heterostructures in 2D $(LA)_2PbX_2$ perovskites (i.e., only $n = 1$) were synthesized by sequentially growing $(LA)_2PbI_4$ epitaxially along the edges of $(LA)_2PbBr_4$ nanosheets.[35] Despite this success, the complex and dynamic equilibrium between RPPs of different n phases[24,34,36] makes the direct growth of lateral heterostructures of RPPs with $n > 1$ challenging because the second synthesis step could shuffle the pure RPP n phase formed in the first step. An alternative and perhaps more general approach to prepare lateral heterostructures of RPPs could be halide anion exchange

starting from various phase-pure RPP phases after they are synthesized, as some earlier reports of post-synthetic modifications of RPP materials using either halide salt vapor or halogen gas suggest that the RPP lattices could be preserved.[37] Contrasting with the isotropic anion exchange well studied in 3D LHPs,[8,9,38–40] the expected anisotropy between ion diffusion along the basal planes versus the out-of-plane direction in RPPs presents much more complexity with many potential controlling variables that remain unexplored. For example, would the quantum well thickness of the RPP phases (the *n* value) affect the chemical behaviors of anion exchange? This and other structural parameters of RPP also introduce potential opportunities for synthetic control over ionic diffusion to enable heterostructures that demands further systematic study.

Here we show how the layered structures of RPPs affect the morphological outcomes of vapor-solid anion exchange of single-crystal RPP microplates with hydrogen bromide (HBr) vapor to make lateral heterostructures of RPPs. We discover that sharp and stable lateral halide heterojunctions can be formed for a wide range of $n = 1$ and $n = 2$ RPPs because of halide immiscibility; however, diffuse gradient junctions are formed for RPPs with higher *n*, closer to the ion interdiffusion behaviors in 3D perovskites. We then illustrate how the identities of LA cations and A cations in RPPs can influence their anion exchange behaviors, the kinetics of the anion exchange process, as well as the enhanced stability of the resulted lateral heterostructures, laying the groundwork for post-synthetic preparation of stable lateral heterostructures from arbitrary RPP materials.

3.2. Vapor-Solid Anion Exchange in Ruddlesden–Popper Lead Halide Perovskites

We first synthesized well-faceted microplates of several RPPs $(LA)_2(A)_{n-1}Pb_nI_{3n+1}$, where LA = *n*-hexylammonium (HA), *n*-butylammonium (BA), or phenethylammonium (PEA); A = methylammonium (MA), formamidinium (FA), or guanidinium (GA), via growth from aqueous

precursor solution droplets[33,41] or an organic solution dissolution-reprecipitation method (herein referred to as "solution transport")[34,42] (see methods and Figure A2.1 in Appendix 2 for details). The microplates are tens of microns in lateral dimensions and a few hundred nanometers up to a few micrometers thick (Figure A2.2). These microplates have well defined shapes and easily identifiable facets suitable for investigating structural influences on anisotropic anion exchange. For brevity, RPP formulas are denoted using the modular notation n = i LA-A-Pb-X, with heterostructures of these materials notated as n = i LA-A-Pb-X/X'. To perform the halide exchange, we exposed these RPP microplates to a controlled flow of HBr vapor at room temperature in a gas flow reactor for specified periods of time (see methods and Figure A2.3 in Appendix 2 for details). The H^+ cations are too small to be suitable A-cations in perovskite structures so that HBr will not shift the delicate equilibrium between RP perovskite n phases, and the HBr exchange reaction does not involve redox chemistry.

We found that the layered structure of RPPs makes the anion exchange kinetics substantially faster in the lateral direction along the basal planes of the Pb-X networks than in the vertical out-of-plane direction across the organic LA bilayers (Figure 3.1a). This is immediately apparent from the color change inward from the edges of the microplates as Br^- replaces I^- in a series of n = 1 - 4 HA-MA-Pb-I RPP microplates (Figure 3.1b-e). There are also fundamental differences among the anion exchange behaviors of different RPP n phases (Figure 3.1a): n = 1 and n = 2 microplates display sharp heterojunctions (Figure 3.1b,c), but gradients of colors are observed toward the edges of n = 3 and n = 4 microplates (Figure 3.1d,e).

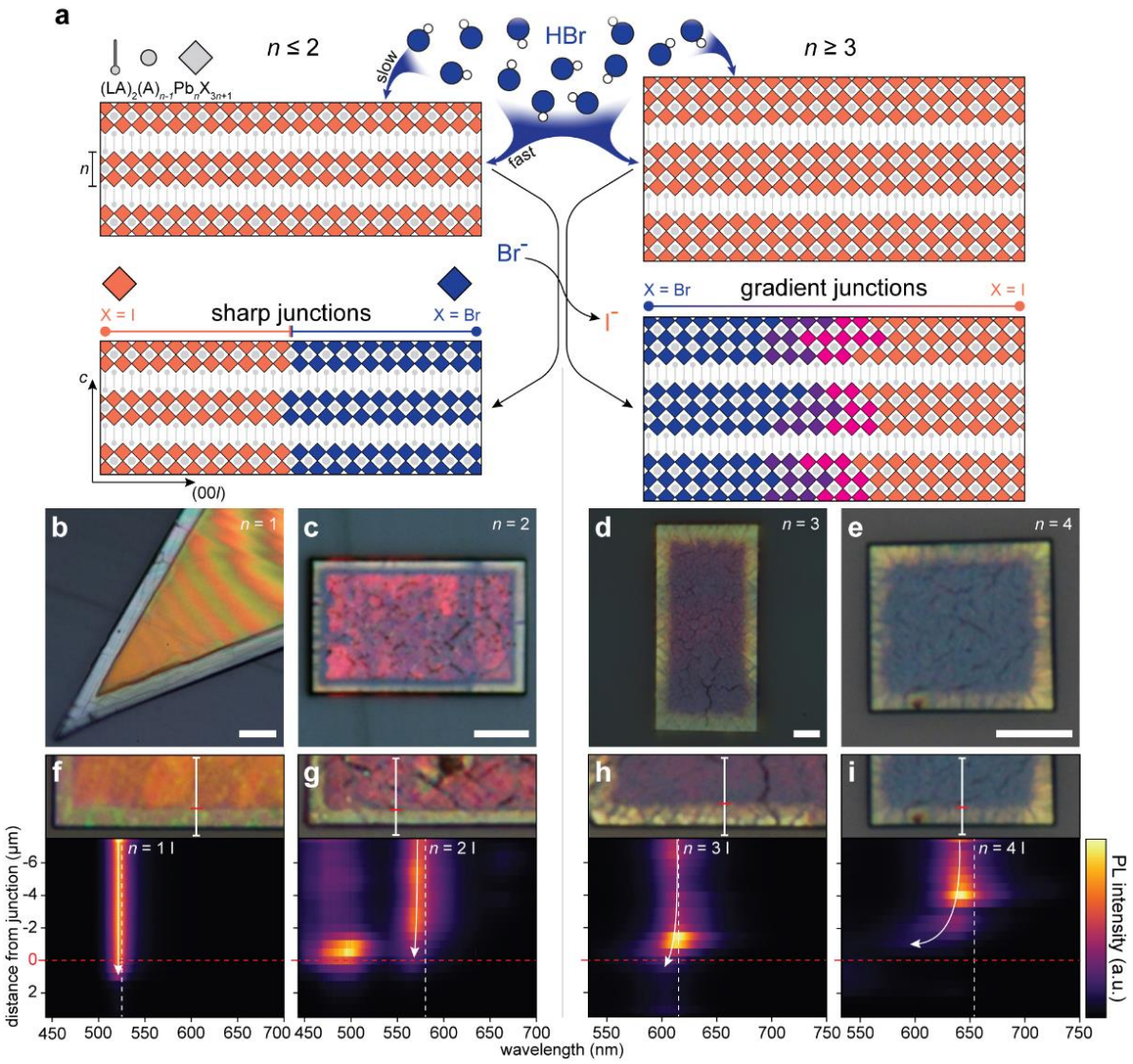

Figure 3.1. Lateral heterostructures from anion exchange in Ruddlesden–Popper perovskites. **(a)** Scheme depicting the differing outcomes of vapor-solid anion exchange in lead iodide RPPs using HBr vapor that depend on RPP layer thickness: when n ≤ 2, sharp junctions are formed; when n ≥ 3, gradient junctions are formed. Blue and red diamonds represent $[PbBr_6]^{4-}$ and $[PbI_6]^{4-}$ octahedra, respectively. **(b-e)** Optical micrographs of representative I/Br heterostructures produced by anion exchange of the homologous series of $(HA)_2(MA)_{n-1}Pb_nI_{3n+1}$ RPPs (n = 1 - 4): **(b)** $(HA)_2PbI_4$, **(c)** $(HA)_2(MA)Pb_2I_7$, **(d)** $(HA)_2(MA)_2Pb_3I_{10}$, **(e)** $(HA)_2(MA)_3Pb_4I_{13}$. All scale bars are 10 μm. **(f-i)** PL line scans corresponding to the 12 μm traces on optical images of the heterointerfaces for the

corresponding $(HA)_2(MA)_{n-1}Pb_nI_{3n+1}$ RPPs shown above the plots. (f,g) were collected under 442 nm excitation; (h,i) were collected under 532 nm excitation. Vertical dashed reference lines indicate the characteristic emission wavelengths for pure $(HA)_2(MA)_{n-1}Pb_nI_{3n+1}$ RPPs. White arrows are visual guides to track wavelength shifts of the peaks as the boundary is crossed.

We further examined this difference using confocal photoluminescence (PL) line scans across the lateral phase boundaries of each I/Br heterostructure (Figure 3.1f-i). The bromide analogues of each RPP phase have blue-shifted PL due to a composition-dependent bandgap that follows Vegard's law; thus, a continuous change in halide composition across the heterojunction would be expected to result in gradual shifting of a single PL peak as the halide interface is crossed. Instead, $n = 1$ and $n = 2$ RPPs showed an abrupt disappearance of their iodide phase peaks (~525 nm for $n = 1$ in Figure 3.1f and ~580 nm for $n = 2$ in Figure 3.1g) with no observable blueshift across the heterojunctions. The 442 nm exciting laser has insufficient energy to excite $n = 1$ & 2 Br RPPs (with expected PL peaks around 410 and 445 nm, respectively), but the lack of peak shifts across these heterostructures (Figure 3.1f,g) are strong evidence for the discontinuity of the interfaces. In the $n = 2$ case, there is also trace emission from 460-500 nm that corresponds to an emissive defect that is also seen in pure $n = 2$ Br phases (Figure A2.4c).[43] In contrast, for $n \geq 3$ RPPs, blue-shifting of the original iodide phase peaks were clearly observed across the I/Br interfaces of the heterostructures (Figure 3.1h-i), which resembles halide mixing observed in 3D LHPs.[39] We used a 532 nm exciting laser for the $n \geq 3$ heterostructures because blue-shifted emission (around 520 nm) from the surface of the microplates dominates the spectra under 442 nm excitation (Figure A2.5c, e). Nonetheless, the spectra observed under 532 nm excitation confirmed the presence of increasingly bromide-rich phases toward the edges.

The discontinuous interfaces observed in $n \leq 2$ RPPs are a stark contrast to the anion exchange behaviors seen in 3D LHPs, which exhibit halide miscibility under standard conditions.[39,40] We have further confirmed this behavior in these experiments: HBr vapor exchange on $MAPbI_3$ produces 3D halide interfaces that are isotropic and continuous (Figure A2.6) as a consequence of Fick-like ion diffusion. But even the interfaces of $n \geq 3$ RPP heterostructures show some signs of discrete peak transitions through the individual spectra across the boundaries (Figure A2.7). This suggests step-wise transitions in halide miscibility between 3D LHPs and RPPs: as the dimensionality of LHPs is reduced from 3D ($n = \infty$) to 2D ($n = 1$), the formation of solid solutions of mixed halide perovskites becomes increasingly difficult, ultimately arriving at an immiscible, binary phase system (either pure iodide or bromide phases) in the cases of $n = 2$ and $n = 1$ RPPs to form heterojunctions with sharp interfaces.

3.3. Influence of Various Spacer Cations on Anion Exchange in Ruddlesden–Popper Perovskites

The diverse compositional and structural parameters of RPPs can also influence the anion exchange behaviors. This multi-dimensional RPP phase space can be visualized in Figure 3.2a using LA cations, A cations, and n value as 3 independent axes. Having revealed the effects of changing n value above (for the specific HA-MA RPPs), we now examine the effects of LA and A cations for the $n \leq 2$ RPPs that exhibit sharp heterojunctions.

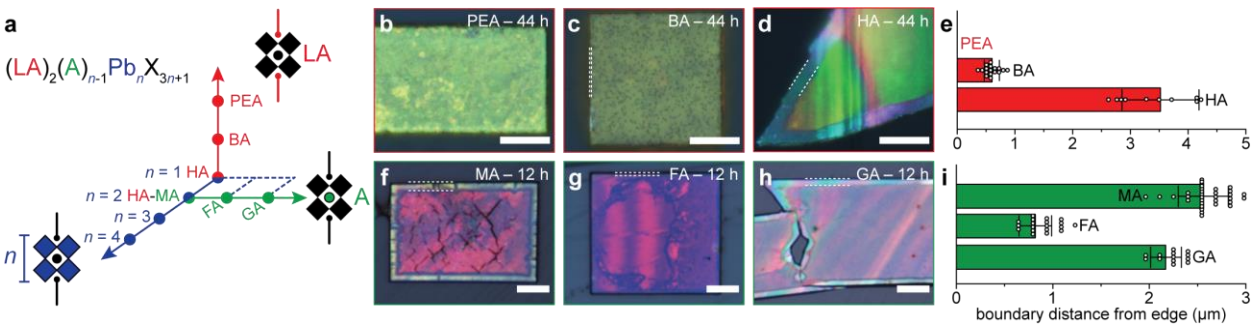

Figure 3.2. Different anion exchange behaviors in RPPs with various spacer (LA) and A-cations. **(a)** Pseudo-coordinate mapping of the compositional phase space of lead halide RPPs. **(b-d)** Optical micrographs of $n = 1$ $(LA)_2PbI_4$ microplates with decreasingly rigid LA spacer cations: **(b)** PEA, **(c)** BA, **(d)** HA, after 44 h of anion exchange with HBr vapor in the same reactor. **(f-h)** Optical micrographs of $n = 2$ $(HA)_2(A)Pb_2I_7$ RPPs with increasingly large A-site cations: **(f)** MA, **(g)** FA, **(h)** GA, after 12 h of anion exchange with HBr vapor. MA and GA samples were in the same reactor. For (b-d) and (f-h), dashed lines mark the edges and junctions of the resulting heterostructures, and all scale bars are 10 μm. **(e, i)** Statistics of the boundary propagation distance for various **(e)** LA spacer cations and **(i)** A-cations. Error bars represent sample standard deviations. White dots represent individual measurements.

Three $n = 1$ $(LA)_2PbI_4$ samples with different LA cations (PEA, BA, HA) show large differences in exchange rates (Figure 3.2b-d). After 44 h of anion exchange, multiple microns of exchanged bromide phase were visible in the HA microplates (Figure 3.2d), but no noticeable exchange occurred in the PEA microplates (Figure 3.2b). The BA microplates had small amounts of exchanged bromide phase present at their edges (Figure 3.2c), but substantially less than HA microplates. The spacer cations clearly have great influence on the rate of the exchange reactions: the more rigid PEA spacer cations[15] drastically hinder the anion exchange, if permitting it at all (Figure 3.2e). We hypothesize that the rigidity of the interlayer space could affect the permeability of HBr molecules into RPPs. Additionally, anion diffusion must be mediated by structural point defects.[29,44] The rigidity of the LA cation could impact the freedom of structural rearrangements within the Pb-X networks and inhibit the ionic exchange in rigidly templated RPPs (such as those containing PEA).

We further compared the exchange behaviors of n = 2 HA-A-Pb-I RPPs with 3 A-site cations of increasing effective radius: MA, FA, and GA.[21,22] After 12 h of exchange, all 3 samples showed noticeable change at the edges (Figure 3.2f-h). The phase boundaries propagate significantly faster in MA and GA RPPs than in FA RPP (Figure 3.2i), but the differences in exchange rates among A-cations are less pronounced than those among spacer cations. The resulting lateral heterostructures also displayed different visual quality, with extensive cracking observed across the surfaces of the MA RPP microplates (Figure 3.2g). This could stem from edge dislocations induced by lattice mismatch at the halide interface, but the exact cause remains unclear. This survey shows that the highest quality lateral RPP heterostructures can be prepared from $n \leq 2$ RPPs containing less rigid spacer cations like HA and A-cations like FA or GA, whereas this vapor-solid exchange method may not yield lateral heterostructures of RPPs containing rigidly packed spacer cations like PEA. These insights can also guide potential direct growth of lateral heterostructures and the previously reported success in sequentially growing lateral heterostructures of n = 1 $(LA)_2PbBr_4$ - $(LA)_2PbI_4$[35] is consistent with our findings.

3.4. Kinetic Characteristics of the Anion Exchange Reaction

These comprehensive findings motivate us to examine the exchange reaction of the n = 2 RPP model systems in detail. We visualized the time evolution of the vapor-solid exchange reaction by directly monitoring individual n = 2 HA-FA-Pb-I microplates as anion exchange progressed (Figure 3.3a). At the beginning, the hue uniformly changed across the surface of the microplates, which likely stems from some anion exchange happening on the surface (Figure A2.8d). After approximately 9 h, the first signs of a grey secondary phase appeared at the edges of the microplates, which then changed in hue to light green until a clearly visible junction formed after approximately 25 h. The junction then propagated inward from the edges, retaining its sharpness

throughout. After 81 h, the exchanged bromide rim of the plate with light green color was very prominent and the vertical component of the anion exchange was also sufficiently extensive that the reflected color became dominated by the bromide surface. Interestingly, the structural imperfections in the microplate remained unperturbed as the exchanged phase propagated through them (see Figure A2.9). Additionally, a control sample of $n = 2$ HA-FA-Pb-I microplates left in the ambient over the same timeframe (Figure 3.3b and Figure A2.10) showed extensive degradation, as evidenced by blemishes across the top surface and edges of the microplate. Such contrasting environmental stability suggests that, despite the inevitable presence of moisture in the HBr vapor, the HBr exchange reaction inhibits the normal degradation process in iodide RPPs.

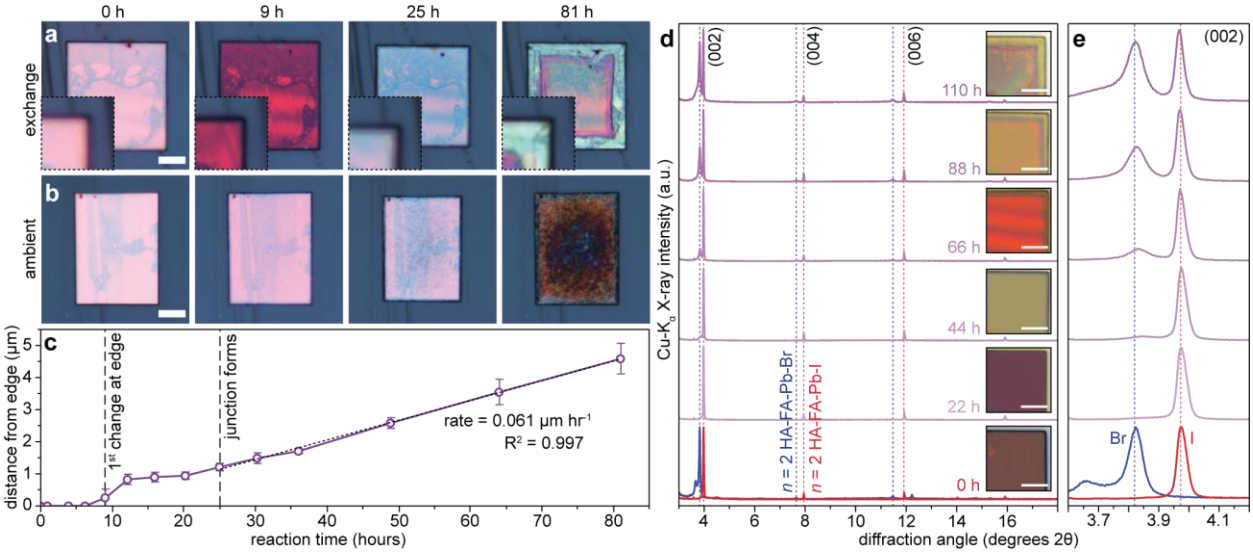

Figure 3.3. Evolution of anion exchange in $(HA)_2(FA)Pb_2I_7$ microplates. **(a,b)** Optical micrographs comparing the temporal evolution of two microplates as one **(a)** underwent anion exchange with HBr vapor and the other **(b)** was left in ambient environment. **(c)** Inward propagation of the I–Br lateral phase boundary over time from a sample of microplates undergoing exchange simultaneously with the one shown in (a). Error bars represent sample standard deviations. The trendline is the linear fit of the time points following pronounced junction

formation. **(d)** PXRD patterns of an $(HA)_2(FA)Pb_2I_7$ microplate sample after undergoing anion exchange for increasing periods of time (from 22 h to 110 h), in comparison to the PXRD patterns of pure $(HA)_2(FA)Pb_2I_7$ and $(HA)_2(FA)Pb_2Br_7$. **(e)** Detailed view of the evolving (002) reflections from (d). The dashed red and blue reference lines correspond to the (00*l*) reflections of pure $(HA)_2(FA)Pb_2I_7$ and $(HA)_2(FA)Pb_2Br_7$, respectively. The inset optical images show the corner of a single microplate in the sample on which XRD analysis was performed. All scale bars are 10 μm. Inset images in (a) are 10 μm × 10 μm.

The most remarkable feature of this anion exchange reaction is the retention of the junction's sharpness as it propagates inward. This does not follow Fick's laws of diffusion observed in 3D perovskites[9,39,40] and suggests that a solid-solid interdiffusion mechanism is not at play in $n \leq 2$ RPPs. Instead, we use a simplified gas-solid exchange reaction to model the process:

$$(HA)_2(FA)Pb_2I_7\ (s) + 7\ HBr\ (g) \rightarrow (HA)_2(FA)Pb_2Br_7 + 7\ HI\ (g)$$

with an associated rate law:

$$\frac{d\ (\mathrm{BrRPP})}{dt} = \alpha_{\mathrm{IRPP}}^{a}\alpha_{\mathrm{HBr}}^{b}$$

where α is the activity of each of the species and a and b are the reaction orders for each species. Since the stoichiometric conversion of iodide RPP (IRPP) to bromide RPP (BrRPP) is one-to-one and the associated change in lattice constants is small (according to the reported crystal structures of the BA RPPs[41,43,45]), the propagation of the phase boundary from the plate edge is linearly proportional to the progression of the reaction itself. Thus, we utilize the sharp junction as a "marker plane" to track the reaction progress over time in a specific microplate (Figure 3.3c). The bromide phase did not propagate inward for at least 10 h after it emerged. Following the onset of a visible junction around 25 h, however, the boundary began to propagate linearly with time

(Figure 3.3c), correspondent to a 0^{th} order rate law. The solid RPP has an activity of unity because it is the medium within which the reaction occurs, therefore, a 0^{th} order rate law suggests that a saturation of HBr at the reaction interface must be achieved from the early hours of the exchange reaction.

We also collected X-ray diffraction (XRD) patterns of $(HA)_2(FA)Pb_2I_7$ microplates as they underwent the exchange to elucidate structural changes accompanying the exchange reaction (Figure 3.3d). Initially, only the (00*l*) reflections of $(HA)_2(FA)Pb_2I_7$ are visible, but after 66 h the equivalent (00*l*) reflections of $(HA)_2(FA)Pb_2Br_7$ emerge in tandem. As the phase boundary begins to propagate inward from the edges of the microplates (Figure 3.3d insets), the Br:I peak intensity ratio increases (Figure 3.3e) with no notable peak shifts from either the evolving bromide phase or the iodide starting material. These two discrete iodide and bromide PXRD peak positions, instead of a gradual shift of peak positions, further confirms that mixed I-Br (or alloyed) $n = 2$ RPP does not form under our exchange conditions. Furthermore, the 0^{th} order reaction kinetics suggests that the halide exchange itself is the rate-limiting step. In 3D LHPs, there is a low thermodynamic barrier to halide substitution, which renders the diffusion of the secondary halides at the surface or within the lattice as the possible the rate-limiting steps, but the results here point to a substantially higher energy barrier to halide mixing in RPPs.

3.5. Characterization of Sharp Lateral Heterostructures

We further characterized the resulting highest quality $n = 2$ HA-FA-Pb-I/Br RPP heterostructures with sharp junctions using (confocal) PL mapping, time-of-flight secondary ion mass spectrometry (ToF-SIMS), and energy dispersive X-ray spectroscopy (SEM-EDS). The binary interface can be clearly seen in the optical and PL micrographs (Figure 3.4a,b), with no colorimetric shifts in PL across the phase boundary. Confocal PL maps of a heterostructure at the

characteristic emission wavelengths of 445 nm for $(HA)_2(FA)Pb_2Br_7$ (Figure 3.4c) and 580 nm for $(HA)_2(FA)Pb_2I_7$ (Figure 3.4d) RPPs showed that the two emitting regions are spatially adjacent and non-overlapping, again confirming the compositions of the inner and outer components of the lateral heterostructure as pure single halide phases.

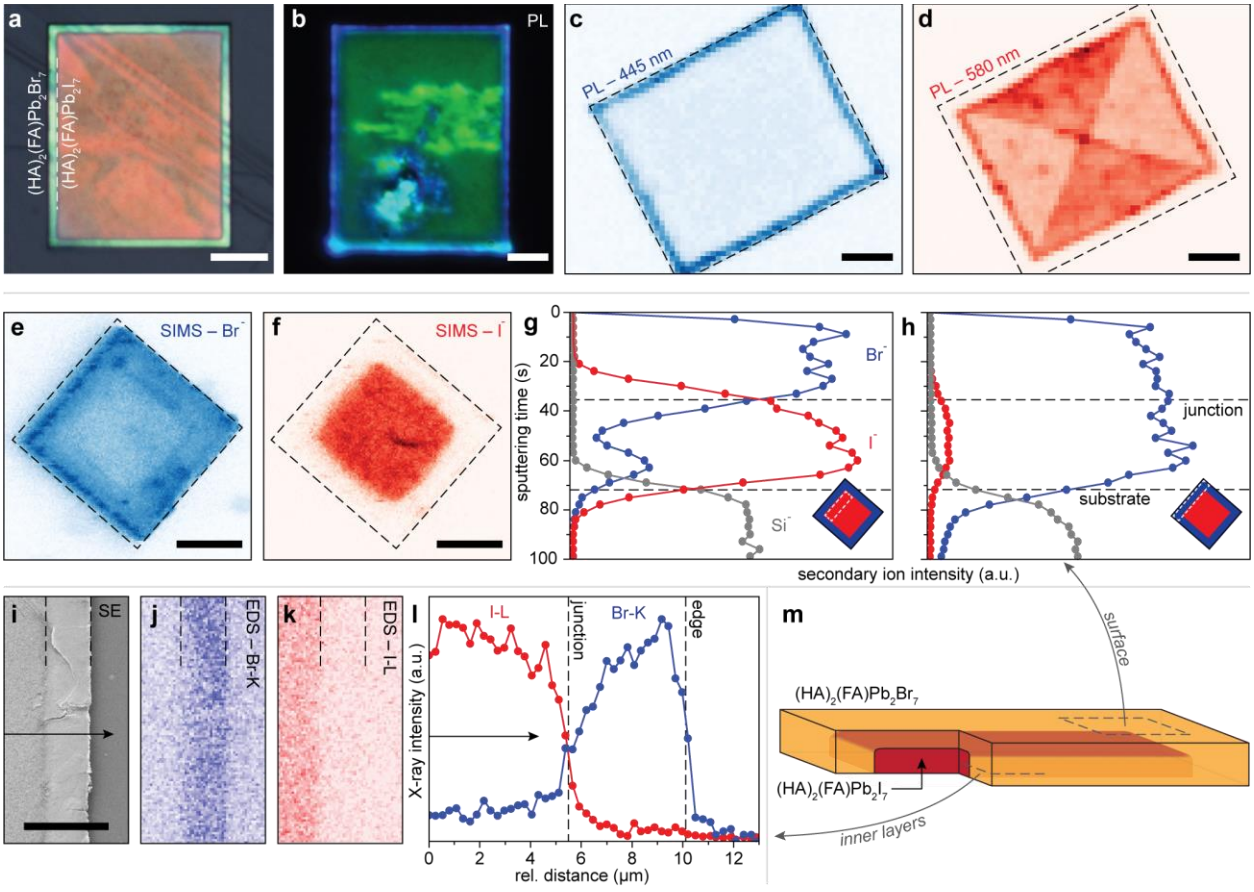

Figure 3.4. Structural characterization of exchanged lateral heterostructures starting from $(HA)_2(FA)Pb_2I_7$. **(a,b)** Optical micrographs of representative n = 2 HA-FA-Pb-I/Br lateral heterostructures under **(a)** visible light and **(b)** 385 nm LED illumination. **(c,d)** Confocal PL maps of a lateral heterostructure under 442 nm excitation within the characteristic emission regions for **(c)** n = 2 Br (445 nm) and **(d)** n = 2 I RPPs (580 nm). **(e,f)** ToF-SIMS halide maps of a lateral heterostructure showing **(e)** bromide and **(f)** iodide signal intensities. Dashed outlines in (c-f)

represent the spatial footprints of the microplate. **(g,h)** SIMS sputtering profiles collected at the **(g)** inner and **(h)** outer components of the heterostructure imaged in (e,f). Inset cartoons indicate the sputtering areas as dashed boxes. **(i)** Top-down SEM image of an exfoliated layer of a lateral heterostructure with the corresponding halide EDS maps at **(j)** Br-K and **(k)** I-L characteristic X-Ray energies. **(l)** EDS line scan corresponding to the arrow in (i). **(m)** Illustration of the 3D morphology of an exchanged $n = 2$ HA-FA-Pb-I/Br heterostructure showing a cross section. The vertical dimension is disproportionately large in scale to emphasize detail. All scale bars are 10 μm.

We further used ToF-SIMS to examine both in-plane and out-of-plane composition profiles of this heterostructure (Figure 3.4e-h). Secondary ion maps of a $n = 2$ HA-FA-Pb-I/Br microplate confirm the presence of bromide across its entire top surface (Figure 3.4e), whereas iodide is exclusively present in the center of the microplate (Figure 3.4f). ToF-SIMS sputtering profiles were collected through the depth of the heterostructure. The center profile (Figure 3.4g) shows that the upper fraction of the microplate contains only bromide, with an increase of iodide and decrease of bromide concentration beginning approximately one third into the total depth of the plate. The edge sputtering profile (Figure 3.4h), however, is dominated by bromide throughout the entire depth of the plate. EDS mapping performed on a heterostructure after the top layer was exfoliated (Figure 3.4j-l) eliminated the convolution from the bromide-rich top surface. The EDS maps confirm the sharp lateral interface, and the EDS line scan across the same interface (Figure 3.4l) shows a transition from I to Br over a distance of ~2 μm, setting an upper limit to the diffuseness of the heterojunction. We were unable to measure the height of the specific microplate studied with ToF-SIMS but based on atomic force microscopy (AFM) measurements and optical imaging of similar $n = 2$ HA-FA-Pb-I/Br lateral heterostructures (Figure A2.11), we can estimate a lateral

anion exchange distance exceeding an order of magnitude greater than the possible vertical exchange depth, which is limited to the height of the microplate (see additional discussion associated with Figure A2.11). These results suggest a core-shell "3D" heterostructure morphology with an overwhelming lateral bias, as illustrated in Figure 3.4m. An important consequence of the non-zero vertical anion exchange is that top-down exchange could dominate over lateral exchange in exceedingly thin nanosheets (see an example in Figure A2.8d), presenting a potential method to completely exchange the halide ions of some RPP starting materials with spatial control using patterned masks.

3.6. Stability of Lateral RPP Heterostructures

Finally, these lateral RPP heterostructures with sharp interfaces formed by anion exchange are more stable against anion interdiffusion and degradation. Again using n = 2 HA-FA-Pb-I/Br heterostructures as a model system, we first assessed the effects of temperature by heating two separate lateral heterostructure samples in an oven for 12 h at temperatures of 50 and 100 °C (Figure 3.5a-c). Surprisingly, the boundary between the iodide and bromide phases remained sharp even under elevated temperatures of 50 °C (Figure 3.5b), which is harsher than the operating conditions of many optoelectronic devices, and there was no noticeable sign of general degradation in comparison with the starting microplates (Figure 3.5a). Even at 100 °C (Figure 3.5c), the phase boundary remained mostly intact, but there was extensive warping and striations across the microplate, suggesting that the interdiffusion threshold of the junction is comparable to the structural degradation threshold of the RPP materials. We also kept an unencapsulated sample of these heterostructures in a sealed petri dish with desiccant for 116 days to evaluate environmental stability (Figure 3.5d). There was some surface degradation as evidenced by spot-like blemishes, but even after 116 days, the basic lateral heterostructure morphology retained and the microplate

had not yet degraded to the extent that the starting $(HA)_2FAPb_2I_7$ microplates did in under 100 h under ambient conditions (Figure 3.3b). The junction of the pictured specimen showed a third yellow-colored band toward the edges of the microplate. PL line scans of an analogous ternary junction after exfoliation (Figure A2.5h) showed that the new feature was likely a mixed halide phase, suggesting that some ion interdiffusion may have eventually occurred over such an extended duration.

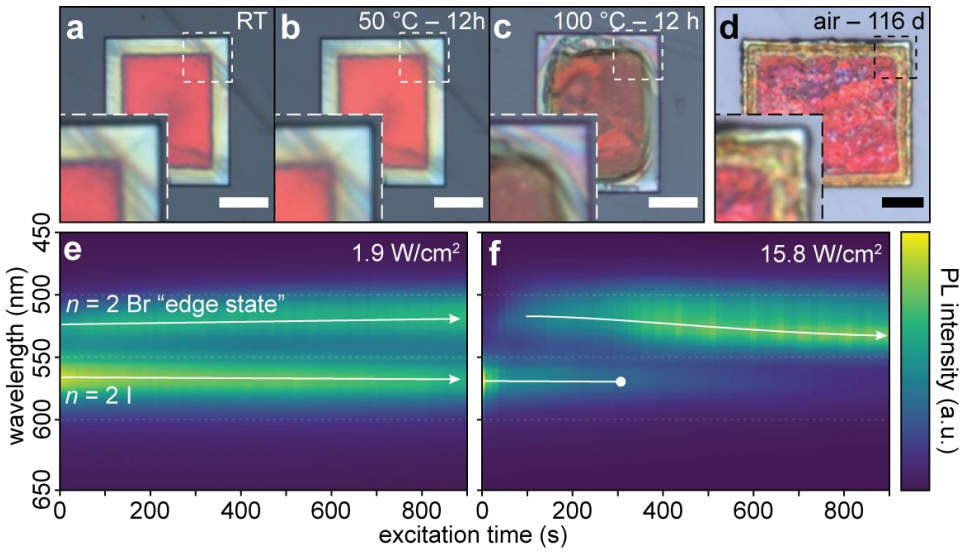

Figure 3.5. Stability of lateral RPP heterostructures after anion exchange from $(HA)_2(FA)Pb_2I_7$. **(a-c)** Optical micrographs n = 2 HA-FA-Pb-I/Br lateral heterostructures after being held at increasing temperatures for extended periods: **(a)** room temperature at the start, **(b)** at 50 °C for 12 h, **(c)** at 100 °C for 12 h. **(d)** Optical micrograph of an n = 2 HA-FA-Pb-I/Br lateral heterostructure left in desiccated air for 116 d. Bottom-left insets in (a-d) show magnified 10 × 10 μm corner regions highlighted in the corresponding micrographs with dashed boxes. All scale bars are 10 μm. **(e,f)** Temporal evolution of PL spectra from an exfoliated junction of an n = 2 HA-FA-Pb-I/Br lateral heterostructure under confocal 442 nm CW excitation at **(e)** low (1.9 W/cm^2) and **(f)** high

irradiance (15.8 W/cm^2). White arrows are visual guides to track spectral shifts and feature onsets over time.

Photoinduced ion diffusion is also a significant source of degradation for halide perovskite heterojunctions.[13] We focused a 442 nm CW laser onto the junction of an exfoliated layer of the lateral heterostructure and monitored PL spectral changes over the course of the 15 min excitation period. Under lower laser irradiance (1.9 W/cm^2, ~18 suns' equivalent) the spectra remained the same throughout (Figure 3.5e), but under much more intense irradiance (15.8 W/cm^2, ~150 suns' equivalent) significant spectral changes were observed (Figure 3.5f): the intensity of the characteristic $n = 2$ I emission peak at 580 nm significantly diminished. Concurrently, the 525 nm peak associated with a Br RPP edge state[43] began to intensify and red-shift, indicating that the junction was changing over time. Inspection of the microplate after the experiment revealed no significant physical damage, suggesting that the PL spectral changes were likely caused by compositional changes induced by the excitation.

These results show that these lateral halide heterojunctions of RPPs are much more stable than the halide junctions in 3D LHPs in that they display dramatically suppressed anion interdiffusion (but not eliminating it) along both basal plane and out-of-plane directions. Additionally, the enhanced environmental resilience of the RPP heterostructures compared to starting lead iodide RPP materials suggests that the bromide-rich RPP surfaces are more robust, making anion exchange a convenient approach for stabilizing iodide RPP surfaces.

3.7. Conclusion

We have shown that the anisotropic anion exchange behaviors in RPPs substantially and systematically differ from those in 3D LHPs as a function of decreasing perovskite layer thickness due to increasing halide immiscibility in these 2D structures. These attributes enable the formation

of sharp halide lateral heterostructures of $n = 1$ and 2 RPP phases via anion exchange. In contrast, RPPs with $n \geq 3$ form more diffuse compositional gradients upon anion exchange. Furthermore, the anion exchange behaviors can be fine-tuned by the structural characteristics of the LA spacer and A-site cations. The findings from our systematic exploration of anion exchange in RPPs enabled the preparation of high-quality lateral heterostructures of $n = 2$ RPPs that are more stable against anion interdiffusion and degradation than similar interfaces in 3D perovskites and suitable for the operating environments of many optoelectronic devices. This study provides new insights on the complex, anisotropic halide diffusion behaviors of RPPs and demonstrates the capacity of anion exchange as a general post-synthetic modification technique to prepare stable lateral heterostructures from existing RPP starting materials to enable their future optoelectronic device applications.

3.8. References

(1) Stranks, S. D.; Snaith, H. J. Metal-Halide Perovskites for Photovoltaic and Light-Emitting Devices. *Nature Nanotechnology* **2015**, *10* (5), 391–402.

(2) Zhu, H.; Fu, Y.; Meng, F.; Wu, X.; Gong, Z.; Ding, Q.; Gustafsson, M. V.; Trinh, M. T.; Jin, S.; Zhu, X.-Y. Lead Halide Perovskite Nanowire Lasers with Low Lasing Thresholds and High Quality Factors. *Nature Materials* **2015**, *14* (6), 636–642.

(3) Fu, Y.; Zhu, H.; Chen, J.; Hautzinger, M. P.; Zhu, X.-Y.; Jin, S. Metal Halide Perovskite Nanostructures for Optoelectronic Applications and the Study of Physical Properties. *Nature Reviews Materials* **2019**, *4* (3), 169–188.

(4) Yin, W.-J.; Shi, T.; Yan, Y. Unusual Defect Physics in $CH_3NH_3PbI_3$ Perovskite Solar Cell Absorber. *Appl. Phys. Lett.* **2014**, *104* (6), 063903.

(5) Manser, J. S.; Christians, J. A.; Kamat, P. V. Intriguing Optoelectronic Properties of Metal Halide Perovskites. *Chem. Rev.* **2016**, *116* (21), 12956–13008.

(6) Protesescu, L.; Yakunin, S.; Bodnarchuk, M. I.; Krieg, F.; Caputo, R.; Hendon, C. H.; Yang, R. X.; Walsh, A.; Kovalenko, M. V. Nanocrystals of Cesium Lead Halide Perovskites ($CsPbX_3$, X = Cl, Br, and I): Novel Optoelectronic Materials Showing Bright Emission with Wide Color Gamut. *Nano Lett.* **2015**, *15* (6), 3692–3696.

(7) Alferov, Zh. I. The History and Future of Semiconductor Heterostructures. *Semiconductors* **1998**, *32* (1), 1–14.

(8) Dou, L.; Lai, M.; Kley, C. S.; Yang, Y.; Bischak, C. G.; Zhang, D.; Eaton, S. W.; Ginsberg, N. S.; Yang, P. Spatially Resolved Multicolor $CsPbX_3$ Nanowire Heterojunctions via Anion Exchange. *Proc Natl Acad Sci USA* **2017**, *114* (28), 7216.

(9) Pan, D.; Fu, Y.; Chen, J.; Czech, K. J.; Wright, J. C.; Jin, S. Visualization and Studies of Ion-Diffusion Kinetics in Cesium Lead Bromide Perovskite Nanowires. *Nano Lett.* **2018**, *18* (3), 1807–1813.

(10) Scheidt, R. A.; Kamat, P. V. Temperature-Driven Anion Migration in Gradient Halide Perovskites. *J. Chem. Phys.* **2019**, *151* (13), 134703.

(11) Hoke, E. T.; Slotcavage, D. J.; Dohner, E. R.; Bowring, A. R.; Karunadasa, H. I.; McGehee, M. D. Reversible Photo-Induced Trap Formation in Mixed-Halide Hybrid Perovskites for Photovoltaics. *Chem. Sci.* **2015**, *6* (1), 613–617.

(12) Draguta, S.; Sharia, O.; Yoon, S. J.; Brennan, M. C.; Morozov, Y. V.; Manser, J. S.; Kamat, P. V.; Schneider, W. F.; Kuno, M. Rationalizing the Light-Induced Phase Separation of Mixed Halide Organic–Inorganic Perovskites. *Nature Communications* **2017**, *8* (1), 200.

(13) Bischak, C. G.; Hetherington, C. L.; Wu, H.; Aloni, S.; Ogletree, D. F.; Limmer, D. T.; Ginsberg, N. S. Origin of Reversible Photoinduced Phase Separation in Hybrid Perovskites. *Nano Lett.* **2017**, *17* (2), 1028–1033.

(14) Wang, Y.; Chen, Z.; Deschler, F.; Sun, X.; Lu, T.-M.; Wertz, E. A.; Hu, J.-M.; Shi, J. Epitaxial Halide Perovskite Lateral Double Heterostructure. *ACS Nano* **2017**, *11* (3), 3355–3364.

(15) Blancon, J.-C.; Even, J.; Stoumpos, Costas. C.; Kanatzidis, Mercouri. G.; Mohite, A. D. Semiconductor Physics of Organic–Inorganic 2D Halide Perovskites. *Nature Nanotechnology* **2020**, *15* (12), 969–985.

(16) Smith, I. C.; Hoke, E. T.; Solis-Ibarra, D.; McGehee, M. D.; Karunadasa, H. I. A Layered Hybrid Perovskite Solar-Cell Absorber with Enhanced Moisture Stability. *Angewandte Chemie International Edition* **2014**, *53* (42), 11232–11235.

(17) Spitha, N.; Kohler, D. D.; Hautzinger, M. P.; Li, J.; Jin, S.; Wright, J. C. Discerning between Exciton and Free-Carrier Behaviors in Ruddlesden–Popper Perovskite Quantum Wells through Kinetic Modeling of Photoluminescence Dynamics. *J. Phys. Chem. C* **2020**, *124* (31), 17430–17439.

(18) Katan, C.; Mercier, N.; Even, J. Quantum and Dielectric Confinement Effects in Lower-Dimensional Hybrid Perovskite Semiconductors. *Chem. Rev.* **2019**, *119* (5), 3140–3192.

(19) Saparov, B.; Mitzi, D. B. Organic–Inorganic Perovskites: Structural Versatility for Functional Materials Design. *Chem. Rev.* **2016**, *116* (7), 4558–4596.

(20) Gao, Y.; Shi, E.; Deng, S.; Shiring, S. B.; Snaider, J. M.; Liang, C.; Yuan, B.; Song, R.; Janke, S. M.; Liebman-Peláez, A.; Yoo, P.; Zeller, M.; Boudouris, B. W.; Liao, P.; Zhu, C.; Blum, V.; Yu, Y.; Savoie, B. M.; Huang, L.; Dou, L. Molecular Engineering of Organic–Inorganic Hybrid Perovskites Quantum Wells. *Nature Chemistry* **2019**, *11* (12), 1151–1157.

(21) Fu, Y.; Hautzinger, M. P.; Luo, Z.; Wang, F.; Pan, D.; Aristov, M. M.; Guzei, I. A.; Pan, A.; Zhu, X.; Jin, S. Incorporating Large A Cations into Lead Iodide Perovskite Cages: Relaxed Goldschmidt Tolerance Factor and Impact on Exciton–Phonon Interaction. *ACS Cent. Sci.* **2019**, *5* (8), 1377–1386.

(22) Hautzinger, M. P.; Pan, D.; Pigg, A. K.; Fu, Y.; Morrow, D. J.; Leng, M.; Kuo, M.-Y.; Spitha, N.; Lafayette, D. P.; Kohler, D. D.; Wright, J. C.; Jin, S. Band Edge Tuning of Two-Dimensional Ruddlesden–Popper Perovskites by A Cation Size Revealed through Nanoplates. *ACS Energy Lett.* **2020**, *5* (5), 1430–1437.

(23) Tsai, H.; Nie, W.; Blancon, J.-C.; Stoumpos, C. C.; Asadpour, R.; Harutyunyan, B.; Neukirch, A. J.; Verduzco, R.; Crochet, J. J.; Tretiak, S.; Pedesseau, L.; Even, J.; Alam, M. A.; Gupta, G.; Lou, J.; Ajayan, P. M.; Bedzyk, M. J.; Kanatzidis, M. G.; Mohite, A. D. High-Efficiency Two-Dimensional Ruddlesden–Popper Perovskite Solar Cells. *Nature* **2016**, *536* (7616), 312–316.

(24) Yuan, M.; Quan, L. N.; Comin, R.; Walters, G.; Sabatini, R.; Voznyy, O.; Hoogland, S.; Zhao, Y.; Beauregard, E. M.; Kanjanaboos, P.; Lu, Z.; Kim, D. H.; Sargent, E. H. Perovskite Energy Funnels for Efficient Light-Emitting Diodes. *Nature Nanotechnology* **2016**, *11* (10), 872–877.

(25) Liang, D.; Peng, Y.; Fu, Y.; Shearer, M. J.; Zhang, J.; Zhai, J.; Zhang, Y.; Hamers, R. J.; Andrew, T. L.; Jin, S. Color-Pure Violet-Light-Emitting Diodes Based on Layered Lead Halide Perovskite Nanoplates. *ACS Nano* **2016**, *10* (7), 6897–6904.

(26) Zhang, F.; Lu, H.; Tong, J.; Berry, J. J.; Beard, M. C.; Zhu, K. Advances in Two-Dimensional Organic–Inorganic Hybrid Perovskites. *Energy Environ. Sci.* **2020**, *13* (4), 1154–1186.

(27) Liu, Y.; Ye, H.; Zhang, Y.; Zhao, K.; Yang, Z.; Yuan, Y.; Wu, H.; Zhao, G.; Yang, Z.; Tang, J.; Xu, Z.; Liu, S. (Frank). Surface-Tension-Controlled Crystallization for High-Quality 2D Perovskite Single Crystals for Ultrahigh Photodetection. *Matter* **2019**, *1* (2), 465–480.

(28) Lin, Y.; Bai, Y.; Fang, Y.; Wang, Q.; Deng, Y.; Huang, J. Suppressed Ion Migration in Low-Dimensional Perovskites. *ACS Energy Lett.* **2017**, *2* (7), 1571–1572.

(29) Xiao, X.; Dai, J.; Fang, Y.; Zhao, J.; Zheng, X.; Tang, S.; Rudd, P. N.; Zeng, X. C.; Huang, J. Suppressed Ion Migration along the In-Plane Direction in Layered Perovskites. *ACS Energy Lett.* **2018**, *3* (3), 684–688.

(30) Huang, Z.; Proppe, A. H.; Tan, H.; Saidaminov, M. I.; Tan, F.; Mei, A.; Tan, C.-S.; Wei, M.; Hou, Y.; Han, H.; Kelley, S. O.; Sargent, E. H. Suppressed Ion Migration in Reduced-Dimensional Perovskites Improves Operating Stability. *ACS Energy Lett.* **2019**, *4* (7), 1521–1527.

(31) Cho, J.; DuBose, J. T.; Le, A. N. T.; Kamat, P. V. Suppressed Halide Ion Migration in 2D Lead Halide Perovskites. *ACS Materials Lett.* **2020**, *2* (6), 565–570.

(32) Akriti; Shi, E.; Shiring, S. B.; Yang, J.; Atencio-Martinez, C. L.; Yuan, B.; Hu, X.; Gao, Y.; Finkenauer, B. P.; Pistone, A. J.; Yu, Y.; Liao, P.; Savoie, B. M.; Dou, L. Layer-by-Layer Anionic Diffusion in Two-Dimensional Halide Perovskite Vertical Heterostructures. *Nature Nanotechnology* **2021**.

(33) Pan, D.; Fu, Y.; Spitha, N.; Zhao, Y.; Roy, C. R.; Morrow, D. J.; Kohler, D. D.; Wright, J. C.; Jin, S. Deterministic Fabrication of Arbitrary Vertical Heterostructures of Two-Dimensional Ruddlesden–Popper Halide Perovskites. *Nature Nanotechnology* **2020**.

(34) Fu, Y.; Zheng, W.; Wang, X.; Hautzinger, M. P.; Pan, D.; Dang, L.; Wright, J. C.; Pan, A.; Jin, S. Multicolor Heterostructures of Two-Dimensional Layered Halide Perovskites That Show Interlayer Energy Transfer. *J. Am. Chem. Soc.* **2018**, *140* (46), 15675–15683.

(35) Shi, E.; Yuan, B.; Shiring, S. B.; Gao, Y.; Akriti; Guo, Y.; Su, C.; Lai, M.; Yang, P.; Kong, J.; Savoie, B. M.; Yu, Y.; Dou, L. Two-Dimensional Halide Perovskite Lateral Epitaxial Heterostructures. *Nature* **2020**, *580* (7805), 614–620.

(36) Oswald, I. W. H.; Koegel, A. A.; Neilson, J. R. General Synthesis Principles for Ruddlesden–Popper Hybrid Perovskite Halides from a Dynamic Equilibrium. *Chem. Mater.* **2018**, *30* (23), 8606–8614.

(37) Solis-Ibarra, D.; Smith, I. C.; Karunadasa, H. I. Post-Synthetic Halide Conversion and Selective Halogen Capture in Hybrid Perovskites. *Chem. Sci.* **2015**, *6* (7), 4054–4059.

(38) Elmelund, T.; Scheidt, R. A.; Seger, B.; Kamat, P. V. Bidirectional Halide Ion Exchange in Paired Lead Halide Perovskite Films with Thermal Activation. *ACS Energy Lett.* **2019**, *4* (8), 1961–1969.

(39) Zhang, Y.; Lu, D.; Gao, M.; Lai, M.; Lin, J.; Lei, T.; Lin, Z.; Quan, L. N.; Yang, P. Quantitative Imaging of Anion Exchange Kinetics in Halide Perovskites. *Proc Natl Acad Sci USA* **2019**, *116* (26), 12648.

(40) Osherov, A.; Feldman, Y.; Kaplan-Ashiri, I.; Cahen, D.; Hodes, G. Halide Diffusion in MAPbX3: Limits to Topotaxy for Halide Exchange in Perovskites. *Chem. Mater.* **2020**, *32* (10), 4223–4231.

(41) Stoumpos, C. C.; Cao, D. H.; Clark, D. J.; Young, J.; Rondinelli, J. M.; Jang, J. I.; Hupp, J. T.; Kanatzidis, M. G. Ruddlesden–Popper Hybrid Lead Iodide Perovskite 2D Homologous Semiconductors. *Chem. Mater.* **2016**, *28* (8), 2852–2867.

(42) Ma, D.; Fu, Y.; Dang, L.; Zhai, J.; Guzei, I. A.; Jin, S. Single-Crystal Microplates of Two-Dimensional Organic–Inorganic Lead Halide Layered Perovskites for Optoelectronics. *Nano Research* **2017**, *10* (6), 2117–2129.

(43) Shi, E.; Deng, S.; Yuan, B.; Gao, Y.; Akriti; Yuan, L.; Davis, C. S.; Zemlyanov, D.; Yu, Y.; Huang, L.; Dou, L. Extrinsic and Dynamic Edge States of Two-Dimensional Lead Halide Perovskites. *ACS Nano* **2019**, *13* (2), 1635–1644.

(44) Senocrate, A.; Maier, J. Solid-State Ionics of Hybrid Halide Perovskites. *J. Am. Chem. Soc.* **2019**, *141* (21), 8382–8396.

(45) Li, L.; Shang, X.; Wang, S.; Dong, N.; Ji, C.; Chen, X.; Zhao, S.; Wang, J.; Sun, Z.; Hong, M.; Luo, J. Bilayered Hybrid Perovskite Ferroelectric with Giant Two-Photon Absorption. *J. Am. Chem. Soc.* **2018**, *140* (22), 6806–6809.

Chapter 4 . Cation Diffusion and Chemical Restructuring in Atomically Precise 2D/3D Lead Halide Perovskite Heterojunctions [a]

4.1. Introduction

Lead halide perovskite (LHP) solar cells have advanced to the current frontier of single-junction photovoltaic efficiency in under ¼ the time it took silicon,[1–3] yet their commercial viability is still hampered by a lack of long-term stability.[4] Efforts to stabilize LHP solar cells have largely been turned toward addressing the thermodynamic stability of the perovskite absorber and its interfaces with charge carrier transport layers (CTLs) on either side of the device. Within the LHP absorber, which typically consists of a polycrystalline thin film of a three-dimensional (3D) perovskite $APbX_3$ (A = methylammonium (MA), formamidinium (FA), and Cs; X = I, Br, and Cl), synthetic improvements yielding higher crystallinity and more stable compositions have drastically improved the performance and lifetimes of LHP solar cells due to the passivation and removal of defects within the film.[5–9] Simultaneous approaches to minimize defects at perovskite/CTL interfaces have ranged from molecular surface treatments to elimination of the CTL altogether in favor of band edge tuning through surface modification,[10,11] but the broad scope of device configurations and CTL materials makes the stabilization of LHP/CTL interfaces a much more nuanced challenge.

Among the many approaches to passivate LHP surfaces and interfaces, incorporation of a thin layer of two-dimensional (2D) or quasi-2D LHPs on the surface of the 3D LHP film to form a planar 2D/3D LHP heterostructure (HS) has been an effective strategy.[12] 2D and quasi-2D LHPs

[a] This chapter is also in preparation for publication as an article in collaboration with Kristel Forlano, Ping Chen, Zihua Zhu, John C. Wright, and Song Jin.

are layered analogues of their 3D LHP counterpart, whose bulk structure consists of planar perovskite slabs $[A_{n-1}Pb_nX_{3n+1}]^{2-}$ *n* octahedral layers thick separated by layers of organic "spacer" cations (LA). The spacer can be bilayers of large monoammonium cations (e.g. *n*-butylammonium (BA) or phenethylammonium (PEA)), which form Ruddlesden–Popper perovskites (RPPs) of formula $(LA)_2(A)_{n-1}Pb_nX_{3n+1}$, or monolayers of large dications (e.g. 3-(aminomethyl)piperidinium (3-AMP) or 1,4-butanediammonium (BDA)), which form Dion–Jacobson (DJ) perovskites of formula $(LA)(A)_{n-1}Pb_nX_{3n+1}$. For brevity, we refer to these 2D LHP phases using the syntax *n* = i LA-A. 2D and quasi-2D LHPs (RPPs in particular) have been integrated onto 3D LHP absorbers to passivate the 3D LHP surface and improve longevity. The large organic cations in the 2D structure provide enhanced resistance to environmental degradation and act as a barrier to migrating ions – a major mechanism driving LHP degradation.[13–15] Alongside this, they retain many of the desirable optoelectronic properties of their 3D counterparts (defect tolerance, long carrier lifetimes, long carrier diffusion distances),[16] leading to simultaneous improvements in stability *and* performance.[17,18] In recent years, a substantial fraction of the most efficient and stable LHP solar cells have incorporated 2D/3D interfaces at the absorber surface and/or the grain boundaries within the LHP film.[12,19]

Despite their success, the controlled fabrication of 2D/3D HSs is challenging due to poor control over phase dispersity of the 2D overlayer. The layer thickness *n* of 2D RPPs is highly sensitive to the relative activity of precursor ions during growth,[20–22] thus polydisperse 2D overlayers tend to form from the inhomogeneous precursor matrix present during common wet fabrication methods such as spin coating.[23] High phase dispersity is undesirable because it leads to inhomogeneities in the energy landscape at the absorber/CTL interface that can impede charge carrier extraction.[24,25] Efforts to address this have included tuning of 2D precursor activity to favor

a narrower range of phases,[19] engineering spacer cations to achieve RPP phase systems with lower dispersity,[26] and pre-synthesizing the desired 2D LHP before integrating it onto the 3D surface in a secondary step.[27,28] But even if a phase-pure 2D/3D HS is successfully fabricated, 2D/3D interfaces undergo restructuring into a distribution of quasi-2D phases due to ionic diffusion.[29–34] Most investigations of this ionic diffusion have studied n = 1-2 RPP|$MAPbI_3$ HSs and focused on spacer cations, which influence ion diffusion kinetics. However, the exact nature of restructuring at the 2D/3D interface is muddled by the heterogeneous chemical landscape of the thin films being studied, and the scope of 2D overlayers studied is severely limited by challenges in synthesizing phase-pure 2D overlayers – especially for $n > 2$ RPPs.

In this work, we leverage synthesis methods developed in fundamental studies of 3D and 2D LHPs to independently grow large-area single crystals of 3D and 2D LHPs, then merge them using van der Waals heterostructure fabrication employed in studies of 2D materials.[35–38] The resulting atomically precise 2D/3D HSs are the highest quality 2D/3D LHP interfaces prepared to-date. Investigation of 2D/3D interfaces via spatially registered photoluminescence (PL) microscopy, atomic force microscopy (AFM), and time-of-flight secondary ion mass spectrometry (ToF-SIMS) reveal a much more precise picture of diffusion and restructuring at the 2D/3D interface, and the exploration of new classes of 2D overlayers using powder X-ray diffraction (XRD) and microscopy techniques unveil a road to classes of 2D/3D interfaces that may be much more stable than ones studied previously.

4.2. Fabrication of Atomically-Precise 2D/3D Halide Perovskite Heterojunctions

To prepare a wide scope of 2D/3D HSs with precision, we synthesized high-quality 2D & 3D LHPs separately and interfaced them using mechanical vdW assembly (Figure 4.1a). Large-area single crystals (SCs) of 3D LHPs were grown via the popular inverse temperature

crystallization method,[35] using γ-butyrolactone (GBL) precursor solution confined between two planar substrates to template the growth of smooth SC plates with large width-to-thickness ratios (>500 μm : >20 μm, see Figure A3.2 for examples). We silanized our preferred substrates (glass and p-type Si/native oxide) to functionalize them with hydrophobic surfaces that promote the migration of precursor ions and growth of larger SCs (Figure A3.3).[39,40] Following SC growth, we washed the 3D SCs with MeCN to prevent degradation of the 3D LHP surface by residual precursor solution. MeCN only sparingly dissolves the 3D surface,[28] but we still observed MeCN-etched striations aligned parallel to the edge facets of the 3D SCs after only a few seconds of exposure (Figure A3.4). We posit this etching could be utilized to reduce the reflectance of highly crystalline perovskite absorber surfaces analogous to textured c-Si absorbers.[41] For the 2D RPP overlayers, phase-pure, highly crystalline microsheets of a wide variety of RPPs (10-500 μm wide, 5-500 nm thick, see Figure A3.1 for examples) were synthesized via floating growth at the surface of an aqueous droplet of LHP precursor solution following our previously reported procedure (see methods in Appendix 3).[42] We retrieved the intact microsheets by contacting them with hydrophobic polydimethylsiloxane (PDMS) film, then fabricated the 2D/3D HS by stamping the RPP-covered PDMS onto an aligned 3D LHP crystal (see methods for detailed notes on this approach).[42,43]

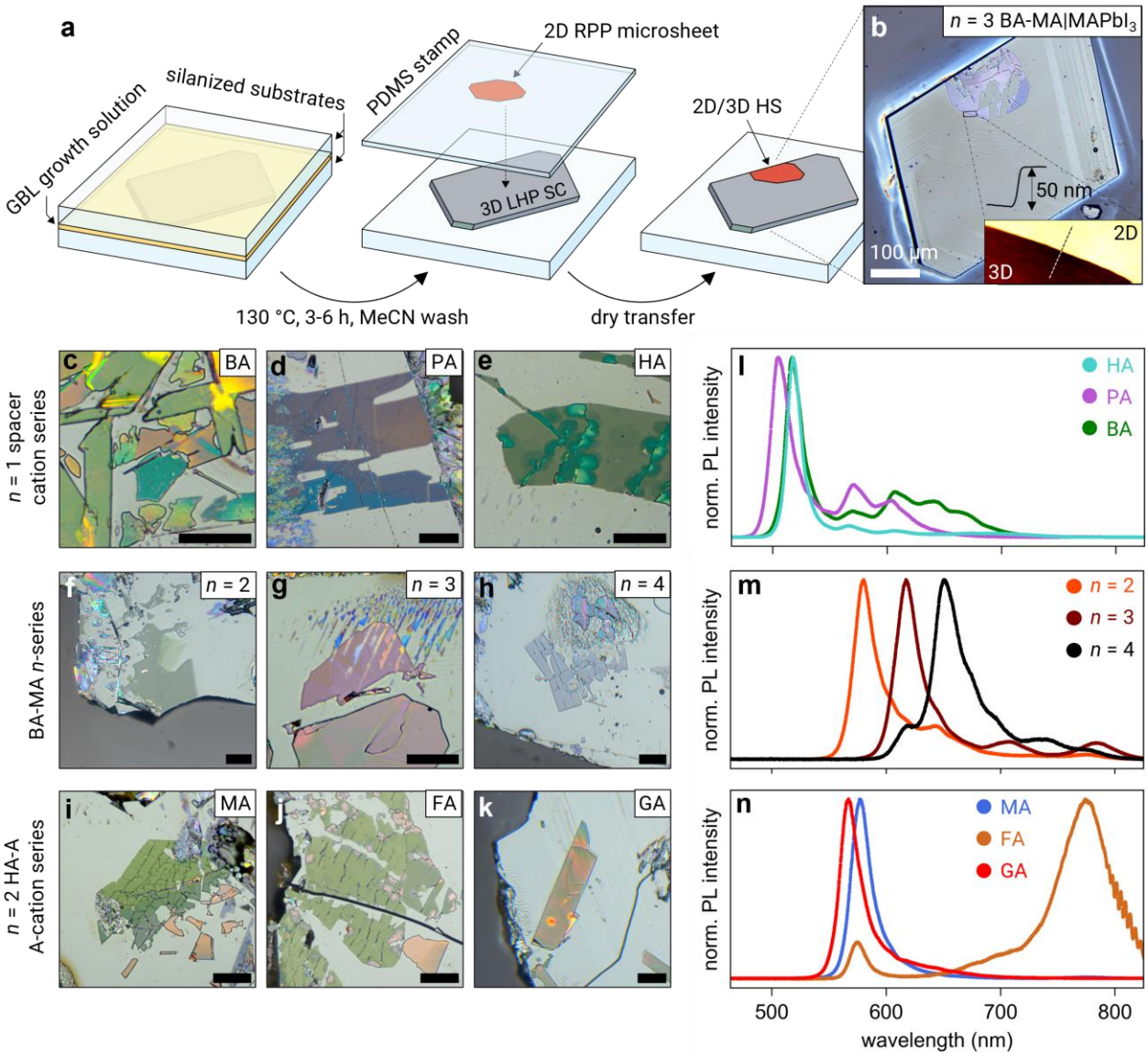

Figure 4.1. Fabrication of atomically precise 2D/3D halide perovskite heterojunctions. **(a)** Fabrication sequence starts with growth of flat 3D $MAPbI_3$ single crystals via confined inverse temperature crystallization, followed by dry transfer of 2D RPP microsheets. **(b)** Optical microscope image of a n = 3 BA-MA|(MA)PbI_3 HS fabricated according to the scheme in (a) with corresponding AFM topography of a 2D step edge (false color inset). **(c-k)** Optical microscope images of 2D|$MAPbI_3$ HSs with various phase-pure 2D RPP overlayers: n = 1 2D LHPs **(c-e)** containing n-butylammonium (BA) **(c)**, n-pentylammonium (PA) **(d)**, and n-hexylammonium

(HA) **(e)** spacer cations; a homologous *n*-series **(f-h)** of $(BA)_2(MA)_{n-1}Pb_nI_{3n+1}$ from $n = 2$ **(f)** to $n = 4$ **(h)**; $n = 2$ HA-A RPPs with various A-site cations **(i-k)** including methylammonium (MA) **(i)**, formamidinium (FA) **(j)**, and guanidinium (GA) **(k)**. **(l-n)** PL spectra of the HSs shown in (c-e) **(l)**, (f-h) **(m)**, and (i-k) **(n)**.

The resulting 2D/3D LHP heterojunctions are assembled deterministically and are atomically precise due to the high crystallinity of each component prior to assembly. Thus, their morphologies closely resemble the platonic ideal of those in 2D-passivated 3D perovskite solar absorbers. Figure 4.1b shows a typical 3D SC ($MAPbI_3$) and 2D RPP overlayer ($n = 3$ BA-MA) prepared via this method. Correlated AFM topography (Figure 4.1b, inset) shows the 2D overlayer is 50 nm thick – within the thickness regime of 2D passivating layers used in high performance solar cells. The 2D overlayer thickness can be controlled through the growth time of the 2D microsheets. The surface quality of each HS component is apparent through the specular appearance of the 3D and 2D surfaces, as well as their RMS roughness (via AFM), which is on the order of single nm for each layer (Figure A3.5). The consistent quasi-hexagonal shapes of the $MAPbI_3$ plates presented this work have been identified as the (100) facet in previous works on $MAPbI_3$ SCs,[44] and we are confident the lamellar growth habit of the 2D perovskites indicates that the surfaces of 2D sheets are (001) (out-of-plane) facets. The resulting $(100)_{3D}|(001)_{2D}$ interfaces reflect the typical "horizontal" interfacial alignment observed in 2D/3D HSs prepared via most wet methods.[45,46]

Alongside interface quality, decoupling material synthesis and HS assembly allows phase-pure 2D overlayers to be fabricated with confidence. Whereas integration of 2D overlayers during solar cell fabrication typically uses solvents and temperatures that restructure the 2D/3D interface, room temperature mechanical assembly presents phase-pure systems to investigate the intrinsic

thermodynamic stability and subsequent phase restructuring of 2D/3D LHP interfaces as diffusion couples. Mechanical assembly also expands the variety of 2D overlayers that can be interfaced with the 3D absorber. Figure 4.1c-k shows a collage of most of the 2D RPP overlayers used in this work, with different spacer cations (Figure 4.2c-e), perovskite layer thicknesses (Figure 4.1f-h), and A-site cations (Figure 4.1i-k). The corresponding PL spectra of the HSs shown are in Figure 4.1l-n. Strong emission from singular peaks attest to the phase purity of the 2D RPP overlayers, although in many of the spectra there is already emission from multiple phases beyond (higher in *n*) the intended RPP overlayer. These impurities arise from interdiffusion at the 2D/3D interface after dry assembly, regardless of the 2D RPP overlayer chosen and even in absence of heat or light.

4.3. Mechanism of Restructuring at 2D/3D LHP Interface

To better understand the phase restructuring at the 2D/3D HS interface, we leveraged the precise thickness control attainable through floating growth of 2D RPP microsheets. The restructuring is most apparent under accelerated ageing conditions such as ISOS-D-2I (65°C, inert atmosphere, dark).[47] Figure 4.2a shows a comparison of PL spectra from a microscopic excitation spot on a $n = 2$ HA-MA|$MAPbI_3$ HS freshly after fabrication and after 12 h of accelerated ageing. Several emission peaks emerge between the original $n = 2$ emission at 575 nm and the 3D emission at 775 nm. The peaks within the broad feature (675 nm, 690 nm, 705 nm) closely match reported emission wavelengths for $n = 5$-7 RPP phases containing the similar spacer cation BA.[20,48,49] This transformation suggests that an originally sharp $n = 2$|3D interface was transformed into an array of higher-*n* intermediate RPP phases. We sought to narrow the exact morphology of this interfacial reaction and the extent to which it propagates.

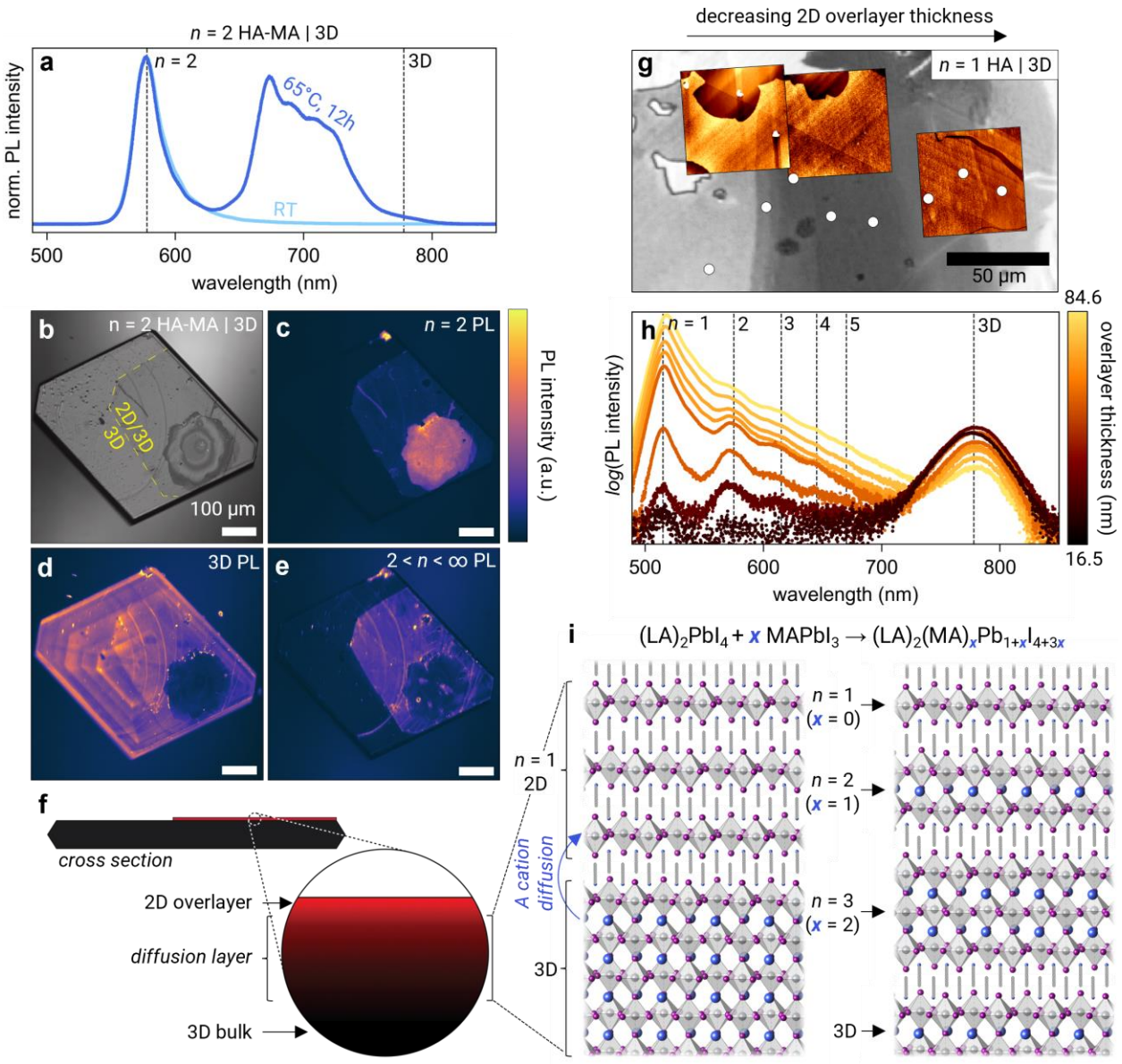

Figure 4.2. Nature of interdiffusion and restructuring at 2D/3D perovskite interfaces. **(a)** PL spectra of a n = 2 HA-MA|$MAPbI_3$ HS before and after accelerated diffusion for 12 h at 65°C. **(b-e)** Widefield spectral imaging of a n = 2 HA-MA|$MAPbI_3$ HS with varying 2D thickness after 1 d ambient ageing: **(b)** bright field optical, **(c)** n = 2 RPP PL (580±10 nm), **(d)** 3D PL (750+ nm), **(e)** n > 2 2D PL (650-700 nm). **(f)** Scheme depicting extent of 2D/3D diffusion inferred from the data in (a-e). **(g)** Bright field optical image of a thin n = 1 HA|$MAPbI_3$ HS with terraced 2D morphology.

Inset false-color images are registered AFM topography. White dots are PL measurement points for (h). **(h)** PL spectra of the points indicated in (g) after accelerated diffusion for 36 h at 65°C. **(i)** Scheme depicting atomic-scale nature of the 2D/3D diffusion zone inferred from the data in (g,h).

To probe the extent of the interfacial phase change, we analyzed another n = 2 HA-MA|$MAPbI_3$ HS after only 1d ambient ageing using widefield PL microscopy (Figure 4.2b-e). The n = 2 overlayer consists of a large-area, thin sheet (likely under 20 nm based on the opacity of similar HSs measured via AFM; see Figure A3.1) together with a thicker, terraced island of n = 2 RPP, which appears as a bullseye in the optical image (Figure 4.2b) due to etaloning effects. Imaging PL in the emission range of the n = 2 RPP peak (570-590 nm) shows positive contrast in the 2D overlayer region that correlates with 2D overlayer thickness (Figure 4.2c). This correlation occurs in this narrow thickness regime because an increasing proportion of the excitation light is absorbed by the thicker 2D overlayer.

In contrast, the PL intensity for 3D perovskite is inversely proportional to the thickness of the 2D layer, as seen by the dark region underneath the thicker island of n = 2 HA-MA in Figure 4.2d. This negative contrast is due to attenuation of incident excitation light by the 2D overlayer. We further verified this attenuation effect by collecting photoluminescence excitation (PLE) spectra from various BA-MA|$MAPbI_3$ HSs with different n RPP overlayers, which revealed that the relative 3D emission intensities closely correspond to the transmittance of the 2D overlayer at each wavelength (Figure A3.6). Despite this attenuation effect, there is positive contrast in 3D emission where the overlayer is extremely thin. We believe this is due to an improvement in 3D PL quantum yield due to 2D surface passivation,[50] which could outweigh the loss of incident excitation light when the overlayer is sufficiently thin (<20 nm).

We used this contrast difference as a mechanism to interrogate the locale of the restructured phases at the 2D/3D interface, which have distinct emission wavelengths between the original 2D and 3D perovskite emission wavelengths (Figure 4.2a). A PL image of the restructured 2D phases in the 650-700 nm wavelength range (Figure 4.2e) shows contrast anticorrelated to 2D thickness analogous to the 3D perovskite emission, verifying that the 2D/3D restructuring is localized at the 2D/3D interface. The lower emission intensity in the thickest overlayer region also indicates that the restructuring is likely confined within the top few nm of the 3D perovskite surface, meaning only a few layers are reformed at a time. This implies that there is a narrow "diffusion zone" at the 2D/3D interface where even phase-pure 2D overlayers undergo discrete transformations into RPP phases of increasing n over time (Figure 4.2f).

To accurately understand this diffusion zone on the atomic scale, we subjected an $n = 1$ HA|$MAPbI_3$ HS to extensive accelerated ageing (36 h at 65°C) and employed registered optical, PL, and atomic force microscope data to directly connect 2D overlayer thickness with phase distribution after restructuring (Figure 4.2g,h). The layer-by-layer growth of the $n = 1$ HA phase yields thin sheets with gradually changing thickness and large-area steps, presenting a variety of overlayer thicknesses in an otherwise identical HS. Additionally, the pure $n = 1$ 2D composition ensures that all $n > 1$ RPP phases must have originated from A-site cations diffusing from the underlying 3D perovskite crystal. The optical image and registered AFM topography (inset false color images) in Figure 4.2g indicate steps ranging in thickness from 16.5 nm (~10 perovskite layers) to 84.6 nm (~52 perovskite layers, see Figure A3.7 and Table A3.3 for exact measurements and step heights). The PL spectra as a function of overlayer thickness (Figure 4.2h, measured at locations marked in Figure 4.2g) show an increase in $n > 1$ PL intensity as a function of decreasing overlayer thickness, reinforcing the localized diffusion zone inferred from the widefield PL

imaging experiment. As the 2D overlayer thickness decreases, even higher n RPP phases become apparent in the spectra (up to $n = 5$ is distinguishable). This cascade of increasing n peaks suggests that the 2D/3D interface undergoes a series of discrete phase transformations, incrementing an original 2D overlayer of layer thickness n to a discrete cascade of (n+1, n+2, …) phases as diffusion continues. Figure 4.2i illustrates the atomic-scale structure of the 2D/3D interface pre- and post-diffusion as inferred from the data in Figure 4.2g,h. Each step in the 2D/3D transformation is topotactic, occurring in discrete $APbI_3$ steps according to the reaction $(LA)_2(A)_{n-1}Pb_nI_{3n+1} + x\ APbI_3 \rightarrow (LA)_2(A)_{n+x-1}Pb_{n+x}I_{3(n+x)+1}$. Importantly, this transformation increases the effective thickness of the 2D overlayer as $APbI_3$ units are added to the 2D RPP slabs through the A-cation diffusion process. In the example above, a minimum of 4 n = 1 layers must have transformed into n = 2,3,4,5 to yield the PL spectra observed in Figure 4.2h (10 $[PbI_6]^{4-}$ octahedral units added in total), corresponding to a 2D overlayer thickness increase of at least 6 nm. This reconstruction spells consequences for device performance because the efficiency of carrier extraction (current density) is highly sensitive to the thickness and band alignment of 2D passivating layers.[28,51]

We then sought to evaluate the scope of 2D RPP phases that are susceptible to interdiffusion reactions under ambient conditions beginning with a series of n = 1 2D perovskites with the common spacer cations BA, PA, HA, and PEA (Figure 4.3a-d). For this study, all 2D/3D HSs were stored at room temperature in an environmental chamber under dry N_2 during and between measurements (see methods in Appendix 3).

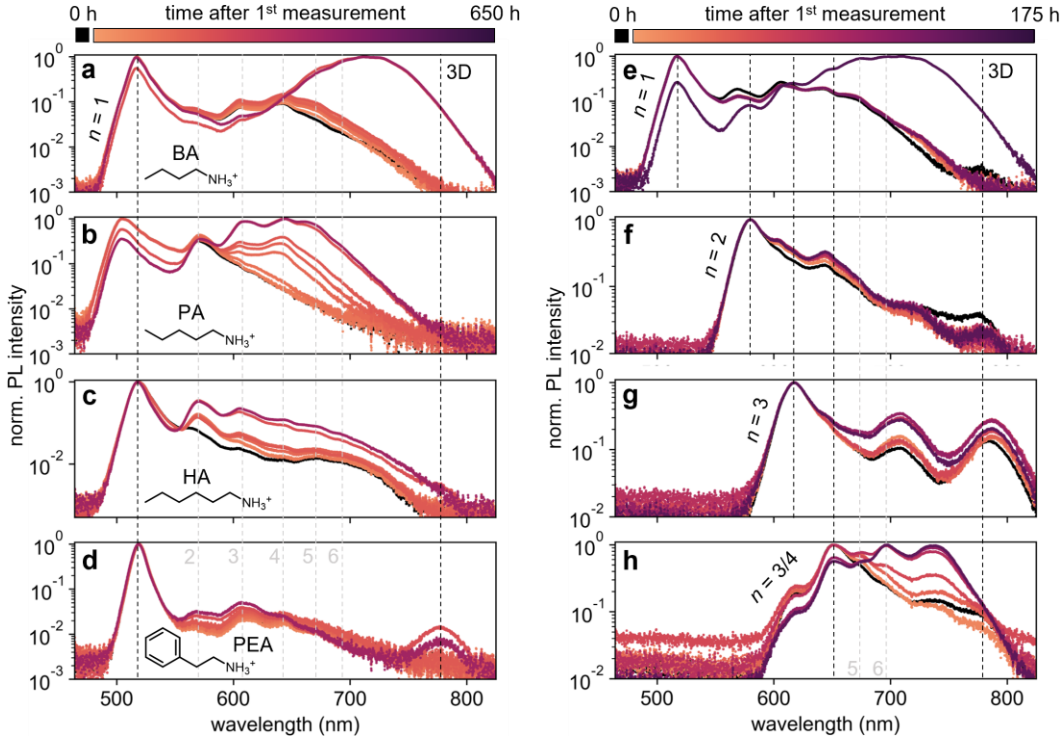

Figure 4.3. Ubiquity of A-cation diffusion from 3D perovskite across most 2D RPP overlayers. **(a-d)** Comparison of 2D/3D interdiffusion over time under ambient conditions for n = 1 2D perovskites with different spacer cations: $(BA)_2PbI_4$ **(a)**, $(PA)_2PbI_4$ **(b)**, $(HA)_2PbI_4$ **(c)**, $(PEA)_2PbI_4$ **(d)**. **(e-h)** 2D/3D interdiffusion as a function of RPP n phase: n = 1 BA **(e)**, n = 2 BA-MA **(f)**, n = 3 BA-MA **(g)**, n = 3/4 BA-MA **(h)**.

The evolution of PL spectra over time from single microscopic spots on mechanically assembled n = 1 LA|$MAPbI_3$ HSs (Figure 4.3a-d, see Figure A3.8 for images of the HSs) show interdiffusion across 2D/3D HSs occurs at relatively short time scales (<24 h) even under ambient, dark conditions for 2D perovskites containing the most common spacer cations. It appears that the rate of interdiffusion is slower for PEA|3D interfaces compared to the aliphatic (LA = BA, PA, HA) spacers, but exact kinetics cannot be resolved from our experimental parameters due to possible influences from other variables. Despite this, the diffusion outcomes observed in Figure

4.3 are reproducible on similar timescales for each n = 1 LA|$MAPbI_3$ HS (Figure A3.9), and uncontrolled variables in this experiment (nanoscale 3D surface morphology, twist angle between the 2D and 3D lattice) do not have any clearly observed effects on the diffusion kinetics (Table A3.4). With extensive 2D/3D interdiffusion occurring over the course of mere days even at ambient conditions for each HS system in this study, long-term stabilization of 2D/3D interfaces by tuning spacer cations alone does not seem promising.

It should be noted that the most significant difference among different spacer cations is arguably not the relative kinetics of A-cation interdiffusion, but rather the relative phase distributions of the restructured RPP phases. Close inspection of the PL spectra of n = 1 LA|$MAPbI_3$ HSs with aliphatic spacer cations each show an evolving cascade of n phases as interdiffusion proceeds over time, but the extent of resolvable RPP phases spans further for BA and HA phases vs. PA. Furthermore, BA and PEA-based 2D overlayers seem to preferentially restructure into $n \geq 3$ RPP phases, partially "skipping" the n = 2 phase in the process. These non-monotonic restructuring sequences are repeatably observed across multiple PEA- and BA-based HSs (Figure A3.9) and may correspond to the relative formation energies for different n members of each RPP phase system.[52] For solar applications, this means that even if 2D/3D interdiffusion cannot be stopped altogether, the consequences may be partially controlled by choosing a 2D phase which is limited in possible restructuring products. The wide range of resolvable RPP phases in each n = 1 LA|3D PL spectrum also suggests the potential use of assembled 2D/3D HSs as systems for RPP phase exploration to guide the synthesis of higher n analogues of emerging 2D RPPs.

A less explored family of 2D overlayers are "quasi-2D" (n > 1) RPP phases, which are seeing increased attention as passivation layers due to their favorable band alignments to 3D $APbI_3$-based absorbers.[24,28] To explore these interfaces, we subjected the homologous series of n

= 1-4 BA-MA RPPs on 3D $MAPbI_3$ to the same ambient diffusion conditions and monitored evolution of their PL spectra (Figure 4.3e-h). Each phase-pure overlayer restructures into a diffusion cascade in a fashion similar to their n = 1 counterpart (Figure 4.3e) and over similar timescales, but the restructuring only proceeds toward the 3D perovskite phase. Put simply, n phase redistribution never proceeds "backwards" from the initial n phase of the overlayer. This provides another mechanism to mitigate the effects of 2D/3D interdiffusion: if higher n phase-pure overlayers can be synthesized, the range of diffusion products – and correspondingly the distribution of band energies at the interface – will be limited by the starting n phase; even though utilizing higher n phases alone may not prevent 2D/3D interdiffusion.

4.4. Thermodynamic Stability of RPP Overlayers with Oversized A-Site Cations

The study of ambient diffusion in 2D/3D HSs with various n phases and spacer cations revealed that the outcome of 2D/3D interdiffusion is substantially affected by the thermodynamics of phase formation of the interdiffusion products. This poses a new question: if a 2D/3D interface is designed such that the RPP diffusion products are not thermodynamically stable, can 2D/3D restructuring be prevented altogether? One way in which this approach could be explored is through tuning of the A-site cation in RPP phases. In 3D perovskites, great advances in absorber stability have been achieved by replacing unstable components of the 3D structure. Most notably, minimizing the incorporation of MA and replacing it with more stable cations like FA and Cs has yielded simultaneous improvements in performance and stability.[53,54] MA-free perovskites have also been explored in RPP photovoltaics to a similar effect,[55] but there is also an entirely unique class of large A-site cations that can be incorporated into some RPP structures due to relaxed structural tolerances vs. their 3D analogues.[56–58] The 3D A-site can only be occupied by a narrow range of cations (Cs, MA, FA) due to geometric constraints of the perovskite lattice as empirically

described by Goldschmidt's tolerance factor. These constraints are relaxed in RPPs because the spacer cations can compensate for structural distortions in isolated perovskite slabs that would not be geometrically possible in an uninterrupted 3D perovskite lattice, resulting in n = 2&3 RPP phases containing "oversized" A-site cations that cannot form a corresponding 3D perovskite phase, like guanidinium (GA) or ethylammonium (EA) (Figure 4.4a).

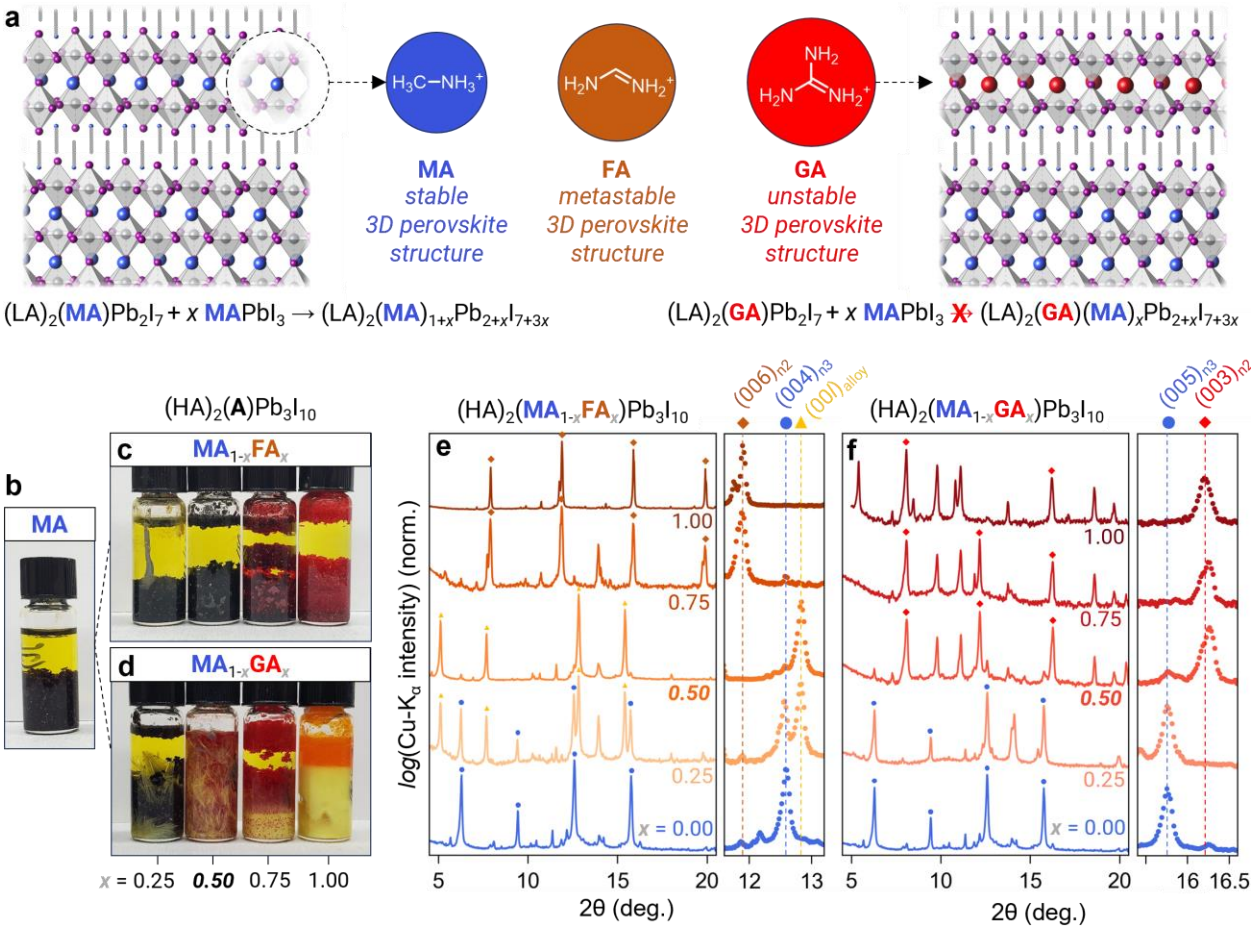

Figure 4.4. Limits of oversized A-site alloying in $n > 2$ RPPs. **(a)** Scheme depicting hypothetical thermodynamic stabilization of 2D/3D interfaces using oversized 2D A-site cations. **(b-d)** Images of RPP precipitates formed after alloying n = 3 HA-MA precursor solutions of with x fraction of oversized A cations: **(b)** non-alloyed n = 3 HA-MA, **(c)** HA-$MA_{1-x}FA_x$, **(d)** HA-$MA_{1-x}GA_x$. Some of these phase separate into crystals of different colors. Vials are 1.2 cm in diameter. **(e,f)** Powder

X-ray diffraction patterns of the precipitates from the vials shown in (b-d). Markers indicate interlayer reflections (e.g. (00*l*)) of known $n = 2/3$ phases in the phase system. Triangular markers indicate reflections assigned to a hypothesized alloyed $n = 3$ HA-MA/FA phase.

To explore the concept, we first evaluated the hypothetical outcome of the first interdiffusion step between a 3D perovskite and a phase-pure $n = 2$ RPP overlayer: a $n = 3$ RPP phase. Using HA as a common spacer cation, we took supersaturated aqueous precursor solutions known to yield phase-pure bulk crystals of $n = 3$ HA-MA,[59] and iteratively replaced the 3D-compatible MA with an increasing fraction x of the larger A-site cations FA or GA (Figure 4.4b-d). Photographs of the resulting bulk precipitates show substantial colorimetric changes as the nominal mean A-site cation becomes increasingly oversized. In the $MA_{1-x}FA_x$ case (Figure 4.4c), the maroon (nearly black) $n = 3$ crystals can accommodate up to 50% ($x = 0.5$) FA precursor content, before excess FA preferentially precipitates as red plates of $n = 2$ HA-FA. This transition is visible at $x = 0.75$, where red and maroon $n = 2$ and $n = 3$ phases coprecipitate from the same supersaturated precursor solution. The same system is far less tolerant to alloying with the much larger GA cation (Figure 4.4d), showing signs of immiscibility at the lowest alloying increment we investigated ($MA_{0.75}GA_{0.25}$). At first, GA appears to coprecipitate with the maroon $n = 3$ HA-MA plates as colorless needles, likely corresponding to the non-perovskite (monoclinic) phase $GAPbI_3$ consisting of parallel 1D chains of edge-sharing $[PbI_6]^{4-}$ octahedra.[56] At 50% GA content, there is no visible $n = 3$ HA-MA precipitate, nearly entirely being replaced by red $n = 2$ HA-GA and the monoclinic needle phase.[56] Further alloying with GA seems to push the system toward lower n phases (orange possibly corresponding to $n = 1$ HA and/or $n = 1$ GA 2D perovskites) and more needles of $GAPbI_3$.

We studied the miscibility of the $n = 3$ HA-$MA_{1-x}A_x$ phases in more detail by analyzing powder X-ray diffraction (PXRD) of these alloyed precipitates (Figure 4.4e,f). The relative amount of $n = 2$ reflections (annotated as diamonds) vs. $n = 3$ reflections (annotated as dots) in each pattern at different x values affirm what is visible to the eye, but there are notable differences in the $n = 3$ reflections as the alloying content of each cation increases. In the FA case, a slight shift of the $n = 3$ (00l) reflections to lower diffraction angles (Figure 4.4e, right) is conducive to minor lattice expansion as the larger FA cations occupy A-sites in the $n = 3$ slabs, but interestingly, strong peaks resembling (00l) reflections of a layered perovskite (yellow triangles) emerge in tandem with the $n = 3$ alloy. Unlike the original $n = 3$ HA-MA phase and the final $n = 2$ HA-FA phase at 100% FA, the angles and periodicity of the reflections could not be assigned to a known phase, possibly indicating the formation of a $MA_{1-x}FA_x$ multi-cation phase with a structure distinct from the stochastic alloy. At 50% FA content, reflections from this unknown layered phase are the only significant signal in the PXRD pattern, possibly indicating that a unique phase is formed at a 1:1 MA:FA stoichiometry.

In the GA case, the $n = 3$ reflections display no resolvable shift from the starting HA-MA phase at $x = 0.25$, suggesting that little to no GA is being incorporated into the $n = 3$ HA-MA lattice (Figure 4.4f, right). By $x = 0.50$, $n = 2$ HA-GA (00l) reflections dominate the pattern and grow more prominent from there on. In the context of 2D/3D interdiffusion, a stoichiometric reaction of $MAPbI_3$ with one layer of $n = 2$ $(HA)_2(A)Pb_2I_7$ would yield a layer of $n = 3$ $(HA)_2(MA^{3D})(A^{2D})Pb_3I_{10}$, in which 50% of the A-site occupants would originate from either layer. As such, the 50/50 alloy is most pertinent to the stabilization hypothesis. Since FA seems to be tolerant to alloying up to 50%, it would pass the initial thermodynamic barrier and proceed to form higher n phases of decreasing FA content as $MAPbI_3$ units are added. GA, on the other hand, seems

unable to form a 50/50 alloy with n = 3 HA-MA, making the n = 2 HA-GA RPP a reasonable candidate to explore as a thermodynamically stable 2D overlayer.

4.5. Stability of 2D/3D Interfaces Incorporating Oversized A-Site Cations

We then tested the stability of GA-containing 2D RPP overlayers by preparing n = 2 HA-A|3D HSs with either MA or GA A-site cations and subjecting them to extensive accelerated diffusion conditions. We employed time-of-flight secondary ion mass spectrometry (ToF-SIMS) and corresponding PL spectroscopy of similar HSs (Figure 4.5) to directly probe and understand the phase redistribution and spatial extent of ion interdiffusion at the 2D/3D interfaces. To distinguish MA originating from the n = 2 HA-MA overlayers from the $MAPbI_3$ substrates in the SIMS depth profiles, we grew isotopically labelled 3D SCs using methylammonium-^{13}C iodide ((^{13}C-MA)I) as a precursor salt.

Figure 4.5a-g contrasts SIMS depth profiles of n = 2 HA-MA|(^{13}C-MA)PbI_3 HSs with analogous n = 2 HA-GA|(^{13}C-MA)PbI_3 HSs at different stages of diffusion. The 2D/3D interfaces are best resolved in the depth profiles as the crossing point of the 2D $[HA]^+$ signal and the 3D $[^{13}C\text{-}MA]^+$ signal. Correlating AFM topography of the overlayer step heights to the $[HA]^+/[^{13}C\text{-}MA]^+$ crossover time in SIMS of the HSs in Figure 4.5a and Figure 4.5e yield the sputtering rate of the depth profiles to be ~1.2 nm/s (Figure A3.10). Comparing the $[MA]^+$ signal to the $[HA]^+$ signal in the n = 2 HA-MA|(^{13}C-MA)PbI_3 HS indicates substantial diffusion from the original 2D overlayer into the 3D perovskite even at RT. Initially, the onset of the $[MA]^+$ profile uniformly overlaps with that of the $[HA]^+$ profile (Figure 4.5a), but as interdiffusion increases over time an increasing proportion of the 2D $[MA]^+$ signal is overlapped with the onset of the 3D $[^{13}C\text{-}MA]^+$ signal and past the 2D/3D boundary (Figure 4.5b). Eventually, the majority of the 2D MA cations reside at

the same depths as the 3D ^{13}C-MA cations, and the overlap of the HA^+ and ^{13}C-MA^+ profiles is substantially increased (Figure 4.5c). The relatively static nature of $[HA]^+$ species vs. $[MA]^+$ implies that A-site cations are the primary agents of interdiffusion, whereas the 2D overlayer is essentially a membrane-like scaffold through which A-site cations interdiffuse between the 3D and 2D perovskite. The same profiles for the n = 2 HA-GA|(^{13}C-MA)PbI_3 HS paint a markedly different picture. From the very beginning, the propagation of GA cations extends far beyond the 2D/3D boundary, although the profile appears relatively uniform vs. $[MA]^+$ from n = 2 HA-MA (Figure 4.5d). As diffusion time increases, neither the extent of the $[GA]^+$ profile nor its relative abundance in the 2D vs. 3D layer appears to change, although the relative overlap of the $[HA]^+$ and [^{13}C-$MA]^+$ profiles appears to increase in a similar fashion to the n = 2 HA-MA|(^{13}C-MA)PbI_3 HSs (Figure 4.5e,f).

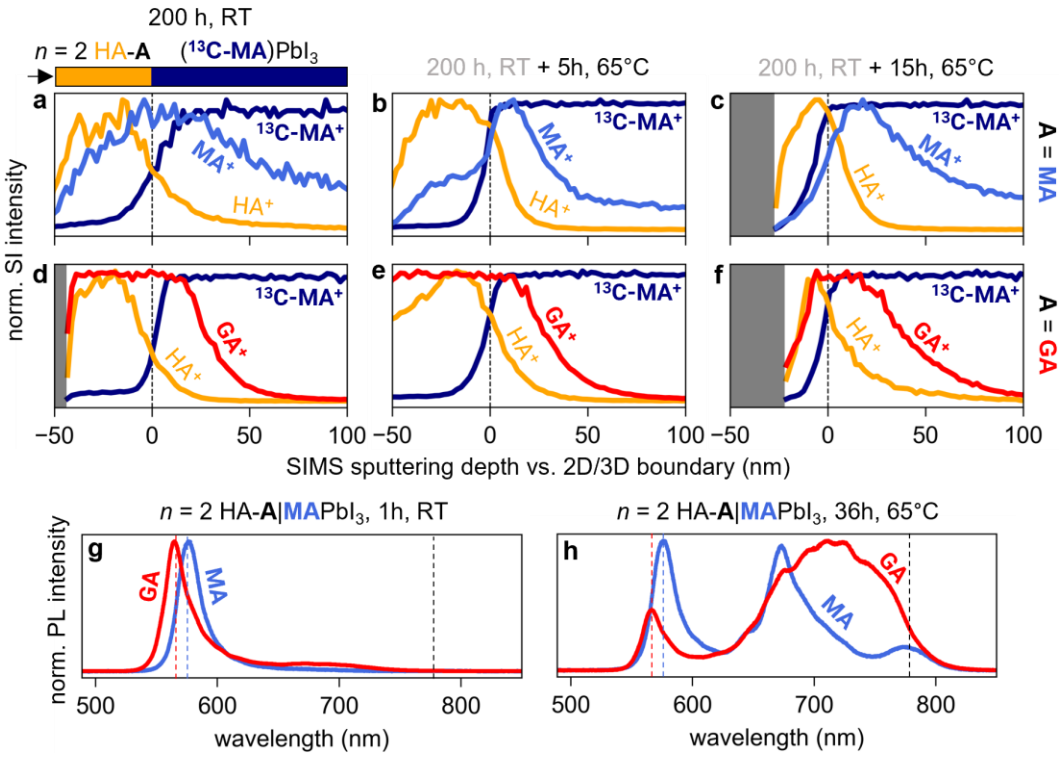

Figure 4.5. Stability of 2D/3D HSs with oversized A-site cations. **(a-f)** ToF-SIMS depth profiles of isotopically labelled n = 2 HA-A|3D HSs with MA **(a-c)** vs. GA **(d-f)** 2D A-site cations at various states of diffusion: RT **(a**,**d)**, 5h at 65°C **(b**,**e)**, 15h at 65°C **(c**,**f)**. **(g,h)** PL spectra of n = 2 HA-A|3D HSs with MA vs. GA 2D A-site cations at various states of diffusion: RT **(g)**, 36h at 65°C **(h)**.

To evaluate structural changes resulting from the cation interdiffusion, we directly compared PL spectra from systems analogous to those investigated via ToF-SIMS under accelerated diffusion lasting up to 72 h (Figure 4.5g,h). From a relatively phase-pure 2D overlayer in fresh HSs at RT (Figure 4.5g), both n = 2 HA-MA and n = 2 HA-GA overlayers are extensively restructured into a series of $n \geq 4$ RPP phases under accelerated interdiffusion, evidenced by increasing amounts of PL from $n \geq 4$ & 3D perovskite in the HS spectra after 36 h at 65°C (Figure 4.5h). It is clear from the SIMS and PL data that even though a n = 3 product is not attainable from alloying of bulk precursors of n = 2 HA-GA, cations freely migrate so extensively at the 2D/3D boundary that viable high-n cation mixtures can be accessed. This combines with the investigations of interdiffusion earlier in this work to paint a more nuanced explanation of restructuring at the 2D/3D boundary. The restructuring of the 2D/3D interface is characterized by discrete transformations of the 2D overlayer into RPP phases of increasing n, but that discrete process is mediated by a continuous flow of 2D and 3D A-site cations across the boundary. This implies that stabilization of the 2D/3D interface necessitates simultaneous immobilization of ion migration and thermodynamic stabilization of the 2D overlayer.

A final alteration to these systems that could potentially improve the interface stability lies on the 3D side of the interface. Throughout this work, $MAPbI_3$ was used to demonstrate 2D/3D interdiffusion at its most severe, but the most competitive LHP absorbers have an ever-decreasing

MA content in favor of more stable A-site cations.[7,54,60,61] Despite this, nearly no investigations have been performed directly studying the stability of 2D/3D interfaces in which the 3D layer is thermodynamically stabilized. To investigate this, we performed the same accelerated diffusion study coupled with ToF-SIMS and PL analysis, except we replaced the $MAPbI_3$ 3D phase with an MA-free composition of $(FA_{0.9}Cs_{0.1})PbI_3$ (Figure 4.6a; see methods in Appendix 3 for details on growth of this phase via inverse temperature crystallization).

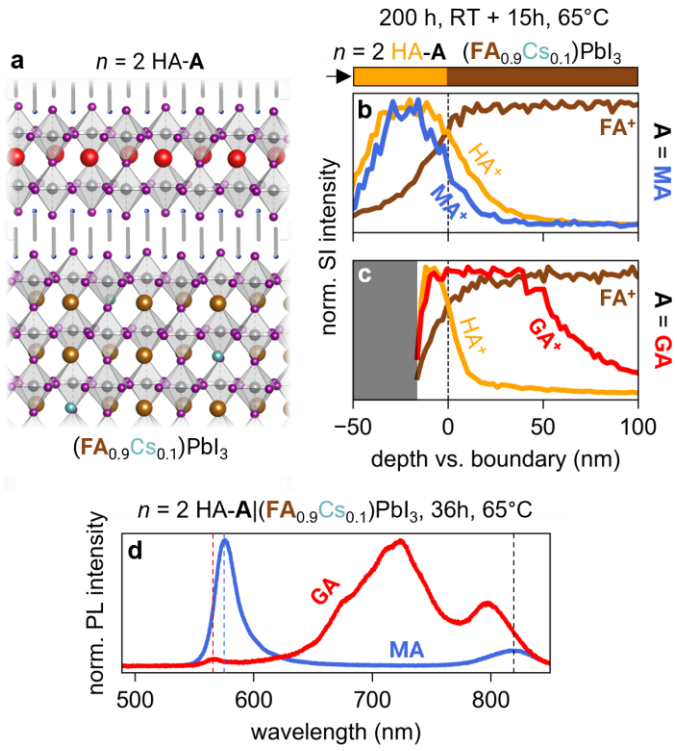

Figure 4.6. Stability of 2D/3D HSs with MA-free 3D LHPs. **(a)** Depiction of a n = 2 HA-A|$(FA_{0.9}Cs_{0.1})PbI_3$ HS. **(b,c)** ToF-SIMS depth profiles of n = 2 HA-A|3D HSs with MA **(b)** vs. GA **(g)** 2D A-site cations after accelerated diffusion conditions. **(d)** PL spectrum of n = 2 HA-A|3D HSs with MA vs. GA 2D A-site cations after accelerated diffusion conditions.

After the same extensive diffusion conditions, the n = 2 HA-GA|$(FA_{0.9}Cs_{0.1})PbI_3$ HS undergoes as much, if not more A-site interdiffusion than its $MAPbI_3$-based counterpart (Figure

4.6c), and surprisingly, the $n = 2$ HA-MA overlayer has nearly no signs of A-cation migration from the 2D overlayer into the 3D substrate (Figure 4.6b). In fact, after 15 h accelerated ageing at 65 °C, the $n = 2$ HA-MA|$(FA_{0.9}Cs_{0.1})PbI_3$ HS has a less diffuse MA^+ profile than the ambient control of the analogous $MAPbI_3$-based HS. This unexpected stabilization is also observed in PL spectra of analogous HSs (Figure 4.6d & Figure A3.11), in which the GA-based HS undergoes extensive transformation into high-n RPP phases, but there are no notable signs of restructuring in the $n = 2$ HA-MA|$(FA_{0.9}Cs_{0.1})PbI_3$ HS after 36 h accelerated ageing at 65°C. The $n = 2$ emission feature decreases in intensity overtime, but this was also observed in isolated RPP sheets on substrates under similar ageing conditions (Figure A3.12). Additionally, the $n = 2$ HA-GA|$(FA_{0.9}Cs_{0.1})PbI_3$ HS shows an emergent emission peak that is slightly blueshifted from the expected emission of pure 3D $(FA_{0.9}Cs_{0.1})PbI_3$ (indicated by a black dashed line, see Figure A3.13 for a reference spectrum), implying that GA cations may be able to form a 3D or quasi-3D LHP phase when mixed in the FA/Cs lattice. The widened bandgap may originate from lattice strain as the oversized cation is incorporated into the 3D lattice, as observed in RPP phases containing extremely oversized A-site cations.[62]

4.6. Performance Implications of 2D/3D Restructuring

Having thoroughly explored the structural parameters that affect 2D/3D interdiffusion, we also sought to gain an understanding of how 2D/3D restructuring affects photophysical characteristics of 2D-passivated LHP absorbers and potentially their performance in solar devices. From the results above, two major performance implications can already be understood. The first relates to the expansion of the effective thickness of the 2D overlayer as it is restructured, which as previously stated can modify the energy landscape and impedance of the 2D/3D interface (see §4.2). The second relates to the effects of the restructured 2D overlayer on light attenuation within

the solar cell. Since 2D/3D interdiffusion transforms a phase-pure 2D perovskite overlayer into a cascade of *n* phases, the wavelengths at which the 2D overlayer attenuates light would be broadened. PLE analysis of various *n* phase overlayers shows that 2D overlayers of higher *n* RPPs absorb a broader range of the visible spectrum before the light is absorbed by the 3D LHP beneath it (Figure A3.6). This limits device configurations containing unstable 2D/3D interfaces to the "buried" interface in single junction devices because such absorption losses on the sun-facing side would reduce external quantum efficiency. The same issue complicates the integration of 2D passivating layers into tandem or other multi-junction cells because 2D/3D restructuring on either side of a wide bandgap (WBG) perovskite top cell could decrease the solar flux incident upon the bottom cell.

We also sought to understand how 2D/3D restructuring affects the passivation of the 3D perovskite absorber. To probe this, we used radiative recombination kinetics as a proxy to monitor carrier trapping and measured 3D perovskite emission from *n* = 2 HA-MA|$MAPbI_3$ vs. *n* = 2 HA-GA|$MAPbI_3$ HSs using time-resolved photoluminescence (TRPL) microscopy as they underwent extensive ambient diffusion (Figure 4.7). Over an extended period under an inert nitrogen atmosphere enabled by an optical environmental chamber, there is no observable change in the TRPL transients of a reference surface of bare $MAPbI_3$ with no 2D overlayer (Figure 4.7a), ensuring that any resulting changes in TRPL kinetics in the HS regions are an effect of 2D/3D restructuring, not environmental degradation.

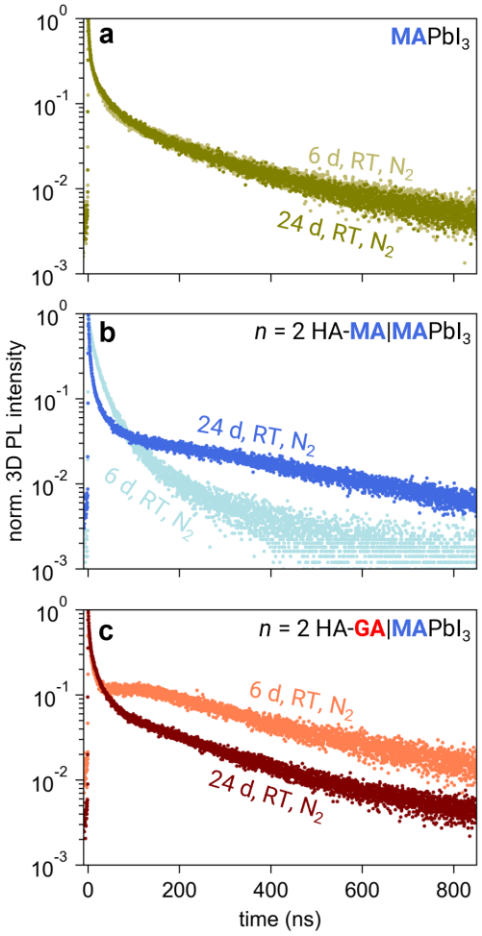

Figure 4.7. TRPL analysis of $n = 2$ HA-A HSs. **(a-c)** TRPL transients of 3D perovskite emission at short vs. long ambient diffusion times for bare $MAPbI_3$ **(a)**, $n = 2$ HA-MA|$MAPbI_3$ **(b)** and $n = 2$ HA-GA|$MAPbI_3$ HSs **(c)**.

We then compared a $n = 2$ HA-MA|$MAPbI_3$ HS to a $n = 2$ HA-GA|$MAPbI_3$ HS under the same ambient conditions (Figure 4.7b,c). In the case of the $n = 2$ HA-MA|$MAPbI_3$ HS, the long-term (>200 ns) PL lifetime of the underlying $MAPbI_3$ surface substantially increased, suggesting that surface trap density decreased as the 2D overlayer was restructured. In contrast, the $n = 2$ HA-GA|$MAPbI_3$ HS showed little change in long-term decay characteristics, but in the fresh HS there was an unusual intermediate period where the recombination rate was remarkably near-constant.

Due to extensive interdiffusion and restructuring, higher *n* RPP restructuring products could not be spectrally isolated from the 3D emission due to peak overlap. The result is that the short-term timescale of each HS transient is superimposed with the sub-100 ns PL emission of the 2D overlayer, and thus does not serve as a reliable gauge of 3D emission characteristics. The same is not so for the longer-term decay component, which substantially exceeds the radiative lifetime of the 2D overlayers. The increase in long-term PL lifetime in the $n = 2$ HA-MA|$MAPbI_3$ HS implies that restructuring may eliminate traps that were originally present at the 2D/3D interface, which facilitate non-radiative (Shockley–Reed–Hall) recombination and decrease long-term PL lifetime,[63] whereas minimal change in the $n = 2$ HA-GA|$MAPbI_3$ HS indicates that some restructured phases do not yield equivalent improvements in the defect environment near the surface. This lack of improvement could possibly be due to a compromise of photophysical performance due to lattice distortions induced by the oversized A-site cation, which may counteract improvements induced by passivation.[62,64,65]

4.7. Conclusion

Using van der Waals assembly of separately synthesized high-quality 2D RPP microsheets and 3D perovskite single crystals, we prepared a wide variety of atomically precise 2D/3D halide perovskite heterostructures and studied their ion interdiffusion dynamics and phase restructuring under ambient and accelerated diffusion conditions. Analysis of the interdiffusion products via PL microscopy and ToF-SIMS depth profiling revealed that phase-pure 2D RPP overlayers are transformed in discrete steps into a sequential cascade of RPP phases as A-cations diffuse continuously from 3D into 2D perovskite layers. The 2D/3D restructuring leads to expansion of the effective thickness of the 2D perovskite overlayer and broadening of 2D phase dispersity over a period of days but does not necessarily compromise the passivating effect of the 2D perovskite

overlayer. Systematic studies of 2D/3D interdiffusion across a broad scope of 2D overlayers with various spacer cations (LA) and layer thicknesses (n) show that nearly all major categories of RPPs are subject to interdiffusion with kinetic timescales well under the life cycle of a solar cell, but the distribution of quasi-2D phases after restructuring is determined in-part by the formation thermodynamics of each component of a given RPP phase system. Finally, we investigated the possibility of thermodynamically blocking 2D restructuring by incorporating 2D overlayers with oversized A-site cations that cannot form corresponding 3D structures. We found that even when high n analogues of $n = 2$ phases containing oversized A-cations cannot form in the bulk, dynamic restructuring at the 2D/3D interface is still possible due to the overwhelming cation mixing that occurs via interdiffusion, but surprisingly, some MA-based 2D RPP overlayers can be stabilized when interfaced with MA-free 3D absorbers, even when the oversized analogue of the same 2D overlayer is not stable in the same configuration. These findings deepen the mechanistic understanding of how 2D/3D diffusion occurs in 2D/3D perovskite HSs, and the connection to key structural parameters of the 2D perovskite overlayer reveal several new considerations that should be considered when attempting to design stable 2D/3D interfaces for high performance perovskite solar cells.

4.8. References

(1) Chapin, D. M.; Fuller, C. S.; Pearson, G. L. A New Silicon P-n Junction Photocell for Converting Solar Radiation into Electrical Power. *J. of Appl. Phys.* **1954**, *25* (5), 676–677.

(2) Kojima, A.; Teshima, K.; Shirai, Y.; Miyasaka, T. Organometal Halide Perovskites as Visible-Light Sensitizers for Photovoltaic Cells. *J. Am. Chem. Soc.* **2009**, *131* (17), 6050–6051.

(3) *Best Research-Cell Efficiency Chart*. https://www.nrel.gov/pv/cell-efficiency.html (accessed 2023-12-04).

(4) Rong, Y.; Hu, Y.; Mei, A.; Tan, H.; Saidaminov, M. I.; Seok, S. I.; McGehee, M. D.; Sargent, E. H.; Han, H. Challenges for Commercializing Perovskite Solar Cells. *Science* **2018**, *361* (6408), eaat8235.

(5) Nie, W.; Tsai, H.; Asadpour, R.; Blancon, J.-C.; Neukirch, A. J.; Gupta, G.; Crochet, J. J.; Chhowalla, M.; Tretiak, S.; Alam, M. A.; Wang, H.-L.; Mohite, A. D. High-Efficiency Solution-Processed Perovskite Solar Cells with Millimeter-Scale Grains. *Science* **2015**, *347* (6221), 522.

(6) Niu, T.; Lu, J.; Munir, R.; Li, J.; Barrit, D.; Zhang, X.; Hu, H.; Yang, Z.; Amassian, A.; Zhao, K.; Liu, S. (Frank). Stable High-Performance Perovskite Solar Cells via Grain Boundary Passivation. *Adv. Mater.* **2018**, *30* (16), 1706576.

(7) Turren-Cruz, S.-H.; Hagfeldt, A.; Saliba, M. Methylammonium-Free, High-Performance, and Stable Perovskite Solar Cells on a Planar Architecture. *Science* **2018**, *362* (6413), 449–453.

(8) Doherty, T. A. S.; Winchester, A. J.; Macpherson, S.; Johnstone, D. N.; Pareek, V.; Tennyson, E. M.; Kosar, S.; Kosasih, F. U.; Anaya, M.; Abdi-Jalebi, M.; Andaji-Garmaroudi, Z.; Wong, E. L.; Madéo, J.; Chiang, Y.-H.; Park, J.-S.; Jung, Y.-K.; Petoukhoff, C. E.; Divitini, G.; Man, M. K. L.; Ducati, C.; Walsh, A.; Midgley, P. A.; Dani, K. M.; Stranks, S. D. Performance-Limiting Nanoscale Trap Clusters at Grain Junctions in Halide Perovskites. *Nature* **2020**, *580* (7803), 360–366.

(9) Macpherson, S.; Doherty, T. A. S.; Winchester, A. J.; Kosar, S.; Johnstone, D. N.; Chiang, Y.-H.; Galkowski, K.; Anaya, M.; Frohna, K.; Iqbal, A. N.; Nagane, S.; Roose, B.; Andaji-Garmaroudi, Z.; Orr, K. W. P.; Parker, J. E.; Midgley, P. A.; Dani, K. M.; Stranks, S. D. Local Nanoscale Phase Impurities Are Degradation Sites in Halide Perovskites. *Nature* **2022**, *607* (7918), 294–300.

(10) Jiang, Q.; Zhao, Y.; Zhang, X.; Yang, X.; Chen, Y.; Chu, Z.; Ye, Q.; Li, X.; Yin, Z.; You, J. Surface Passivation of Perovskite Film for Efficient Solar Cells. *Nat. Photonics* **2019**, *13* (7), 460–466.

(11) Marshall, K. P.; Walker, M.; Walton, R. I.; Hatton, R. A. Enhanced Stability and Efficiency in Hole-Transport-Layer-Free $CsSnI_3$ Perovskite Photovoltaics. *Nat. Energy* **2016**, *1* (12), 1–9.

(12) Metcalf, I.; Sidhik, S.; Zhang, H.; Agrawal, A.; Persaud, J.; Hou, J.; Even, J.; Mohite, A. D. Synergy of 3D and 2D Perovskites for Durable, Efficient Solar Cells and Beyond. *Chem. Rev.* **2023**, *123* (15), 9565–9652.

(13) Smith, I. C.; Hoke, E. T.; Solis-Ibarra, D.; McGehee, M. D.; Karunadasa, H. I. A Layered Hybrid Perovskite Solar-Cell Absorber with Enhanced Moisture Stability. *Angew. Chem. Int. Ed.* **2014**, *53* (42), 11232–11235.

(14) Huang, Z.; Proppe, A. H.; Tan, H.; Saidaminov, M. I.; Tan, F.; Mei, A.; Tan, C.-S.; Wei, M.; Hou, Y.; Han, H.; Kelley, S. O.; Sargent, E. H. Suppressed Ion Migration in Reduced-Dimensional Perovskites Improves Operating Stability. *ACS Energy Lett.* **2019**, *4* (7), 1521–1527.

(15) Cho, J.; DuBose, J. T.; Le, A. N. T.; Kamat, P. V. Suppressed Halide Ion Migration in 2D Lead Halide Perovskites. *ACS Mater. Lett.* **2020**, *2* (6), 565–570.

(16) Deng, S.; Shi, E.; Yuan, L.; Jin, L.; Dou, L.; Huang, L. Long-Range Exciton Transport and Slow Annihilation in Two-Dimensional Hybrid Perovskites. *Nat. Commun.* **2020**, *11* (1), 664.

(17) Grancini, G.; Roldán-Carmona, C.; Zimmermann, I.; Mosconi, E.; Lee, X.; Martineau, D.; Narbey, S.; Oswald, F.; De Angelis, F.; Graetzel, M.; Nazeeruddin, M. K. One-Year Stable Perovskite Solar Cells by 2D/3D Interface Engineering. *Nat. Commun.* **2017**, *8* (1), 15684.

(18) Gharibzadeh, S.; Abdollahi Nejand, B.; Jakoby, M.; Abzieher, T.; Hauschild, D.; Moghadamzadeh, S.; Schwenzer, J. A.; Brenner, P.; Schmager, R.; Haghighirad, A. A.; Weinhardt, L.; Lemmer, U.; Richards, B. S.; Howard, I. A.; Paetzold, U. W. Record Open-Circuit Voltage Wide-Bandgap Perovskite Solar Cells Utilizing 2D/3D Perovskite Heterostructure. *Adv. Energy Mater.* **2019**, *9* (21), 1803699.

(19) Chen, H.; Teale, S.; Chen, B.; Hou, Y.; Grater, L.; Zhu, T.; Bertens, K.; Park, S. M.; Atapattu, H. R.; Gao, Y.; Wei, M.; Johnston, A. K.; Zhou, Q.; Xu, K.; Yu, D.; Han, C.; Cui, T.; Jung, E. H.; Zhou, C.; Zhou, W.; Proppe, A. H.; Hoogland, S.; Laquai, F.; Filleter, T.; Graham, K. R.; Ning, Z.; Sargent, E. H. Quantum-Size-Tuned Heterostructures Enable Efficient and Stable Inverted Perovskite Solar Cells. *Nat. Photon.* **2022**, *16* (5), 352–358.

(20) Stoumpos, C. C.; Cao, D. H.; Clark, D. J.; Young, J.; Rondinelli, J. M.; Jang, J. I.; Hupp, J. T.; Kanatzidis, M. G. Ruddlesden–Popper Hybrid Lead Iodide Perovskite 2D Homologous Semiconductors. *Chem. Mater.* **2016**, *28* (8), 2852–2867.

(21) Oswald, I. W. H.; Koegel, A. A.; Neilson, J. R. General Synthesis Principles for Ruddlesden–Popper Hybrid Perovskite Halides from a Dynamic Equilibrium. *Chem. Mater.* **2018**, *30* (23), 8606–8614.

(22) Hou, J.; Li, W.; Zhang, H.; Sidhik, S.; Fletcher, J.; Metcalf, I.; Anantharaman, S. B.; Shuai, X.; Mishra, A.; Blancon, J.-C.; Katan, C.; Jariwala, D.; Even, J.; Kanatzidis, M. G.; Mohite, A. D. Synthesis of 2D Perovskite Crystals via Progressive Transformation of Quantum Well Thickness. *Nat. Synth.* **2023**, 1–11.

(23) Kodalle, T.; Moral, R. F.; Scalon, L.; Szostak, R.; Abdelsamie, M.; Marchezi, P. E.; Nogueira, A. F.; Sutter-Fella, C. M. Revealing the Transient Formation Dynamics and Optoelectronic Properties of 2D Ruddlesden-Popper Phases on 3D Perovskites. *Adv. Energy Mater.* **2023**, *13* (33), 2201490.

(24) Zhong, X.; Ni, X.; Sidhik, S.; Li, H.; Mohite, A. D.; Brédas, J.-L.; Kahn, A. Direct Characterization of Type-I Band Alignment in 2D Ruddlesden–Popper Perovskites. *Adv. Energy Mater. 12* (45), 2202333.

(25) Yuan, M.; Quan, L. N.; Comin, R.; Walters, G.; Sabatini, R.; Voznyy, O.; Hoogland, S.; Zhao, Y.; Beauregard, E. M.; Kanjanaboos, P.; Lu, Z.; Kim, D. H.; Sargent, E. H. Perovskite Energy Funnels for Efficient Light-Emitting Diodes. *Nat. Nanotechnol.* **2016**, *11* (10), 872–877.

(26) Proppe, A. H.; Quintero-Bermudez, R.; Tan, H.; Voznyy, O.; Kelley, S. O.; Sargent, E. H. Synthetic Control over Quantum Well Width Distribution and Carrier Migration in Low-Dimensional Perovskite Photovoltaics. *J. Am. Chem. Soc.* **2018**, *140* (8), 2890–2896.

(27) Jang, Y.-W.; Lee, S.; Yeom, K. M.; Jeong, K.; Choi, K.; Choi, M.; Noh, J. H. Intact 2D/3D Halide Junction Perovskite Solar Cells via Solid-Phase in-Plane Growth. *Nat. Energy* **2021**, *6* (1), 63–71.

(28) Sidhik, S.; Wang, Y.; De Siena, M.; Asadpour, R.; Torma, A. J.; Terlier, T.; Ho, K.; Li, W.; Puthirath, A. B.; Shuai, X.; Agrawal, A.; Traore, B.; Jones, M.; Giridharagopal, R.; Ajayan, P. M.; Strzalka, J.; Ginger, D. S.; Katan, C.; Alam, M. A.; Even, J.; Kanatzidis, M. G.; Mohite, A. D. Deterministic Fabrication of 3D/2D Perovskite Bilayer Stacks for Durable and Efficient Solar Cells. *Science* **2022**, *377* (6613), 1425–1430.

(29) Sutanto, A. A.; Drigo, N.; Queloz, V. I. E.; Garcia-Benito, I.; Kirmani, A. R.; Richter, L. J.; Schouwink, P. A.; Cho, K. T.; Paek, S.; Nazeeruddin, M. K.; Grancini, G. Dynamical Evolution of the 2D/3D Interface: A Hidden Driver behind Perovskite Solar Cell Instability. *J. Mater. Chem. A* **2020**, *8* (5), 2343–2348.

(30) Perini, C. A. R.; Rojas-Gatjens, E.; Ravello, M.; Castro-Mendez, A.-F.; Hidalgo, J.; An, Y.; Kim, S.; Lai, B.; Li, R.; Silva-Acuña, C.; Correa-Baena, J.-P. Interface Reconstruction from Ruddlesden–Popper Structures Impacts Stability in Lead Halide Perovskite Solar Cells. *Adv. Mater.* **2022**, *34* (51), 2204726.

(31) Sutanto, A. A.; Szostak, R.; Drigo, N.; Queloz, V. I. E.; Marchezi, P. E.; Germino, J. C.; Tolentino, H. C. N.; Nazeeruddin, M. K.; Nogueira, A. F.; Grancini, G. In Situ Analysis Reveals the Role of 2D Perovskite in Preventing Thermal-Induced Degradation in 2D/3D Perovskite Interfaces. *Nano Lett.* **2020**, *20* (5), 3992–3998.

(32) Fiorentino, F.; Albaqami, M. D.; Poli, I.; Petrozza, A. Thermal- and Light-Induced Evolution of the 2D/3D Interface in Lead-Halide Perovskite Films. *ACS Appl. Mater. Interfaces* **2022**, *14* (30), 34180–34188.

(33) Mathew, P. S.; Kamat, P. V. Cation Migration in Physically Paired 2D and 3D Lead Halide Perovskite Films. *Adv. Optical Mater.* **2023**, 2300957.

(34) Szabó, G.; Kamat, P. V. How Cation Migration across a 2D/3D Interface Dictates Perovskite Solar Cell Efficiency. *ACS Energy Lett.* **2023**, 193–200.

(35) Saidaminov, M. I.; Abdelhady, A. L.; Murali, B.; Alarousu, E.; Burlakov, V. M.; Peng, W.; Dursun, I.; Wang, L.; He, Y.; Maculan, G.; Goriely, A.; Wu, T.; Mohammed, O. F.; Bakr, O. M. High-Quality Bulk Hybrid Perovskite Single Crystals within Minutes by Inverse Temperature Crystallization. *Nat. Commun.* **2015**, *6* (1), 7586.

(36) Chen, Y.-X.; Ge, Q.-Q.; Shi, Y.; Liu, J.; Xue, D.-J.; Ma, J.-Y.; Ding, J.; Yan, H.-J.; Hu, J.-S.; Wan, L.-J. General Space-Confined On-Substrate Fabrication of Thickness-Adjustable Hybrid Perovskite Single-Crystalline Thin Films. *J. Am. Chem. Soc.* **2016**, *138* (50), 16196–16199.

(37) Fu, Y.; Zhu, H.; Chen, J.; Hautzinger, M. P.; Zhu, X.-Y.; Jin, S. Metal Halide Perovskite Nanostructures for Optoelectronic Applications and the Study of Physical Properties. *Nat. Rev. Mater.* **2019**, *4* (3), 169–188.

(38) Geim, A. K.; Grigorieva, I. V. Van Der Waals Heterostructures. *Nature* **2013**, *499* (7459), 419–425.

(39) Chen, Z.; Dong, Q.; Liu, Y.; Bao, C.; Fang, Y.; Lin, Y.; Tang, S.; Wang, Q.; Xiao, X.; Bai, Y.; Deng, Y.; Huang, J. Thin Single Crystal Perovskite Solar Cells to Harvest Below-Bandgap Light Absorption. *Nat. Commun.* **2017**, *8* (1), 1890.

(40) Seed, B. Silanizing Glassware. *Current Protocols in Cell Biology* **2000**, *8* (1), A.3E.1-A.3E.2.

(41) Campbell, P.; Green, M. A. Light Trapping Properties of Pyramidally Textured Surfaces. *J. of Appl. Phys.* **1987**, *62* (1), 243–249.

(42) Pan, D.; Fu, Y.; Spitha, N.; Zhao, Y.; Roy, C. R.; Morrow, D. J.; Kohler, D. D.; Wright, J. C.; Jin, S. Deterministic Fabrication of Arbitrary Vertical Heterostructures of Two-Dimensional Ruddlesden–Popper Halide Perovskites. *Nat. Nanotechnol.* **2021**, *16* (2), 159–165.

(43) Castellanos-Gomez, A.; Buscema, M.; Molenaar, R.; Singh, V.; Janssen, L.; van der Zant, H. S. J.; Steele, G. A. Deterministic Transfer of Two-Dimensional Materials by All-Dry Viscoelastic Stamping. *2D Materials* **2014**, *1* (1), 011002.

(44) Dang, Y.; Liu, Y.; Sun, Y.; Yuan, D.; Liu, X.; Lu, W.; Liu, G.; Xia, H.; Tao, X. Bulk Crystal Growth of Hybrid Perovskite Material $CH_3NH_3PbI_3$. *Cryst. Eng. Comm.* **2015**, *17* (3), 665–670.

(45) Koh, T. M.; Shanmugam, V.; Schlipf, J.; Oesinghaus, L.; Müller-Buschbaum, P.; Ramakrishnan, N.; Swamy, V.; Mathews, N.; Boix, P. P.; Mhaisalkar, S. G. Nanostructuring Mixed-Dimensional Perovskites: A Route Toward Tunable, Efficient Photovoltaics. *Adv. Mater.* **2016**, *28* (19), 3653–3661.

(46) Kuo, M.-Y.; Spitha, N.; Hautzinger, M. P.; Hsieh, P.-L.; Li, J.; Pan, D.; Zhao, Y.; Chen, L.-J.; Huang, M. H.; Jin, S.; Hsu, Y.-J.; Wright, J. C. Distinct Carrier Transport Properties Across Horizontally vs Vertically Oriented Heterostructures of 2D/3D Perovskites. *J. Am. Chem. Soc.* **2021**, *143* (13), 4969–4978.

(47) Khenkin, M. V.; Katz, E. A.; Abate, A.; Bardizza, G.; Berry, J. J.; Brabec, C.; Brunetti, F.; Bulović, V.; Burlingame, Q.; Di Carlo, A.; Cheacharoen, R.; Cheng, Y.-B.; Colsmann, A.; Cros, S.; Domanski, K.; Dusza, M.; Fell, C. J.; Forrest, S. R.; Galagan, Y.; Di Girolamo, D.; Grätzel, M.; Hagfeldt, A.; von Hauff, E.; Hoppe, H.; Kettle, J.; Köbler, H.; Leite, M. S.; Liu, S. (Frank); Loo,

Y.-L.; Luther, J. M.; Ma, C.-Q.; Madsen, M.; Manceau, M.; Matheron, M.; McGehee, M.; Meitzner, R.; Nazeeruddin, M. K.; Nogueira, A. F.; Odabaşı, Ç.; Osherov, A.; Park, N.-G.; Reese, M. O.; De Rossi, F.; Saliba, M.; Schubert, U. S.; Snaith, H. J.; Stranks, S. D.; Tress, W.; Troshin, P. A.; Turkovic, V.; Veenstra, S.; Visoly-Fisher, I.; Walsh, A.; Watson, T.; Xie, H.; Yıldırım, R.; Zakeeruddin, S. M.; Zhu, K.; Lira-Cantu, M. Consensus Statement for Stability Assessment and Reporting for Perovskite Photovoltaics Based on ISOS Procedures. *Nat. Energy* **2020**, *5* (1), 35–49.

(48) Stoumpos, C. C.; Soe, C. M. M.; Tsai, H.; Nie, W.; Blancon, J.-C.; Cao, D. H.; Liu, F.; Traoré, B.; Katan, C.; Even, J.; Mohite, A. D.; Kanatzidis, M. G. High Members of the 2D Ruddlesden-Popper Halide Perovskites: Synthesis, Optical Properties, and Solar Cells of $(CH_3(CH_2)_3NH_3)_2(CH_3NH_3)_4Pb_5I_{16}$. *Chem* **2017**, *2* (3), 427–440.

(49) Soe, C. M. M.; Nagabhushana, G. P.; Shivaramaiah, R.; Tsai, H.; Nie, W.; Blancon, J.-C.; Melkonyan, F.; Cao, D. H.; Traoré, B.; Pedesseau, L.; Kepenekian, M.; Katan, C.; Even, J.; Marks, T. J.; Navrotsky, A.; Mohite, A. D.; Stoumpos, C. C.; Kanatzidis, M. G. Structural and Thermodynamic Limits of Layer Thickness in 2D Halide Perovskites. *Proc. Nat. Acad. Sci.* **2019**, *116* (1), 58–66.

(50) Noel, N. K.; Abate, A.; Stranks, S. D.; Parrott, E. S.; Burlakov, V. M.; Goriely, A.; Snaith, H. J. Enhanced Photoluminescence and Solar Cell Performance via Lewis Base Passivation of Organic–Inorganic Lead Halide Perovskites. *ACS Nano* **2014**, *8* (10), 9815–9821.

(51) La-Placa, M.-G.; Gil-Escrig, L.; Guo, D.; Palazon, F.; Savenije, T. J.; Sessolo, M.; Bolink, H. J. Vacuum-Deposited 2D/3D Perovskite Heterojunctions. *ACS Energy Lett.* **2019**, *4* (12), 2893–2901.

(52) Forlano, K. M.; Roy, C. R.; Mihalyi-Koch, W.; Hossain, T.; Sanders, K.; Guzei, I.; Graham, K. R.; Wright, J. C.; Jin, S. High Layer Number (n = 1–6) 2D Ruddlesden–Popper Lead Bromide Perovskites: Nanosheets, Crystal Structure, and Optoelectronic Properties. *ACS Materials Lett.* **2023**, *5* (11), 2913–2921.

(53) Conings, B.; Drijkoningen, J.; Gauquelin, N.; Babayigit, A.; D'Haen, J.; D'Olieslaeger, L.; Ethirajan, A.; Verbeeck, J.; Manca, J.; Mosconi, E.; Angelis, F. D.; Boyen, H.-G. Intrinsic Thermal Instability of Methylammonium Lead Trihalide Perovskite. *Adv. Energy Mater.* **2015**, *5* (15), 1500477.

(54) Gao, X.-X.; Luo, W.; Zhang, Y.; Hu, R.; Zhang, B.; Züttel, A.; Feng, Y.; Nazeeruddin, M. K. Stable and High-Efficiency Methylammonium-Free Perovskite Solar Cells. *Adv. Mater.* **2020**, *32* (9), 1905502.

(55) Zeng, F.; Kong, W.; Liang, Y.; Li, F.; Lvtao, Y.; Su, Z.; Wang, T.; Peng, B.; Ye, L.; Chen, Z.; Gao, X.; Huang, J.; Zheng, R.; Yang, X. Highly Stable and Efficient Formamidinium-Based

2D Ruddlesden–Popper Perovskite Solar Cells via Lattice Manipulation. *Adv. Mater.* **2023**, *35* (42), 2306051.

(56) Fu, Y.; Hautzinger, M. P.; Luo, Z.; Wang, F.; Pan, D.; Aristov, M. M.; Guzei, I. A.; Pan, A.; Zhu, X.; Jin, S. Incorporating Large A Cations into Lead Iodide Perovskite Cages: Relaxed Goldschmidt Tolerance Factor and Impact on Exciton–Phonon Interaction. *ACS Cent. Sci.* **2019**, *5* (8), 1377–1386.

(57) Ramos-Terrón, S.; Jodlowski, A. D.; Verdugo-Escamilla, C.; Camacho, L.; de Miguel, G. Relaxing the Goldschmidt Tolerance Factor: Sizable Incorporation of the Guanidinium Cation into a Two-Dimensional Ruddlesden–Popper Perovskite. *Chem. Mater.* **2020**, *32* (9), 4024–4037.

(58) Fu, Y. Stabilization of Metastable Halide Perovskite Lattices in the 2D Limit. *Adv. Mater.* **2022**, *34* (9), 2108556.

(59) Spanopoulos, I.; Hadar, I.; Ke, W.; Tu, Q.; Chen, M.; Tsai, H.; He, Y.; Shekhawat, G.; Dravid, V. P.; Wasielewski, M. R.; Mohite, A. D.; Stoumpos, C. C.; Kanatzidis, M. G. Uniaxial Expansion of the 2D Ruddlesden–Popper Perovskite Family for Improved Environmental Stability. *J. Am. Chem. Soc.* **2019**, *141* (13), 5518–5534.

(60) Lee, J.-W.; Kim, D.-H.; Kim, H.-S.; Seo, S.-W.; Cho, S. M.; Park, N.-G. Formamidinium and Cesium Hybridization for Photo- and Moisture-Stable Perovskite Solar Cell. *Adv. Energy Mater.* **2015**, *5* (20), 1501310.

(61) Lee, J.-W.; Dai, Z.; Han, T.-H.; Choi, C.; Chang, S.-Y.; Lee, S.-J.; De Marco, N.; Zhao, H.; Sun, P.; Huang, Y.; Yang, Y. 2D Perovskite Stabilized Phase-Pure Formamidinium Perovskite Solar Cells. *Nat. Commun.* **2018**, *9* (1), 3021.

(62) Hautzinger, M. P.; Pan, D.; Pigg, A. K.; Fu, Y.; Morrow, D. J.; Leng, M.; Kuo, M.-Y.; Spitha, N.; Lafayette, D. P.; Kohler, D. D.; Wright, J. C.; Jin, S. Band Edge Tuning of Two-Dimensional Ruddlesden–Popper Perovskites by A Cation Size Revealed through Nanoplates. *ACS Energy Lett.* **2020**, *5* (5), 1430–1437.

(63) Kirchartz, T.; Márquez, J. A.; Stolterfoht, M.; Unold, T. Photoluminescence-Based Characterization of Halide Perovskites for Photovoltaics. *Adv. Energy Mater.* **2020**, *10* (26), 1904134.

(64) W. Jones, T.; Osherov, A.; Alsari, M.; Sponseller, M.; C. Duck, B.; Jung, Y.-K.; Settens, C.; Niroui, F.; Brenes, R.; V. Stan, C.; Li, Y.; Abdi-Jalebi, M.; Tamura, N.; Emyr Macdonald, J.; Burghammer, M.; H. Friend, R.; Bulović, V.; Walsh, A.; J. Wilson, G.; Lilliu, S.; D. Stranks, S. Lattice Strain Causes Non-Radiative Losses in Halide Perovskites. *Energ. Environ. Sci.* **2019**, *12* (2), 596–606.

(65) Ramos-Terrón, S.; Verdugo-Escamilla, C.; Camacho, L.; de Miguel, G. A-Site Cation Engineering in 2D Ruddlesden–Popper $(BA)_2(MA_{1-x}A_x)_2Pb_3I_{10}$ Perovskite Films. *Adv. Optical Mater.* **2021**, *9* (18), 2100114.

Appendix 1. Supplementary Information for Chapter 2

A1.1. Experimental Methods

Chemicals and Materials

All chemicals were used as purchased without further purification. Hydroiodic acid (HI, 57 wt.% in H_2O), hypophosphorous acid solution (H_3PO_2, 50 wt.% in H_2O), phenethylamine (PEA, 99%), *n*-hexylamine (HA, 99%), and lead(II) oxide (PbO, 99%) were purchased from Sigma-Aldrich. Hydrobromic acid (HBr, 48 wt.% in H_2O) was purchased from Alfa Aesar. Formamidinium acetate (FA(ac), 99%) was purchased from Acros Organics. p-type Si wafer substrates ((100), native oxide surface) were purchased from University Wafer. Polydimethylsiloxane film (PDMS, 17 mil) was purchased from Gel-Pak. Fluorinated ethylene propylene film (FEP, 5 mil) was cleaned with methanol and delicate task wipes prior to use in synthesis.

Aqueous Droplet Growth and Dry Transfer of Mixed-Halide RPP Microplates

All syntheses and dry transfers were done in ambient conditions. Room temperature ranged from 21-24 °C and relative humidity ranged from 24-29%.

Concentrated HI and HBr solutions were micropipetted into a glass scintillation vial to produce a mixed-halide HX solution totaling 900 μL in volume. The proportion of HI vs. HBr was chosen such that the iodide and bromide concentrations of the mixed-halide solution were at the desired molar percentages for a given synthesis (exact volumes in Table A1.1). PbO was then dissolved in the mixed-halide HX solution on a hot plate set to 120 °C. Before adding other precursors, the mixed-halide Pb^{2+} solution was left on heat for >15 min to ensure that iodide and bromide halidoplumbate complexes were at equilibrium.

In a separate glass vial, the appropriate amounts of amines (PEA or HA) for each desired phase were slowly added to 100 μL of H_3PO_2 solution via micropipette and, in the case of $n = 2$ HA-FA, FA(ac) was dissolved in the H_3PO_2 solution as well (exact concentrations in Table A1.2). The amine solution was then added to the mixed-halide Pb^{2+} solution, yielding yellow-to-white precipitates in the case of $n = 1$ phases and red-to-yellow precipitates in the case of $n = 2$ HA-FA-Pb-X. The precipitate was fully dissolved at 120-130 °C and was again allowed to sit on heat for >15 min to reduce residual I_2 and I_3^- that may have been oxidized in the HI. The heated precursor solution was then pipetted in 300 μL portions into polypropylene microcentrifuge tubes for droplet growth and allowed to cool to room temperature overnight.

Aqueous droplet growth of RPP microplates is described in detail in our previous work.[1,2] In brief, the centrifuge tubes containing RPP precipitates were precisely heated to the desired growth temperature (Table S2) in a PCR thermal cycler and allowed to equilibrate for >90 min. The supernatant of the heated solution was then drawn with a disposable pipet and dispensed onto a piece of FEP film at room temperature, where the slow growth of few-to-single grain RPP microplates was monitored under an optical microscope. After the desired crystal size was reached, the droplet was tilted off the hydrophobic FEP substrate into a glass catch pan and the FEP was quickly dried under a stream of compressed air, leaving a population of RPP microplates stuck to the surface of the FEP film. Some bromide-rich phases exhibited a growth bias toward the surface of the droplet, making residue-free droplet removal difficult. We resolved this by "mopping" the surface of the droplet with a second piece of FEP just before rolling the droplet into the catch pan. To avoid artificial phase mixing that could hypothetically occur if microsheets at the surface and microplates at the bottom were mixed, only microplates that precipitated to the bottom of the droplet were isolated via dry transfer for characterization.

The microplates on FEP were then dry transferred to other substrates for characterization using PDMS stamps. The transfer is most efficient when both the substrate and the PDMS stamp are rigid, flat, and clean. Localized pressure to encourage stamp wetting improved transfer yield, but care must be taken to avoid damaging the microplates. Keeping the PDMS stamp adhered to the destination substrate for an extended period (usually >30 min) before final removal seemed to improve the transfer yield.

Table A1.1. Volumes of HBr and HI to yield a target molar Br% in 900 µL of HI/HBr solution.

Br%	V_{HI} (µL, 57 wt. %)	V_{HBr} (µL, 48 wt. %)
5	862.4	37.6
10	824.2	75.8
15	785.3	114.7
20	745.7	154.3
25	705.4	194.6
30	664.4	235.6
35	622.6	277.4
40	580.1	319.9
45	536.7	363.3
50	492.5	407.5
55	447.5	452.5
60	401.6	498.4
65	354.8	545.2
70	307.1	592.9
75	258.5	641.5
80	248.6	651.4
85	238.7	661.3
90	228.8	671.2
95	218.8	681.2

For a volume V_{total} of mixed HX/HX' solution of a desired molar %X, the volumes of HX and HX' were computed using the following equations:

$$V_{HX} = V_{total}\frac{x_X M_{HX'}}{(1-x_X)M_{HX} + x_X M_{HX'}} \quad (1)$$

$$V_{HX'} = V_{total} - V_{HX} \quad (2)$$

where x_X is the molar fraction of X in the X/X' solution (e.g., 50% X ≡ x_X = 0.5), and M_{HX} and $M_{HX'}$ are the molarities of the HX and HX' solutions to be mixed.

Table A1.2. The precursor concentrations, volumetric fractions of solutions, and growth temperatures for synthesizing microplates of the parent RPP phases presented in the main text.

Compound	$(PEA)_2PbX_4$	$(HA)_2PbX_4$	$(HA)_2(FA)Pb_2X_7$
V_{HX} (µL)	900	900	900
V_{H3PO2} (µL)	100	100	100
[PbO] (mM)	100	100	400
[LA] (mM)	50	100	40
[A] (mM)	-	-	125
m_{PbO} (mg)	22.3	22.3	89.3
m_A (mg)	-	-	13.0
V_{LA} (µL)	6.29	13.14	5.26
T_{growth} (°C)	40	35	38

Powder X-Ray Diffraction

XRD measurements were performed on populations of intact RPP microplates on silicon wafer substrates prior to all other characterization to remove the possibility of photoinduced halide phase separation. XRD patterns were collected in a Bruker D8 Advance powder diffractometer using the Cu-K_α line. A knife edge was used to attenuate incident X-ray background at low diffraction angles.

Atomic Force Microscopy

AFM topography measurements were conducted using an Agilent Keysight 5500 atomic force microscope in tapping mode with a Bruker NCHV-A tip (spring constant of 40 Nm^{-1}).

Time-of-Flight Secondary Ion Mass Spectrometry

Samples for ToF-SIMS analysis were mixed-halide n = 2 HA-FA microplates near the crossover point of the I/Br phase system. They were dry transferred to a p-type Si substrate. Optical images, PL images and AFM topography images were collected prior to SIMS analysis, which was performed within 3 days of synthesis.

ToF-SIMS measurements were performed using a TOF-SIMS5 instrument (IONTOF GmbH, Münster, Germany) with dual beam noninterlaced mode depth profiling at the Environmental Molecular Sciences Laboratory (EMSL) of Pacific Northwest National Laboratory. A 2.0 keV Cs^+ beam was used as the sputtering beam, and a 25 keV Bi^+ beam was used as the analysis beam for ion image collection. The Cs^+ sputtering beam (~70 nA) was scanned over a 200 × 200 μm^2 area. The Bi^+ beam was focused to be about 0.40 μm in diameter with a beam current of about 1.20 pA at a 20 kHz frequency. During image collection, the Bi^+ beam was scanned with 256 × 256 pixels over an area of 70 × 70 μm^2 or 150 × 150 μm^2 at the Cs^+ sputter crater center. The noninterlaced mode was operated at 1.5 s sputtering time, 1.0 s pause time, and 6.55 s data collection time (2 scans of 256 × 256 pixels). A low energy (10 eV) electron flood gun was used for charge compensation in all measurements. Data reconstruction was performed to get digital zoom-in ion maps and depth profiles of interesting ion species at desirable areas.

Mass calibration, peak identification, and extraction of 3D x-y-z arrays for each ion channel were done using the pySPM python library developed by Oliver Scholder (Apache-2.0 license).[3] The iodide signals presented correspond to the $^{127}I^-$ peak in the mass spectrum. The x-y-z signals for monoatomic $^{79}Br^-$ and $^{81}Br^-$ species were saturated (Figure A1.1), so we used the sum of two dibromide cluster signals – $^{81}Br_2^-$ and $(^{79}Br^{81}Br)^-$ – as a more accurate representation of bromide content in the sample.

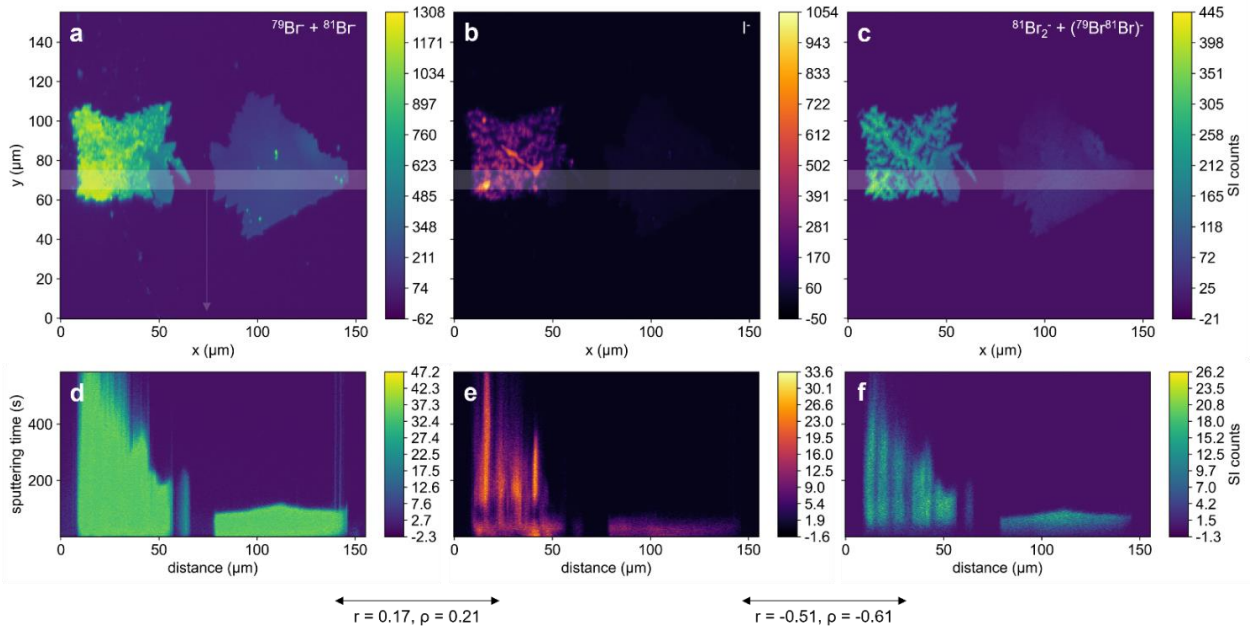

Figure A1.1. Comparison of the bromide signals measured via ToF-SIMS. **(a-c)** Depth projections of ToF-SIMS ion counts from two 85-88% Br $n = 2$ HA-FA-Pb-I/Br microplates: monatomic Br ions ($^{79}Br^-$ & $^{81}Br^-$) **(a)**, I^- **(b)**, and dibromide cluster species [$^{81}Br_2^-$ & $(^{79}Br^{81}Br)^-$] **(c)**. **(d-f)** Depth profiles for each halide signal corresponding to the highlighted regions in (a-c).

Optical and Widefield Photoluminescence Microscopy

An Olympus BX51M widefield optical microscope configured in a reflective geometry with a CMOS RGB camera (ThorLabs Kiralux CS895CU) at the trinocular head was used to collect microscope images. Bright field optical images were collected under episcopic illumination from a tungsten halogen lamp. For true-color PL images, oblique UV illumination came from an externally mounted 365 nm LED flashlight equipped with a 400 nm shortpass filter. Residual violet illumination from the LED was filtered using a 427 nm longpass filter placed along the optic axis, except for $n = 1$ samples, where ~410 nm PL emission was anticipated. Irradiance of 365 nm light at the image plane was measured to be 1-4 mW/cm^2 using a Si photodiode (ThorLabs S120VC).

PL images were contrast-adjusted to remove background light and denoised via two passes of 3×3 median filters.

Confocal Photoluminescence Microscopy

Hyperspectral PL maps were collected using a Horiba LabRAM HR Evolution confocal Raman/PL spectrometer under CW excitation from a 405 nm laser diode. The excitation beam was focused by a microscope objective (Olympus LMPlanFl 50x, Plan Fluorite, NA 0.50) to a 2.6 μm spot (FWHM, Gaussian fit) with an irradiance of 9.4 W/cm^2. For mapping, the sample was rasterized using a motorized XYZ stage with <1 μm precision. Short exposures of 400 ms per x-y point were used to minimize light exposure and photoinduced phase separation. The collected light was filtered of the excitation light with a 405±5 nm notch filter and sent through a 100 μm pinhole into a spectrograph, where it was dispersed by a 300 grooves/mm grating onto a CCD array (Horiba Synapse+ BIDD).

Low Excitation Power Photoluminescence Spectroscopy

PL spectra were collected under low excitation power using a custom-built hyperspectral microscope (see diagram in Figure A1.2). A 375 nm pulsed laser diode (Horiba DeltaDiode DD375L, 80 MHz rep. rate, 50 ps pulse duration) was defocused with a biconvex lens and condensed onto the sample through a microscope objective (Olympus UMPlanFl 5x, Plan Fluorite, NA 0.15). The defocused spot (325 μm FWHM, Gaussian fit) had an irradiance of 20 μW/cm^2. The epi-directional fluorescence was isolated from the excitation light using a 400 nm longpass filter before being imaged with an infinity-corrected tube lens. The magnified image was sent through a ~50 μm slit into a spectrograph (Princeton Instruments Acton 2300i) so that a thin vertical slice of the image, corresponding to ~10 um width in the sample plane, was transmitted

for spectral analysis. The spectrometer spectrally dispersed the thin axis with a 150 grooves/mm grating onto a sCMOS camera (Andor Neo) to produce a spectral mapping of a y-slice of the sample.

Hot pixels/spikes (defined here as beyond the 99.5th percentile of pixel intensities) were removed from each camera frame. Background light was subtracted using dark regions of each image. Spectra were integrated along the y-axis to get a spatially averaged PL spectrum. The spectra were then smoothed using a 1st order Savitzky–Golay filter with a 31-point window corresponding to ~4.2 nm bandwidth.

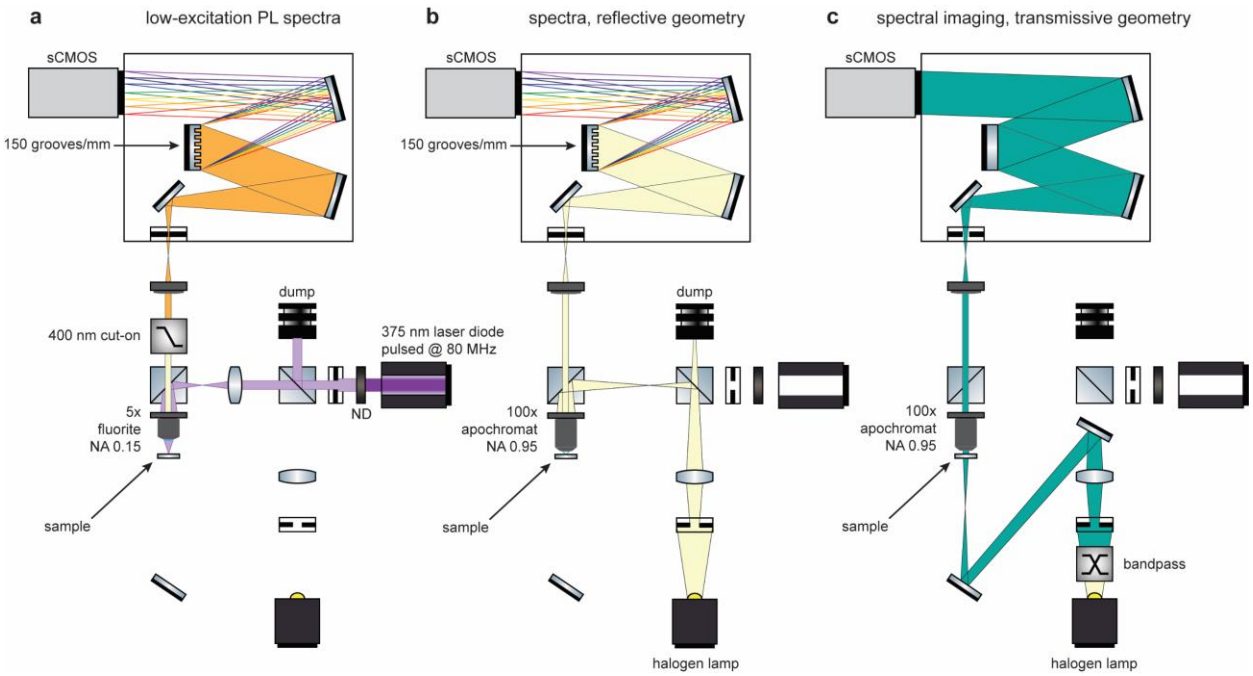

Figure A1.2. Optical diagrams of the custom-built hyperspectral microscope as configured for the spectroscopy experiments described in Experimental Methods. **(a-c)** Modular steps illustrating the various hyperspectral microscope configurations used throughout the work: configuration for low-excitation power PL with a defocused spot from a 375 nm laser diode **(a)**, a micro-reflectance sample geometry with the spectrograph configured for spectrum acquisition

(b), a micro-transmittance sample geometry with incident light and the spectrograph configured for spectral imaging **(c)**. Some graphics in the diagrams were adapted from ComponentLibrary by Alexander Franzen (licensed under CC BY-NC 3.0).[4]

Photostability Experiment

Excitation conditions for widefield PL microscopy were emulated by defocusing the beam from a 405 nm CW laser diode with a biconvex lens and condensing it onto the sample through a microscope objective (Olympus UMPlanFl 20x, Plan Fluorite, NA 0.46). The defocused spot (110 μm FWHM) had a mean irradiance of 3.8 mW/cm^2 in the region from which PL was collected, which was at the high end of the range measured during widefield PL imaging. To emulate confocal PL conditions, a tightly focused 405 nm spot (0.9 μm FWHM, Gaussian fit) was adjusted in power to have an irradiance of 9.7 W/cm^2.

Fluorescence spectra were collected in the same fashion as low excitation power PL spectra, but they were captured in rapid succession by the camera for time resolution. Spectra are y-binned averages of each frame captured by the camera. Frame-to-frame variance in readout noise was subtracted from each spectrum using the average intensity from a feature-free wavelength range (450-500 nm) as reference. Video of photoinduced phase separation was captured under excitation from the defocused spot described above. The magnified image passed through a 580±10 nm bandpass filter before being relayed onto the camera using a mirror on the spectrograph grating turret.

Micro-transmittance and Micro-reflectance Measurements

Perovskite microplate samples for micro-transmittance and micro-reflectance measurements were dry transferred onto fused silica microscope cover slips. Micro-absorbance

and micro-reflectance measurements were performed using a custom-built hyperspectral microscope (see diagrams in Figure A1.2). Light from a tungsten halogen lamp (Fiber-Lite MI150) was either transmitted through the sample along the optic axis or condensed onto the sample through a microscope objective (Olympus MPlan Apo N 100x, Plan Apochromat, NA 0.95) for absorbance or reflectance measurements, respectively. Reflected or transmitted light was collected by the objective and imaged through an infinity-corrected tube lens. Spectra were collected in the same fashion as low power PL, but without any spectral filtering. The vertical slice of the magnified image sent through the slit corresponded to ~500 nm width in the sample plane. For spectral images, light from the lamp was filtered using bandpass filters centered at wavelengths of interest (±10 nm) before being relayed to the sample as described above. The imaged light was reflected onto the camera using a mirror on the spectrograph grating turret. Spectra and images from uncovered regions of substrate were used as a reference intensity (I_0) to compute absorbance and reflectance. Reflectance of the substrate was calibrated to the total incident intensity by comparing with reflectance signals from a UV-enhanced aluminum mirror (ThorLabs -F01).

Dark counts were subtracted from all camera frames using internal references for dark signal. For spectra, average counts at ~385 nm (column of pixels at the blue edge of the frame) were assumed to measure dark counts due to the lossiness of the optical system below 400 nm. For images, edges of the image blocked by the slit at the spectrograph entrance were assumed to measure dark counts. Pixels with negative values following dark count subtraction were set to zero.

The frames were then adjusted for variations in exposure time and incident light intensity. The working assumption was that background regions should have a mean transmittance of 1 or a mean reflectance equivalent to the reflectance of the substrate. Sample frames generally had unoccupied substrate regions to serve as internal references for background (I_0). The mean

intensities of background regions in sample frames were compared to the corresponding regions of the reference frame to determine a correction coefficient c for the reference signal. The final values for reflectance/transmittance were computed using the adjusted formula: R or T = I/(cI_0). Pixels with undefined values after computing R or T were set to 1. Spectra are y-binned averages of frames in the region occupied by the sample.

A1.2. Supplementary Figures

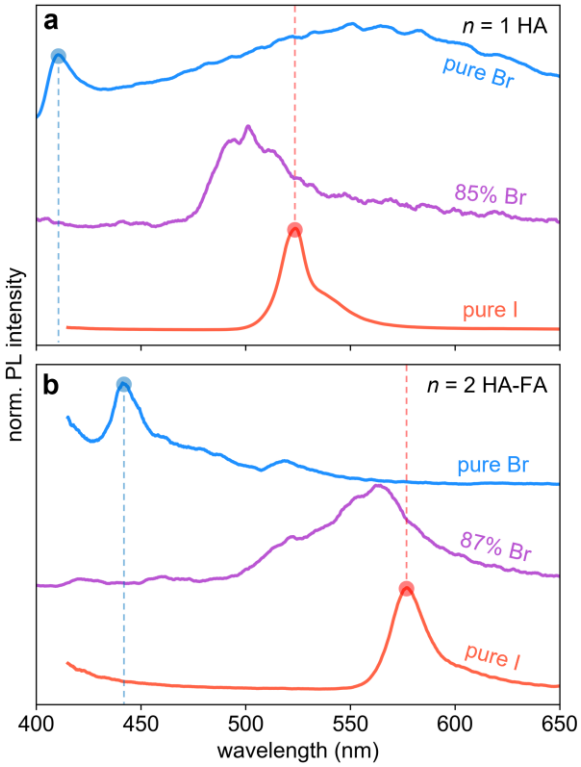

Figure A1.3. Steady state PL spectra for n = 1 HA and n = 2 HA-FA phases shown in this work. **(a,b)** PL obtained from mixed-halide n = 1 HA **(a)** and n = 2 HA-FA **(b)** microplates at the crossing points of their I/Br phase systems, compared to steady state PL spectra from their phase-pure analogues. The PL for the mixed-halides was collected under low excitation power (20 μW/cm^2 for n = 1 HA, 80 μW/cm^2 for n = 2 HA-FA).

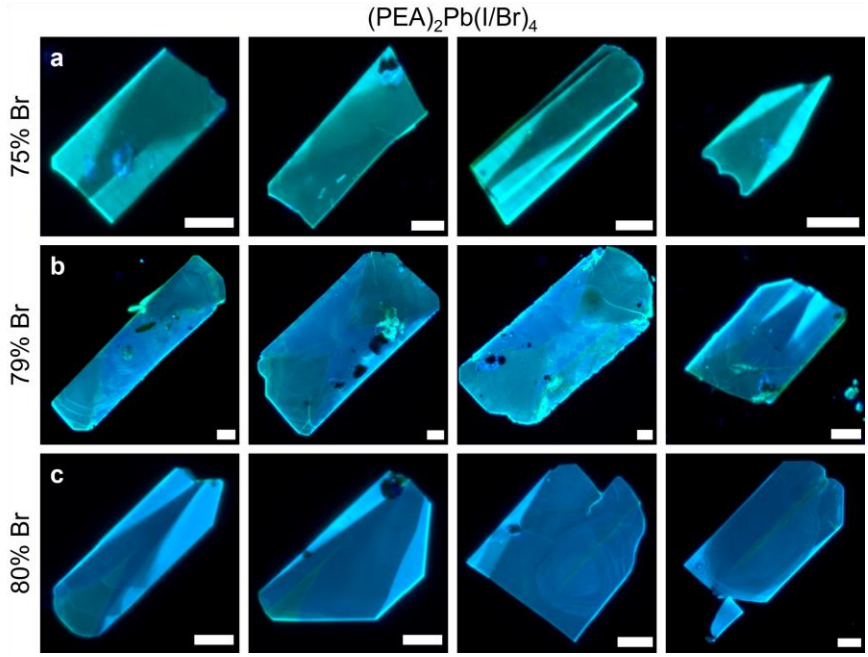

Figure A1.4. Consistency of PL appearance in mixed-halide $n = 1$ PEA microplates around the crossover point of the I/Br phase system. **(a-c)** PL micrographs of sets of four mixed I/Br $n = 1$ microplates precipitated from the same HI/HBr precursor solution containing: 75% Br **(a)**, 79% Br **(b)**, and 80% Br **(c)**. All scale bars are 10 μm.

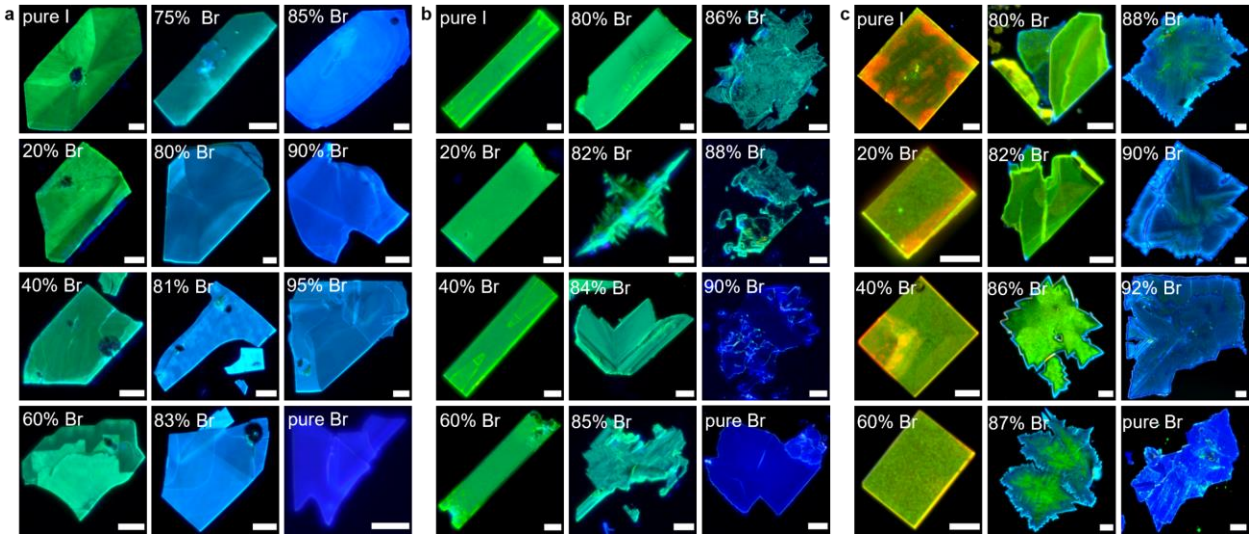

Figure A1.5. PL images of additional microplates from the mixed I/Br phase systems of the three parent phases in the main text. **(a)** $n = 1$ PEA, **(b)** $n = 1$ HA, **(c)** $n = 2$ HA-FA. All scale bars are

10 μm. We are not sure as to why the n = 2 HA-FA microplates appear to show bluer edges, but we hypothesize that it is either a consequence of growth habit for the n = 2 phases, or a bias of light emission at the edges to wider bandgap phases. In the growth habit case, it could be that the I-rich phases have a higher propensity to nucleate in the concentration conditions used in this work, forming a nucleation site off which the Br-rich phases could grow. For light emission bias, it could be that blue light is attenuated by I-rich phases toward the core of the microplate, but toward the edges it can be scattered and escape the microplates.

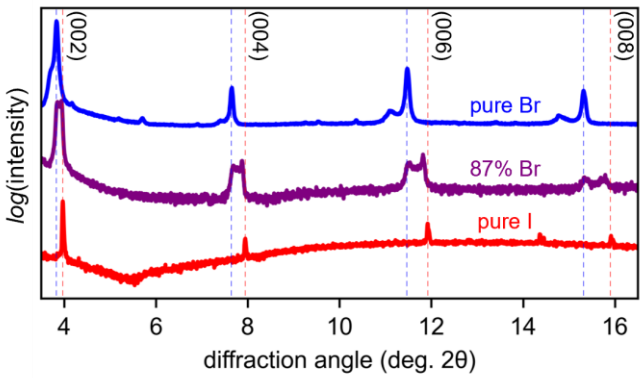

Figure A1.6. Extended range XRD pattern for a mixed-halide n = 2 HA-FA sample at the crossing point of the I/Br phase system, compared to the corresponding patterns of phase-pure analogues.

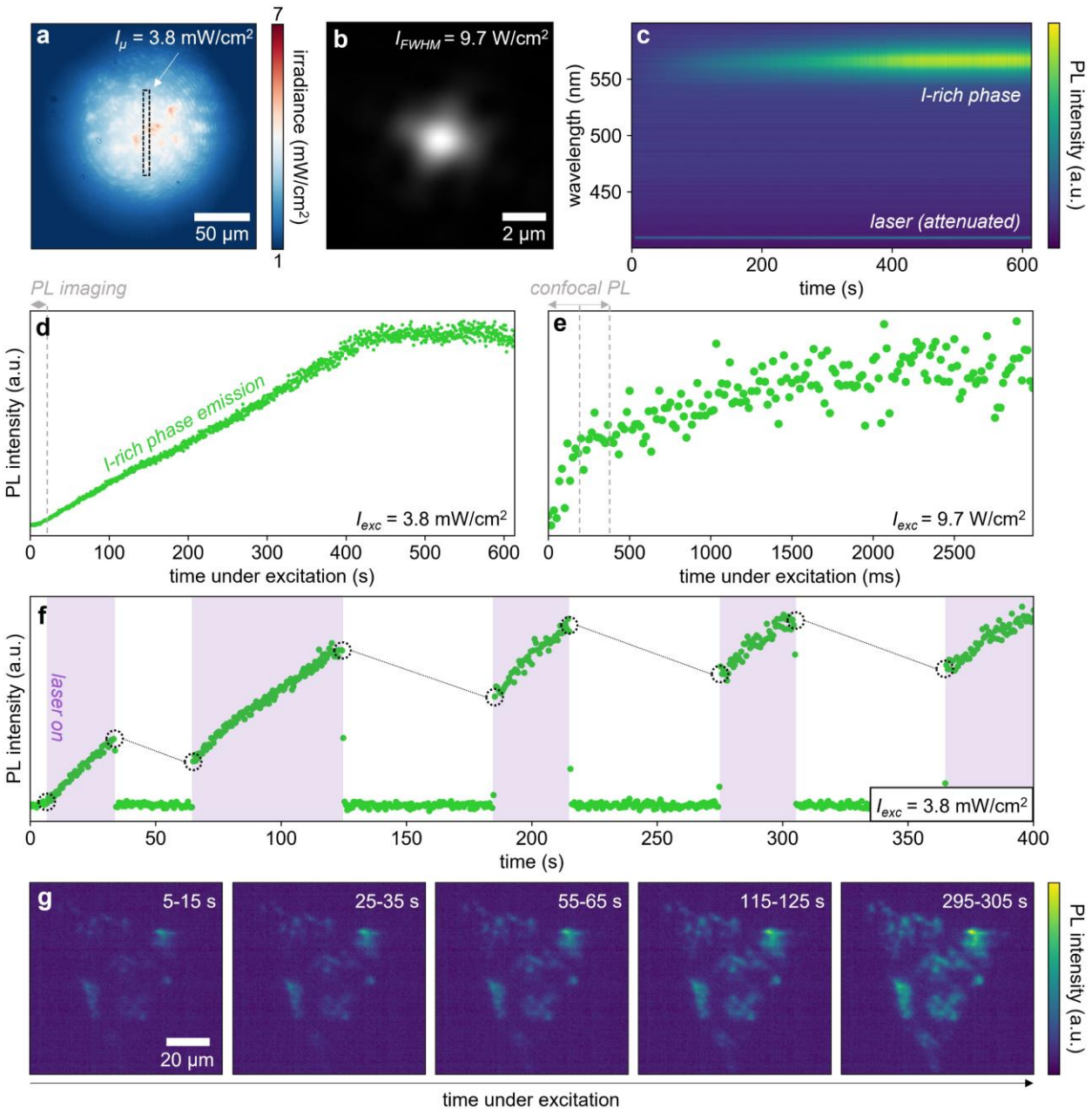

Figure A1.7. Photostability of mixed-halide $n = 2$ HA-FA microplates prepared from an 87% Br precursor solution (at the crossover point of the I/Br phase system). **(a,b)** Excitation spots (405 nm, CW) used for the photostability experiments: a diffuse spot calibrated to the irradiance range used for optical PL imaging **(a)**, a 50× focused spot calibrated to the irradiance range used for confocal PL mapping **(b)**. The boxed region in (a) is the area from which PL was measured and the mean irradiance was computed. **(c)** Temporal evolution of the PL spectrum from a single 87%

Br n = 2 HA-FA microplate under continuous excitation from the defocused spot in (a). **(d,e)** Integrated PL intensity of the I-rich peak identified in (c) under continuous excitation from the defocused spot emulating PL imaging conditions **(d)** and the focused spot emulating confocal PL conditions **(e)**. The dashed lines mark the longest exposure times necessary to collect the data shown throughout this work. Confocal PL data is an average of two sequential 200 ms exposures, indicated by the two dashed lines in (e). **(f)** Integrated PL intensity of the I-rich peak under repeated on-off exposure to PL imaging conditions, demonstrating the timescale for reversibility of the phase separation. Regions highlighted in purple indicate times during which the sample was exposed to 405 nm light. **(g)** Averages of video frames tracking PL emission of I-rich domains over time in a single mixed-halide microplate under the diffuse 405 nm excitation spot. Separate microplates were used for each photostability measurement to avoid convoluting results.

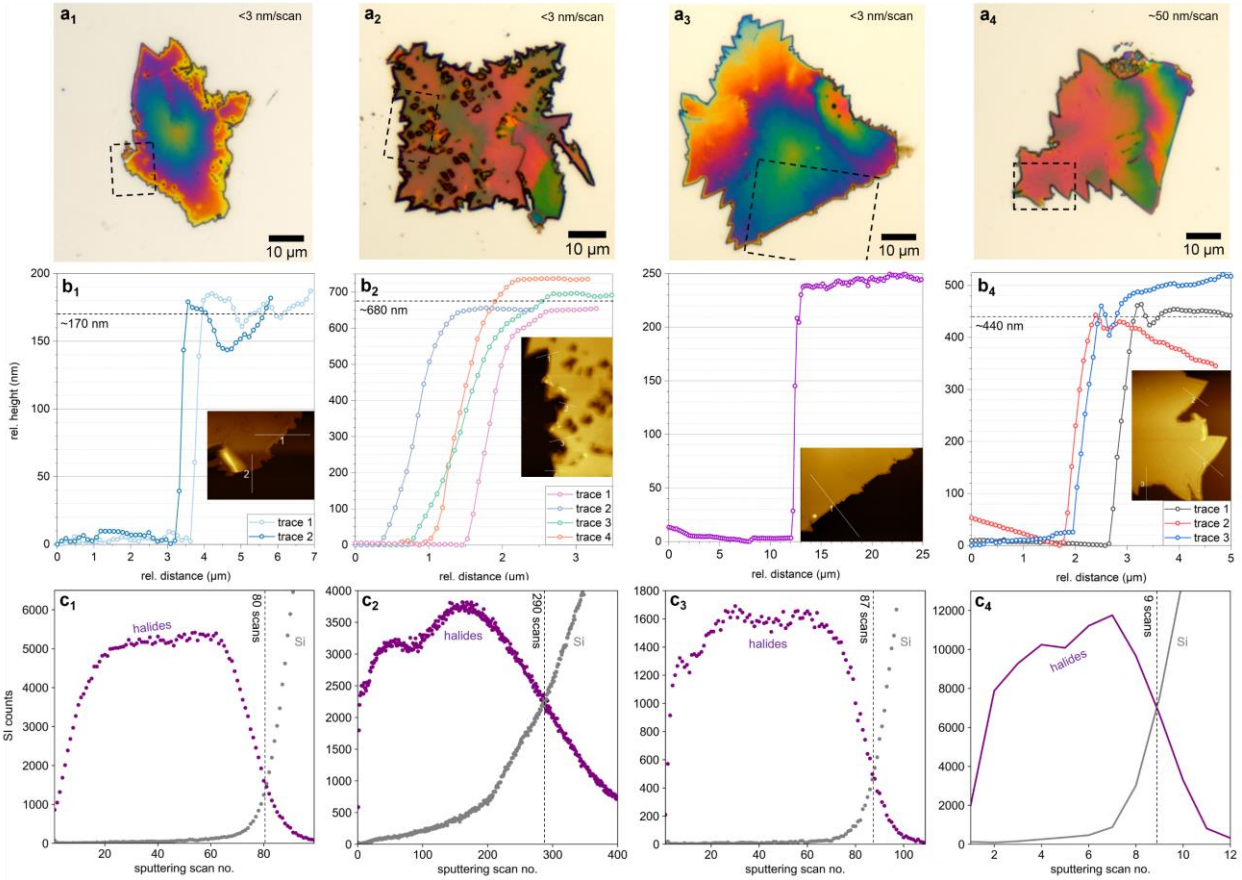

Figure A1.8. Height calibration using AFM topography imaging on the four microplate samples (1 to 4) that were later examined by ToF-SIMS. **(a)** Optical images of mixed-halide $n = 2$ HA-FA-Pb-I/Br microplates precipitated from ~85-88% Br precursor solutions, which were analyzed via ToF-SIMS. The dashed boxes indicate where topography was measured via AFM. **(b)** AFM height profiles corresponding to the lines in the inset AFM topography images. **(c)** ToF-SIMS sputtering profiles from the centers of the microplates in (a). Total halide ion counts (I+Br) were treated as a proxy for the presence of perovskite. Comparison of the sputtering depth in the SIMS experiments with the actual heights determined by AFM allows the determination of absolute height information in the SIMS results.

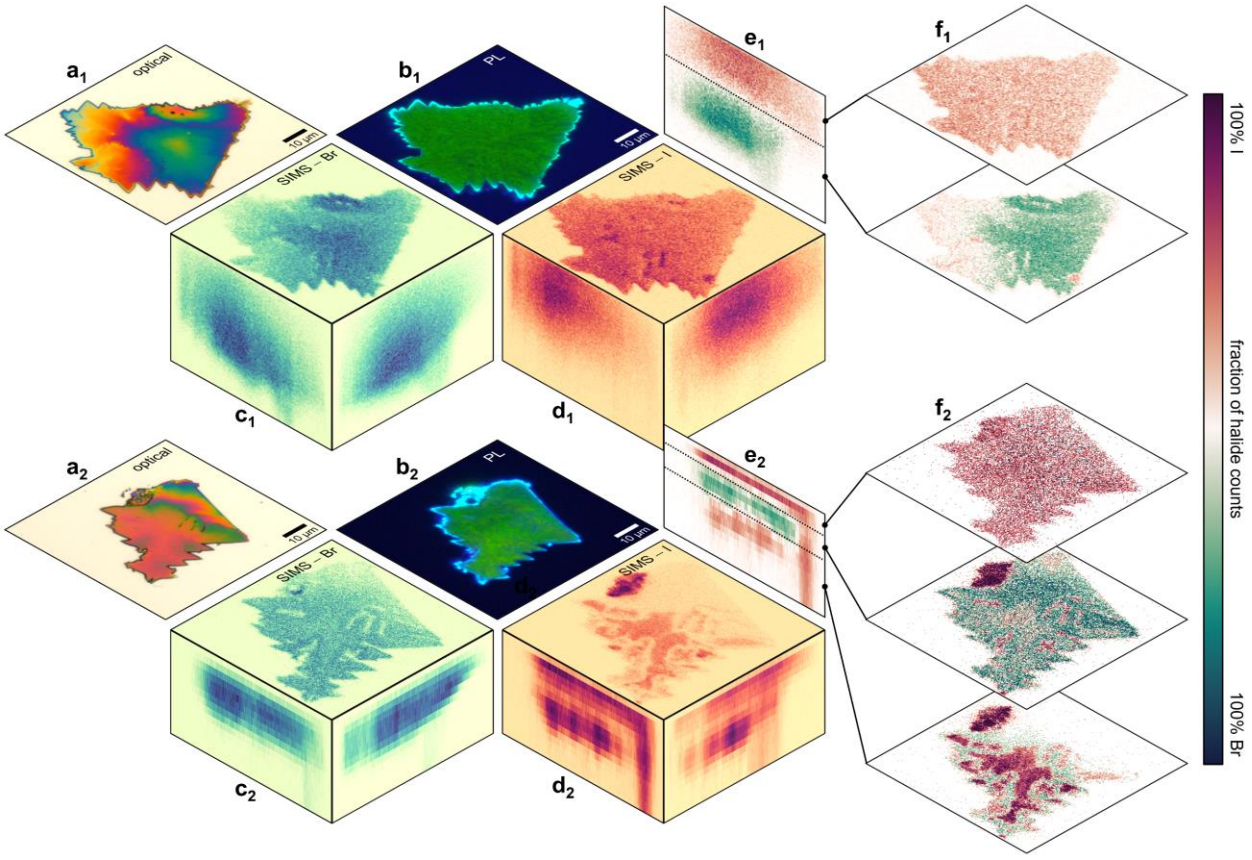

Figure A1.9. ToF-SIMS data for the two additional mixed-halide $n = 2$ HA-FA-Pb-I/Br microplates analyzed (1 and 2). For each microplate, **(a)** Contrast-enhanced optical microscope

images and **(b)** the corresponding true-color PL images collected under minimal light exposure (<5 mW/cm^2, <30s exposure) of $n = 2$ HA-FA microplates grown at the crossover point of the I/Br phase system. All scale bars are 10 µm. **(c, d)** Sums along axes of ToF-SIMS halide counts for bromide **(c)** and iodide **(d)**. Depth axis is not to-scale with x-y. **(e)** Relative I/Br proportion of total halide signal of a depth cross-section of the microplates depicted in (c) & (d). The dashed traces in (d) are the regions from which the cross-sections were extracted. **(f)** Relative I/Br proportion of total halide signal from depth sections of the microplates depicted in (c) & (d). The dashed lines in (e) partition the depth sections imaged in (f).

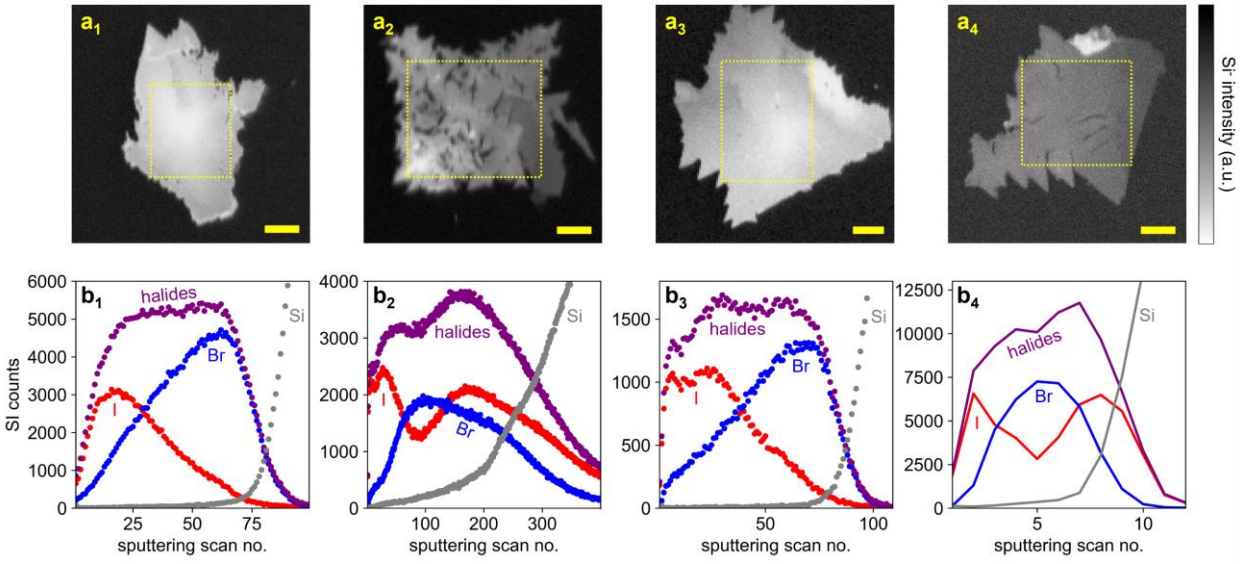

Figure A1.10. ToF-SIMS sputtering profiles of halides in the four microplates of the mixed-halide $n = 2$ HA-FA microplates near the crossover point of the I/Br phase diagram. **(a)** ToF-SIMS images of Si^- (substrate) counts for each microplate analyzed. **(b)** Sputtering profiles of iodide and bromide ions as well as the total halide counts from regions of sample indicated by the dashed boxes in (a). Scale bars are 10 µm.

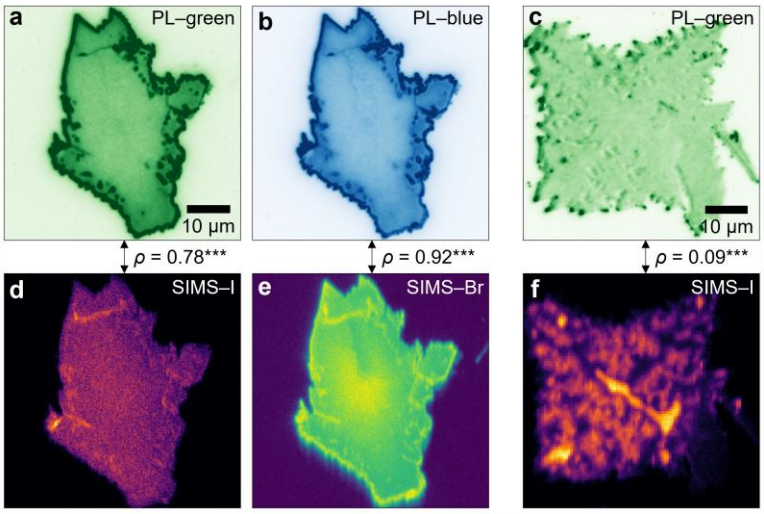

Figure A1.11. Statistical comparison of PL and ToF-SIMS data from common mixed-halide $n = 2$ HA-FA microplates. **(a-c)** Green and blue subpixel intensities from PL microscope images of the microplates analyzed via SIMS in Figure 3 of the main text. **(d-f)** SIMS halide maps summed along the depth axis for each microplate shown in Figure 3. *** indicates $p < 0.001$.

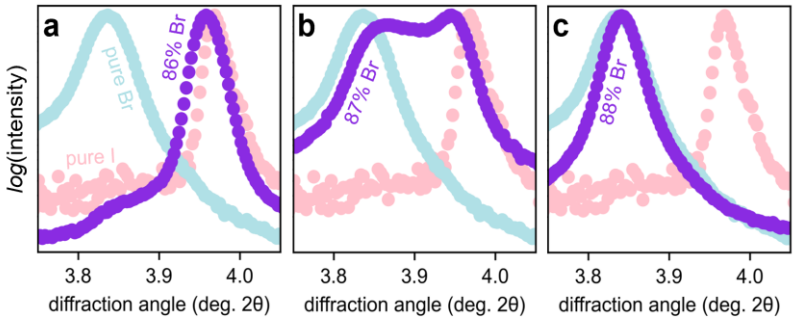

Figure A1.12. Key regions of the XRD patterns collected prior to light exposure of the mixed-halide $n = 2$ HA-FA microplate samples studied via micro-transmittance, micro-reflectance, and spectral imaging: 86% Br **(a)**, 87% Br **(a)**, and 88% Br **(a)**.

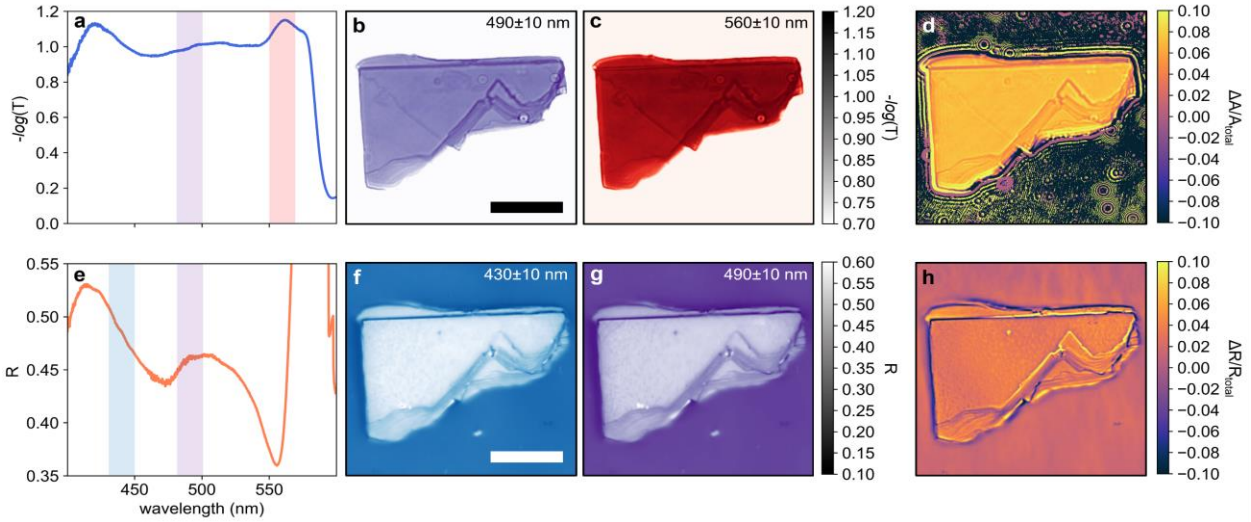

Figure A1.13. Spectral imaging of single-halide pure n = 2 HA-FA microplates. **(a, e)** Micro-transmittance **(a)** and micro-reflectance **(e)** spectra from a pure-I n = 2 HA-FA microplate. **(b, c, f, g)** Spectral images of transmittance **(b, c)** and reflectance **(f, g)** of a single pure-I microplate with varying thickness at spectral ranges highlighted in (a,e). Scale bars are 10 μm. **(d, h)** Difference in -*log*(T) **(d)** and reflectance **(h)** between the two spectral ranges imaged in (b, c) & (f, g), normalized to total signal from both ranges. Note the narrow range of the colormap scale.

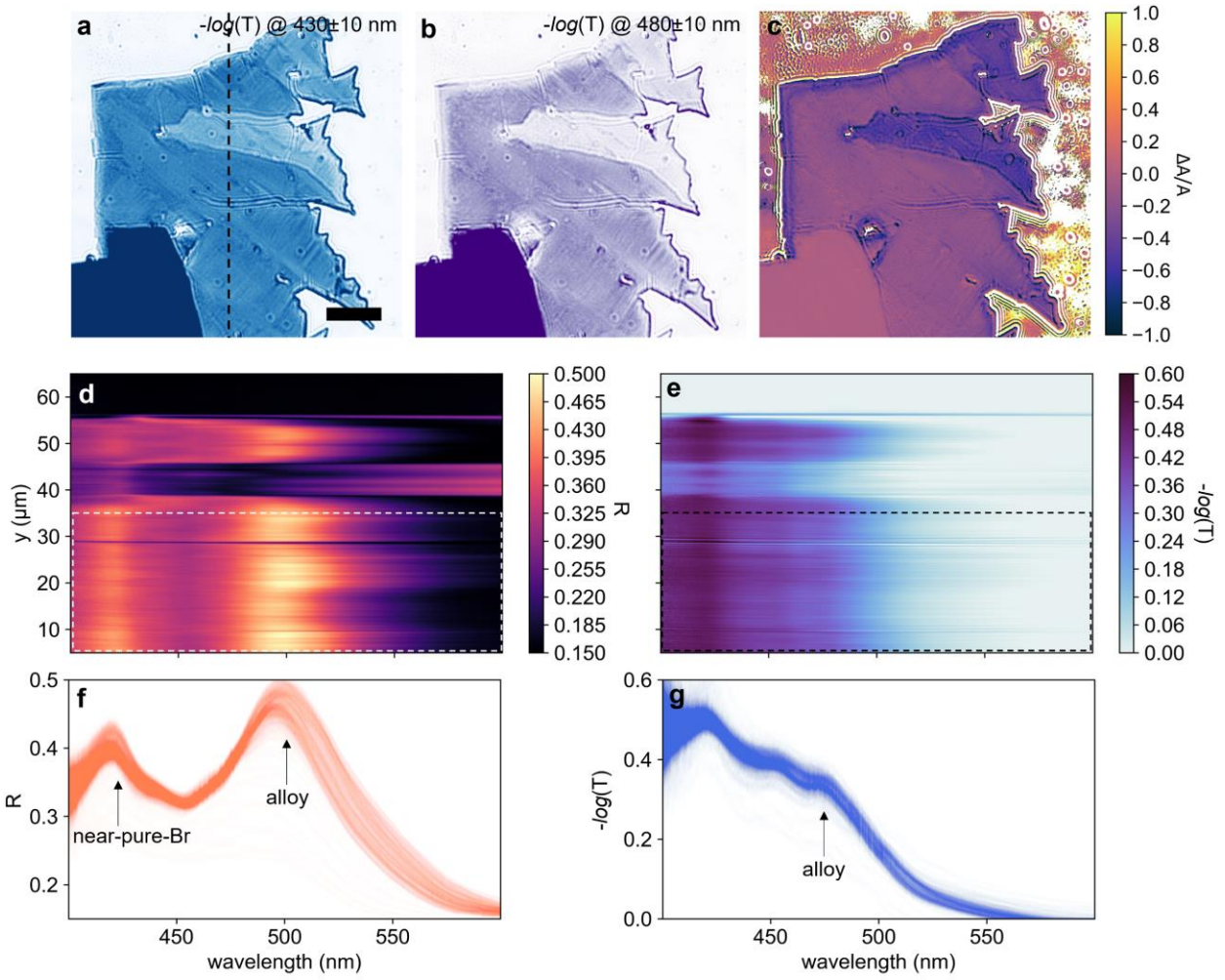

Figure A1.14. Example of layer-to-layer heterogeneity manifesting as coexisting spectral features in an 88% Br n = 2 HA-FA microplate. **(a-c)** Transmittance images at key spectral ranges **(a, b)** for n = 2 HA-FA halide phases and relative -*log*(T) between the two wavelength ranges **(c)** in a single microplate. Scale bar is 10 μm. **(d, e)** Hyperspectral profiles of reflectance **(d)** and transmittance **(e)** across a y-slice of the microplate along the dashed line in (a). **(f,g)** All reflectance **(f)** and transmittance **(g)** spectra decomposed from the boxed regions of the hyperspectral profiles in (d) and (e).

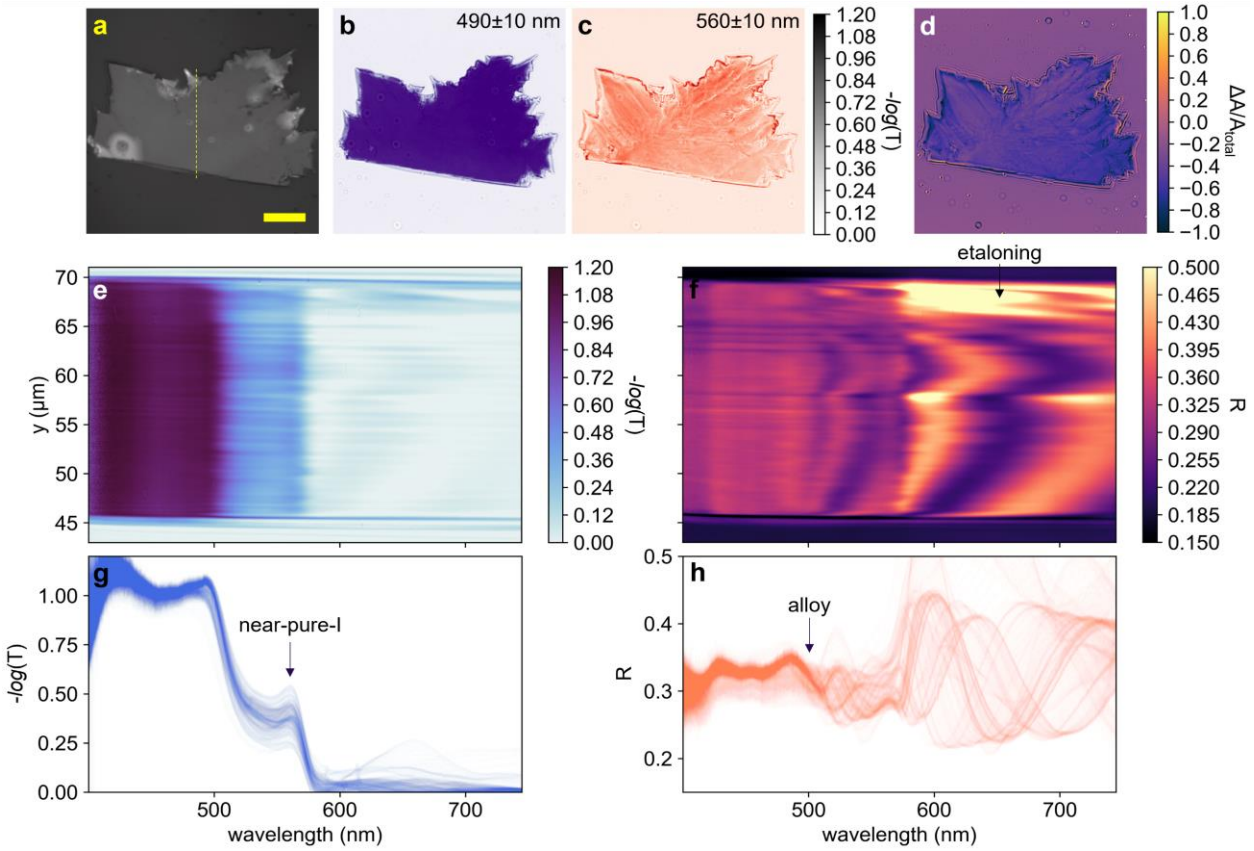

Figure A1.15. Example of etaloning in a mixed-halide $n = 2$ HA-FA microplate at the crossover point of the I/Br phase system. **(a)** Reflective geometry image of an 87% Br $n = 2$ HA-FA microplate under broadband illumination. **(b-d)** Transmittance images at key spectral ranges **(b, c)** and relative *-log*(T) between the two wavelength ranges **(d)** for $n = 2$ HA-FA halide phases. Scale bar is 10 μm. **(e, f)** Hyperspectral profiles of transmittance **(e)** and reflectance **(f)** across a y-slice of the microplate along the dashed line in (a). **(g,h)** All transmittance **(g)** and reflectance **(h)** spectra decomposed from the hyperspectral profiles in (e) and (f).

A1.3. References

(1) Pan, D.; Fu, Y.; Spitha, N.; Zhao, Y.; Roy, C. R.; Morrow, D. J.; Kohler, D. D.; Wright, J. C.; Jin, S. Deterministic Fabrication of Arbitrary Vertical Heterostructures of Two-Dimensional Ruddlesden–Popper Halide Perovskites. *Nat. Nanotechnol.* **2021**, *16*, 159-165.

(2) Roy, C. R.; Pan, D.; Wang, Y.; Hautzinger, M. P.; Zhao, Y.; Wright, J. C.; Zhu, Z.; Jin, S. Anion Exchange of Ruddlesden–Popper Lead Halide Perovskites Produces Stable Lateral Heterostructures. *J. Am. Chem. Soc.* **2021**, *143*, 5212–5221.

(3) Scholder, O. *pySPM.* https://github.com/scholi/pySPM (accessed 2022-07-01, DOI: 10.5281/zenodo.2650457)

(4) Franzen, A. *ComponentLibrary*. http://www.gwoptics.org/ComponentLibrary/ (accessed 2022-07-01)

Appendix 2. Supplementary Information for Chapter 3

A2.1. Experimental Methods

Chemicals and Materials

All chemicals were used as purchased without further purification. Lead(II) iodide (PbI_2, 99.999%), lead(II) acetate trihydrate ($Pb(CH_3COO)_2 \cdot 3\ H_2O$, 99%), and hypophosphorous acid solution (H_3PO_2, 50 wt. % in H_2O) were purchased from Sigma Aldrich. Concentrated hydrobromic acid (HBr, 48 wt. % in H_2O), concentrated hydroiodic acid (HI, 55-58 wt. % in H_2O), and lead(II) bromide ($PbBr_2$, 98+%) were purchased from Alfa Aesar. Methylammonium iodide (MAI), formamidinium iodide (FAI), formamidinum bromide (FABr), guanidinium iodide (GAI), phenethylammonium iodide (PEAI), *n*-butylammonium iodide (BAI), *n*-hexylammonium iodide (HAI), and *n*-hexylammonium bromide (HABr) were purchased from GreatCell Solar. Isopropanol (IPA, 99%) was purchased from Fisher Scientific. 5 mil fluorinated ethylene propylene (FEP) film was wiped with IPA prior to use in synthesis. Silicon substrates [n-type, (111)] with 100 nm native oxide were cleaned with methanol using delicate task wipes prior to use in synthesis.

Aqueous Droplet Growth of RPP Microplates

All synthesis was carried out in ambient conditions. 1 M stock precursor solutions of PbI_2 and the various organoammonium iodide salts were prepared by dissolving the precursor salts in a 10:1 (by volume) solution of HI and H_3PO_2. To synthesize a given RPP compositional target $(LA)_2(A)_{n-1}Pb_nI_{3n+1}$, the 1 M HI solutions of (LA)I, AI, and PbI_2 were mixed in a specific ratio (see Table A2.1) and heated in a scintillation vial to ~110 °C until all precipitate was dissolved. They were then transferred to a polypropylene centrifuge tube and cooled to room temperature, and then precisely heated to the appropriate supersaturation temperature in a PCR thermal cycler (Abbott

LCx) (see Table A2.1) and held there for >1 h to equilibrate. Meanwhile, a glass microscope slide was placed bridged over a glass petri dish to make the stage and the catch pan for the reaction, respectively (see Figure A2.1a). A small (~1 cm × 2 cm) strip of FEP film was placed level on the reaction stage, which was then placed under a reflective optical microscope (Olympus BX51) with a high working distance objective lens and brought into focus. The equilibrated stock solution was removed from the thermal cycler and a large drop of the reaction mixture (without any solids) was pipetted out within 30 s and carefully dispensed onto the center of the FEP substrate at room temperature (Figure A2.1a). The growth of the microplates was monitored live using the microscope. Once the desired average crystal size was reached, usually 50-100 μm along one side, the FEP substrate was tilted over the edge of the slide with tweezers, allowing the large droplet to roll off the hydrophobic FEP substrate into the petri dish. The substrate was then quickly placed under a moderate flow of nitrogen gas for ~10 s to blow off remaining solution droplets, leaving a dry substrate with a population of tens to hundreds of RPP microplates. The same approach was taken to synthesize $(HA)_2(FA)Pb_2Br_7$ with the bromide analogues of each compound in a 10:1 (by volume) solution of HBr and H_3PO_2. The phase purity of the samples was verified using powder XRD and confocal PL measurements of a large population of the microplates in a sample (Figures S11 & S12).

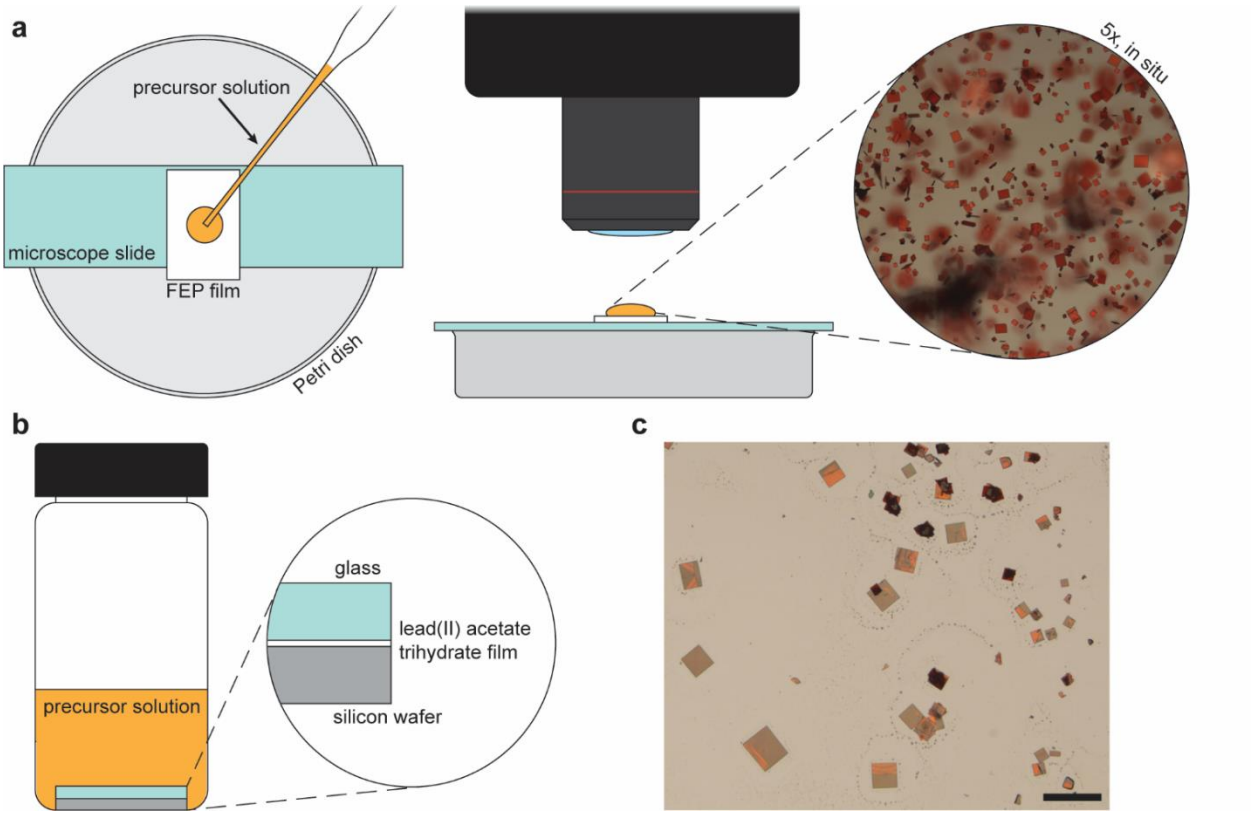

Figure A2.1. Synthesis methods for RPP microplates. **(a)** Scheme of the reaction setup for the aqueous droplet growth method. Inset image on the right shows an optical image of the directly monitored synthesis of a sample of $(HA)_2(FA)Pb_2I_7$ microplates. **(b)** Schematic illustration of the reaction setup for the solution transport growth method in isopropanol (IPA) solution. **(c)** Optical micrograph of the $(HA)_2(FA)Pb_2I_7$ microplates synthesized via solution transport prior to washing with IPA. Scale bar is 500 µm.

Table A2.1. Parameters for the synthesis of halide perovskite microplates and microcrystals via directly monitored aqueous droplet growth.

Compound	[LAI] (mM)	[AI] (mM)	[PbI_2] (mM)	V (µL)	T (°C)
$(C_6H_{13}NH_3)_2PbI_4$	222	-	450	200	35
$(C_6H_{13}NH_3)_2(CH_3NH_3)Pb_2I_7$	150	250	500	300	40
$(C_6H_{13}NH_3)_2(CH_3NH_3)_2Pb_3I_{10}$	83	417	500	300	40
$(C_6H_{13}NH_3)_2(CH_3NH_3)_3Pb_4I_{13}$	33	467	500	300	40

$(C_4H_9NH_3)_2PbI_4$	250	-	500	300	40
$(C_8H_9NH_3)_2PbI_4$	50	-	500	300	40
$(C_6H_{13}NH_3)_2(CH_5N_2)Pb_2I_7$	50	125	450	200	38
$(C_6H_{13}NH_3)_2(CH_6N_3)Pb_2I_7$	80	320	500	300	40
$(C_6H_{13}NH_3)_2(CH_5N_2)Pb_2Br_7$	62	188	500	300	40
$(CH_3NH_3)PbI_3$	-	600	500	300	40

Solution Transport Growth of $(HA)_2(FA)Pb_2I_7$ Microplates

An organoammonium precursor mixture of 10 mM HAI and 295 mM FAI in IPA was prepared quantitatively with volumetric glassware. Following the general approach previously reported,[1] a lead acetate film was prepared by casting a few drops of a methanol solution of 100 mg/mL $Pb(CH_3COO)_2 \cdot 3\,H_2O$ across the surface of a 1 cm^2 glass microscope slide and drying it on a hot plate at 80 °C for about 30 min. In a 4-dram (~15 mL) glass vial, a 1 cm^2 piece of Si/SiO_2 substrate was placed with its polished side up into 2 mL of the precursor mixture. The lead acetate covered glass slide was then gently placed film side down onto the silicon substrate, such that the surface area in mutual contact was maximized (Figure A2.1b). They were then allowed to sit for 90 h at room temperature before being carefully and gently removed from the vials with tweezers. The silicon substrate was washed gently in an IPA bath and dried under a stream of nitrogen gas and repeated one more time to remove the organic precursor residue prior to storage (Figure A2.1c). The exchange behavior of $(HA)_2(FA)Pb_2I_7$ microplates prepared with this method is qualitatively similar to that of $(HA)_2(FA)Pb_2I_7$ microplates prepared via aqueous droplet growth (Figure A2.14).

Vapor-Solid Anion Exchange Reactions

The vapor-solid anion exchange reactions were performed by exposing a RPP sample in a reaction chamber at room temperature to a continuous flow of hydrogen bromide (HBr) vapor

made by bubbling nitrogen gas through a concentrated HBr solution (48 wt. %). As illustrated in Figure A2.2, the exchange reactor was assembled in a fume hood consisting of, in order of flow direction, a gas flow regulator, a gas washing bottle filled with 75 mL of concentrated HBr, a drying tube packed with 10 g of indicator-free 8 mesh Drierite® desiccant between two wads of glass wool, a coarse frit glass filtration funnel sealed with a stemmed rubber stopper (serving as a sample chamber), and a filtration flask containing saturated sodium bicarbonate solution and sealed with a stemmed rubber stopper. The entire apparatus was connected with Tygon® tubing and all glass fittings were sealed with silicone vacuum grease. The substrates covered with microplates of various RPPs were placed in the sample chamber and the anion exchange reaction was typically run at a nitrogen gas flow rate of 0.4 standard liters per minute (SLM) for the desired amount of time, with desiccant being replaced after every ~24 h of reaction time.

Preparation of Exfoliated Heterostructure Layers from Large $(HA)_2(FA)Pb_2I_7$ Crystals

The same $(HA)_2(FA)Pb_2I_7$ reaction mixture that was used for aqueous droplet growth was heated at 75 °C for 3 h before cooling to room temperature at 1 °C/h to promote the slow growth of large crystals. The resulting crystals were vacuum filtered, washed with ~ 5 mL of chilled diethyl ether and dried under vacuum overnight. The crystals were subjected to anion exchange for 24 h (see above) and then mechanically exfoliated using scotch tape. The exfoliation process was repeated a few times until the exfoliated crystal flakes appeared translucent under a microscope. The flakes were then transferred to a silicon substrate by lightly laminating the tape onto the substrate and slowly peeling off multiple times in sections.

Optical and (Confocal) Photoluminescence Microscopy

Optical micrographs were collected using an Olympus BX51 widefield microscope configured in a reflective geometry. Images were captured using Spot Insight 2 or ThorLabs Kiralux CS895CU CMOS cameras. Objective lens scales were calibrated prior to boundary propagation length measurements using the standard elements of a USAF 1951 resolution test target (ThorLabs). PL micrographs were collected using the same microscope under the direct illumination from an Infray pen light handheld 385 nm LED flashlight. A 427 nm longpass filter was placed along the optic axis of the microscope to filter out the incident light. PL images were captured using a Sony Alpha a6000 digital camera with long exposures (>5 s) and low gain (ISO100). Confocal PL maps and line scans were acquired using a Horiba Labram Aramis confocal Raman/photoluminescence microscope with a Horiba Synapse CCD detector and a motorized XYZ stage under 442 nm or 532 nm CW laser excitation. For line scans, an 1800 groove/mm grating was used. A 300 groove/mm grating was used for mapping acquisitions. The gratings were calibrated to the 520.7 cm^{-1} Raman line of silicon under excitation from a 532 nm CW laser. A 100× microscope objective was used for mapping acquisitions, with approximate spot sizes (FWHM) of 1 μm (442 nm) and 4 μm (532 nm).

Time-Resolved Photoluminescence Spectroscopy

Steady state and time-resolved PL measurements were performed using a custom-built TRPL microscope. The 800 nm fundamental of a mode-locked Ti:sapphire oscillator (Coherent Vitesse, 80 MHz rep. rate, 100 fs pulse duration) was frequency doubled to 400 nm using a crystal of barium borate (BBO) and focused onto the sample through a 100× microscope objective. The emitted light was then collected through the same objective and sent into a spectrograph (Princeton Instruments Acton SP2300i), where it was dispersed with a 150 g/mm grating onto a sCMOS camera (Andor Neo) for spectra, or an avalanche photodiode (IQD ID-100) coupled to a time-

correlated single photon counting module (Becker & Hickl SPC-130) for transients. All measurements were conducted at pulse fluence of 2.37 μJ/cm2.

Time-of-Flight Secondary Ion Mass Spectrometry

The $(HA)_2(FA)Pb_2I_7$ microplate samples used for ToF-SIMS analysis were grown directly on a n-type silicon substrate via the solution transport growth (to prevent charging during analysis) followed by the anion exchange reaction as described above. ToF-SIMS measurements were performed using a TOF-SIMS5 instrument (IONTOF GmbH, Münster, Germany) with dual beam non-interlaced mode depth profiling at the Environmental Molecular Sciences Laboratory (EMSL) of Pacific Northwest National Laboratory. A 2.0 keV Cs^+ beam was used as the sputtering beam and a 25 keV Bi^+ beam was used as the analysis beam for ion image collection. The Cs^+ sputtering beam (~140 nA) was scanned over a 200×200 μm^2 area. The Bi^+ beam was focused to be about 0.40 μm in diameter with a beam current of about 1.20 pA at a 20 kHz frequency. During image collection, the Bi^+ beam was scanned with 256×256 pixels over an area of 70×70 μm^2 at the Cs^+ sputter crater center. The non-interlaced mode was operated at 3.0 s sputtering time, 1.0 s pause time and 6.55 s data collection time (2 scans of 256×256 pixels). A low energy (10 eV) electron flood gun was used for charge compensation in all measurements. Data reconstruction was performed to get digital zoom-in ion maps and depth profiles of interesting ion species at desirable areas. The complete SIMS sputtering profiles for all species are shown in Figure A2.15.

Scanning Electron Microscopy and Energy Dispersive X-Ray Spectroscopy

Intact microplates imaged via SEM were directly grown on Si substrates via the solution transport growth. The heterostructure subjected to EDS analysis in Table 3.4i-j was from a large crystal grown from aqueous solution and exfoliated as described above. Scanning electron

micrographs were collected using a Carl Zeiss LEO Supra 55V field emission SEM at an accelerating voltage of 3 kV. EDS analysis was performed in the same SEM at an accelerating voltage of 25 kV and a working distance of 8 ± 0.1 mm, for which the Si drift EDS detector was calibrated. EDS maps were acquired with a signal continuously summated over a 600 s acquisition. For EDS line scans, 100-point lines were used and summated thrice per acquisition, with a dwell time of 0.5 s/point.

Other Structural Characterizations

Powder X-ray diffraction patterns were collected using a Bruker D8 Advance powder X-ray diffractometer with the Cu-K_α line. A knife edge was used to attenuate incident X-ray background at low diffraction angles. AFM topography measurements were performed using an Agilent Keysight 5500 atomic force microscope in tapping mode with a Bruker NCHV-A tip (spring constant: 40 N m^{-1}).

Optical Tracking of Heterostructure Phase Boundary Propagation

Two samples of $(HA)_2(FA)Pb_2I_7$ microplates on FEP films prepared via aqueous droplet growth were imaged immediately prior to the experiment under consistent exposure time and sensor gain. One sample was subjected to the exchange reaction while a control sample was left out in ambient environment. The samples were periodically imaged under the microscope at chosen time points. At certain time intervals, the samples were stored overnight between time points in a sealed desiccator in the dark. The microplates were imaged before and after overnight cycles to ensure no changes had occurred beyond the controlled reactions themselves. The boundary propagation distance was measured using ImageJ image analysis software by aligning image sequences of each individual microplate in time series. The junctions and edges are local

minima in pixel intensity, which are reliable gauges to track. The distances were measured in integer numbers of pixels with no sub-pixel interpolation, instead relying on the statistics of all edge measurements made in the sample to determine the measurement uncertainty. Each side of each quadrilateral microplate served as a measurement point, with measurement lines bisecting each microplate edge.

Temperature and Temporal Stability Experiments

A sample of n = 2 HA-FA-Pb-I/Br heterostructures and n = 2 HA-FA-Pb-I microplates inside a covered, desiccated glass Petri dish were placed inside a temperature-controlled oven at 50 °C for 12 h. The same process was performed on a second sample at 100 °C. A control sample in a desiccated container outside the oven was left in the dark under ambient environment while the test samples were in the oven. A sample of n = 2 HA-FA-Pb-I/Br heterostructures grown via aqueous droplet growth was left inside a sealed, desiccated polystyrene Petri dish for 116 days in the dark before being removed for imaging.

Photostability Experiment

Time-dependent confocal PL spectra were collected using a Horiba Labram Aramis confocal Raman/photoluminescence microscope. A freshly exfoliated layer of an n = 2 HA-FA-Pb-I/Br heterostructure (see above) was continuously excited with a 442 nm CW laser, which was passed through two different neutral density filters and focused onto the junction with a 50× objective lens. Irradiances were calculated using power measurements from a photodiode power meter (ThorLabs S120VC) and the spot sizes (FWHM) from microscope images taken during the experiment. The PL spectra were collected at 10 s (low irradiance) and 15 s (high irradiance)

intervals for 15 min each using an 1800 groove/mm grating. Each trial was done at separate spots on the same exfoliated heterostructure plate to avoid convolving the two outcomes.

Additional notes about the synthesis procedures and safety and equipment considerations

Hazards and damage risks associated with aqueous droplet growth

The hydroiodic acid (HI) precursor solutions used in the aqueous droplet synthesis of perovskite microplates are corrosive, toxic, and volatile when heated. Beyond the normal precautions to be taken during the solution-based synthesis of lead halide perovskites[2], it is suggested that additional measures be taken to protect the microscope from contamination and damage:

- Microscope objective lenses with working distances below 1 cm risk being damaged by HI fumes over repeated droplet syntheses. An inexpensive stereo microscope is ideal for this synthesis, but we have observed no damage to a 1 cm working distance objective lens after hundreds of droplet syntheses. A cover slip or plastic barrier between the lens and the sample may also suffice.

- The microscope should be cleaned with a lead cleaning solution or soapy water near the dispensation zone to avoid contaminating the microscope over repeated droplet syntheses.

Notes about the design and operation of a vapor-solid anion exchange reactor

The VSAE reactor need not be assembled in the exact manner described in the methods, but through optimizing the reactor, we identified some important attributes that should remain as essential components of any derivative of this type of apparatus:

- The main utility of the desiccant is preventing the formation of moisture droplets in the reaction chamber, not the complete removal of the water vapor (which is likely very difficult). Other chambers capable of preventing vapor accumulation and condensation can also work, such a large drying tower packed loosely with glass wool. If desiccant is chosen to attenuate the accumulation of moisture, Drierite® or similar $Ca(SO_4)$ desiccants should be used, because other common desiccants such as silica beads and molecular sieves can be destroyed by reacting with the HBr in the vapor.

- The reactor must be regularly cleaned to prevent the accumulation of moisture/condensation in the tubing, so it is valuable during extended reactions to have multiple sets of tubing available and ready to be swapped.

- An adequate seal through the entire apparatus with an inhibitor of flow through the outlet (i.e., a bubbler) is necessary to maintain positive pressure in the reactor. In our setup, the bubbler containing saturated sodium bicarbonate solution fulfilled this role. The sodium bicarbonate also scavenges the HBr or HI outgassed.

A2.2. Supplementary Figures

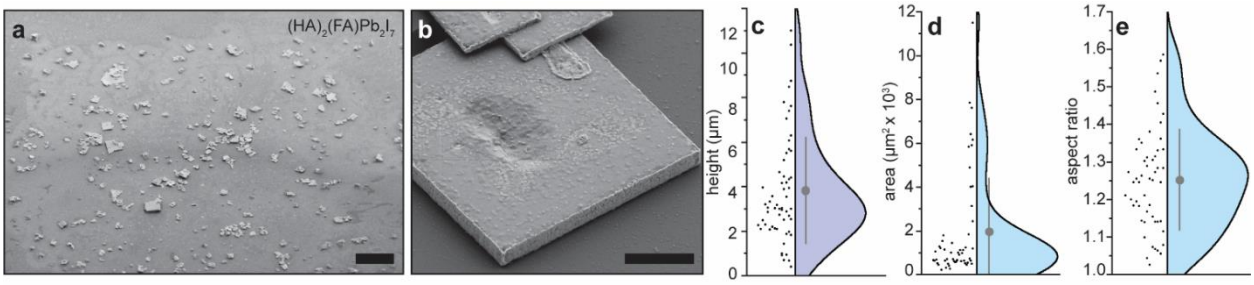

Figure A2.2. Morphology distribution of RPP microplates. **(a,b)** Low magnification tilted SEM images of $(HA)_2(FA)Pb_2I_7$ microplates grown on Si wafer via solution transport. Scale bars are 100 μm for a and 10 μm for b. **(c-e)** Half violin plots showing statistics for measurements of **(c)**

microplate heights of n = 2 HA-FA-Pb-I samples grown via solution transport, **(d)** microplate top face areas of a n = 2 HA-FA-Pb-I sample grown via aqueous droplet growth, **(e)** lateral aspect ratios for the same microplate samples as in d. The distribution curves are kernel density estimates. Large gray dots and bars represent the mean and standard deviation, respectively.

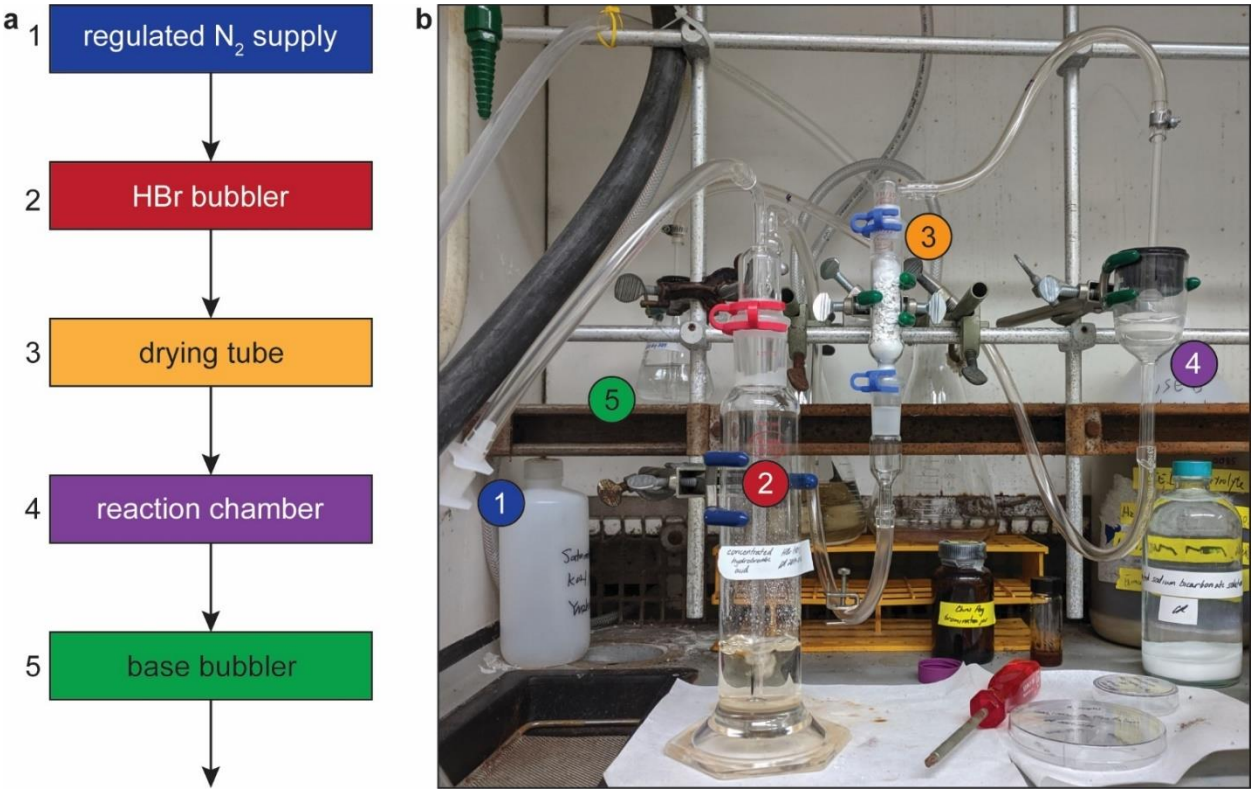

Figure A2.3. Illustration and photo of the vapor-solid anion exchange (VSAE) reactor. **(a)** Flow chart of the components of the VSAE reactor, ordered in flow direction of the carrier gas. **(b)** Photograph of the VSAE reactor during operation, with numbered labels corresponding to the order of the flow chart in a.

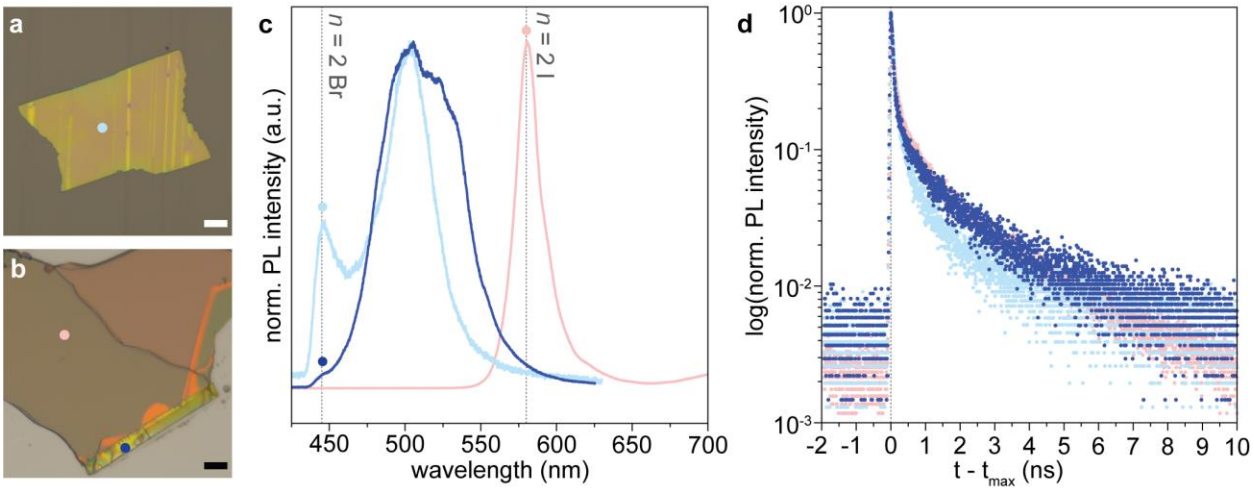

Figure A2.4. Comparison of the pure $(HA)_2(FA)Pb_2Br_7$ microplate directly synthesized and the converted $(HA)_2(FA)Pb_2Br_7$ phase in an anion-exchanged heterostructure. **(a,b)** Optical micrographs of **(a)** a microplate of $(HA)_2(FA)Pb_2Br_7$ directly synthesized via aqueous droplet growth and **(b)** an exfoliated layer of a $(HA)_2(FA)Pb_2I_7$—$(HA)_2(FA)Pb_2Br_7$ heterostructure prepared via anion exchange with HBr vapor. Scale bars are 10 μm. **(c)** PL spectra corresponding to the colored spots in panels a & b. The peak at ~500 nm is also present in the directly synthesized pure $(HA)_2(FA)Pb_2Br_7$ microplate sample, which is attributed to an emissive defect state. Note that the asymmetric blue shoulders of the 445 nm peaks are due to the cut-off wavelength of a long-pass filter used to attenuate the incident laser light. **(d)** TRPL transients at the spots marked in a & b and the peak wavelengths indicated with dots in c.

Table A2.2. Biexponential fitting parameters for the TRPL transients shown in Figure A2.4d using $I(t) = A_1 e^{-t/\tau_1} + A_2 e^{-t/\tau_2}$. The time range of 0-10 ns past peak intensity was used for fitting.

Sample	A_1	τ_1 (ns)	A_2	τ_2 (ns)	R^2
Directly Synthesized $(HA)_2(FA)Pb_2Br_7$	0.92	0.08	0.12	0.83	0.993
Exchanged $(HA)_2(FA)Pb_2Br_7$	0.89	0.07	0.14	1.22	0.995
$(HA)_2(FA)Pb_2I_7$	0.84	0.09	0.17	1.21	0.997

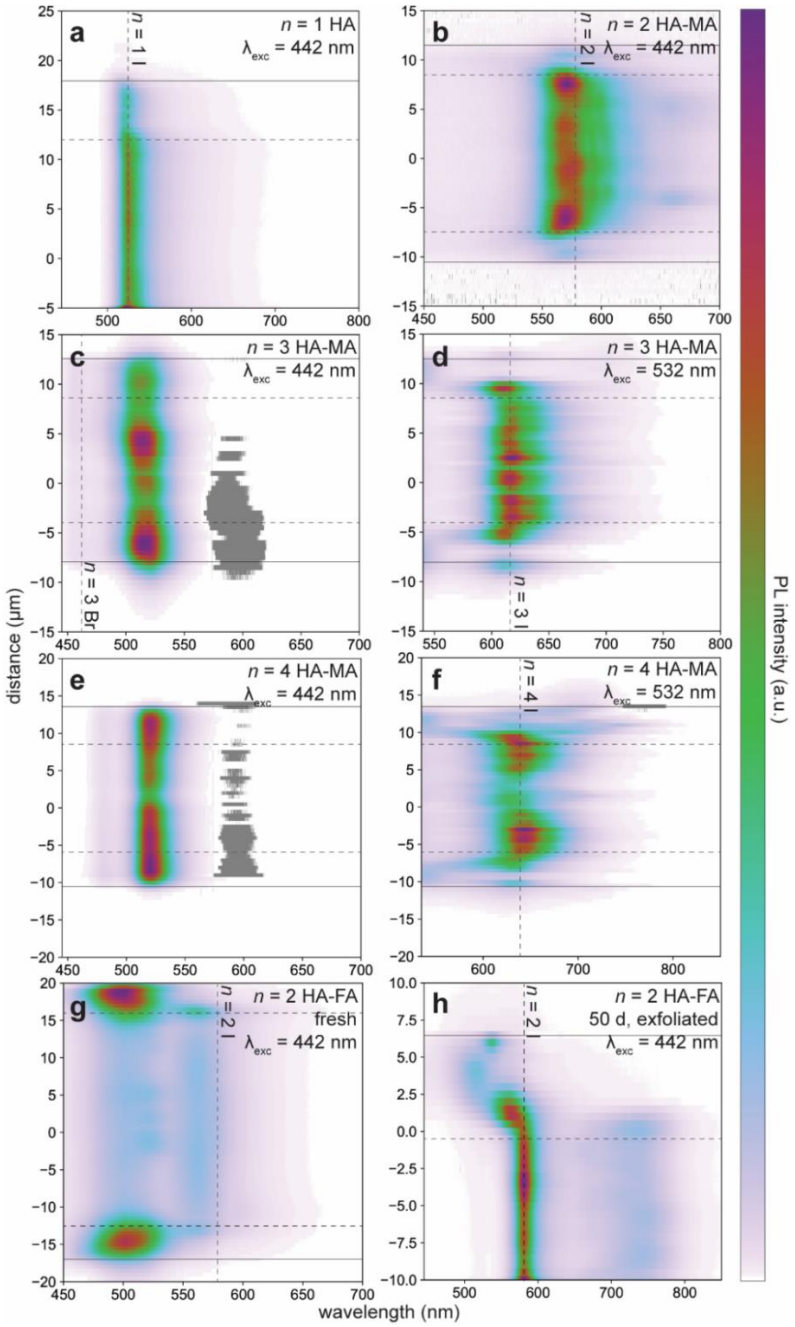

Figure A2.5. Additional PL line scans of exchanged lateral heterostructures. Confocal PL line scans across the lateral profiles of various RPP microplates after anion exchange with HBr vapor: **(a)** Extended data for the $n = 1$ HA-Pb-I/Br heterostructure shown in main text Table 3.1f. **(b)** The entire profile of a $n = 2$ HA-MA-Pb-I/Br heterostructure. **(c,d)** The entire profile of a $n = 3$ HA-MA-Pb-I/Br heterostructure under **(c)** 442 nm excitation and **(d)** 532 nm excitation. **(e,f)** The entire

profile of a n = 4 HA-MA-Pb-I/Br heterostructure under **(e)** 442 nm excitation and **(f)** 532 nm excitation. **(g)** An n = 2 HA-FA-Pb-I/Br heterostructure. **(h)** An exfoliated layer from an n = 2 HA-FA-Pb-I/Br heterostructure that has been kept in ambient conditions for 50 days. Dashed and solid horizontal reference lines indicate the junctions and edges of each heterostructure, respectively. Vertical reference lines are placed at known characteristic emission wavelengths of I and Br RPP phases relevant to the subject of each scan.

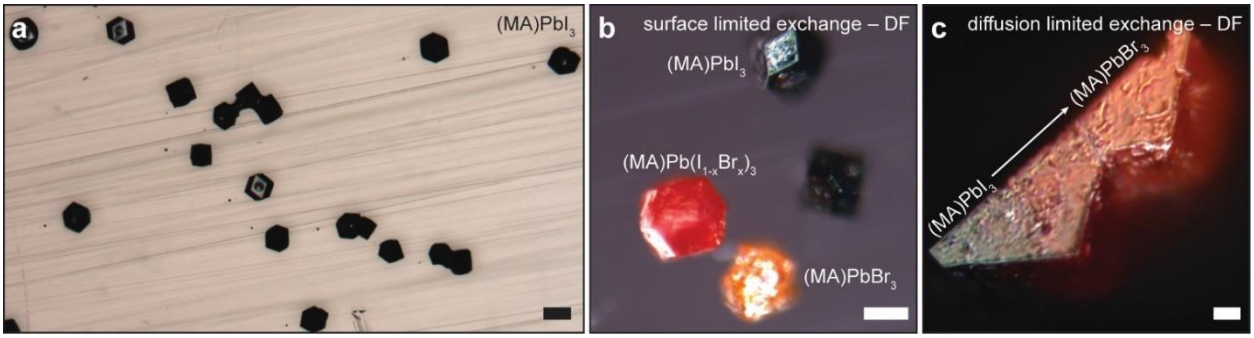

Figure A2.6. Optical micrographs of $MAPbI_3$ microcrystals before and after HBr vapor-solid anion exchange. **(a)** $MAPbI_3$ microcrystals grown via aqueous droplet growth before exchange. Scale bar is 100 µm. **(b)** Outcome of a surface limited anion exchange reaction with several $MAPbI_3$ microcrystals (dark field). **(c)** Outcome of a diffusion limited anion exchange reaction with a $MAPbI_3$ microcrystal (dark field). There is a visible gradient from $MAPbI_3$ to $MAPbBr_3$ in the crystal. Scale bars in b & c are 10 µm.

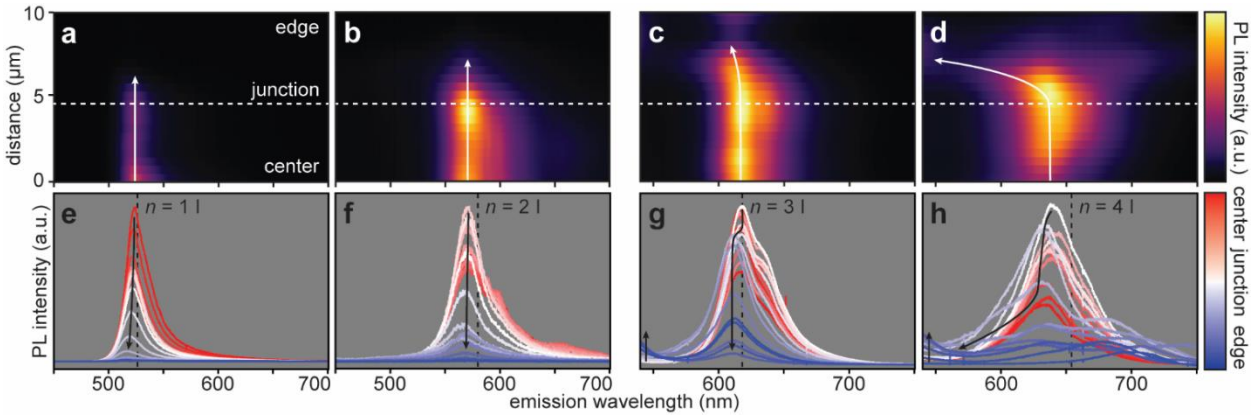

Figure A2.7. Spectral decompositions of PL linescans across the phase boundaries of various n = 1 – 4 HA-MA-Pb-I/Br heterostructures. **(a-d)** Confocal PL line scans across the junctions of heterostructures analogous to those shown in Figure 3.1b-e (but these are not the same specific microplates). a & b were excited at 442 nm; c & d were excited at 532 nm. White arrows are visual guides to track spectral shifts across the junctions. **(e-h)** Individual spectra from distance slices of the line scans shown in a-d. Vertical reference lines indicate the characteristic emission wavelengths for pure iodide analogues of the RPPs presented; black arrows track the intensity and central wavelength of the spectra from the junction to the edge.

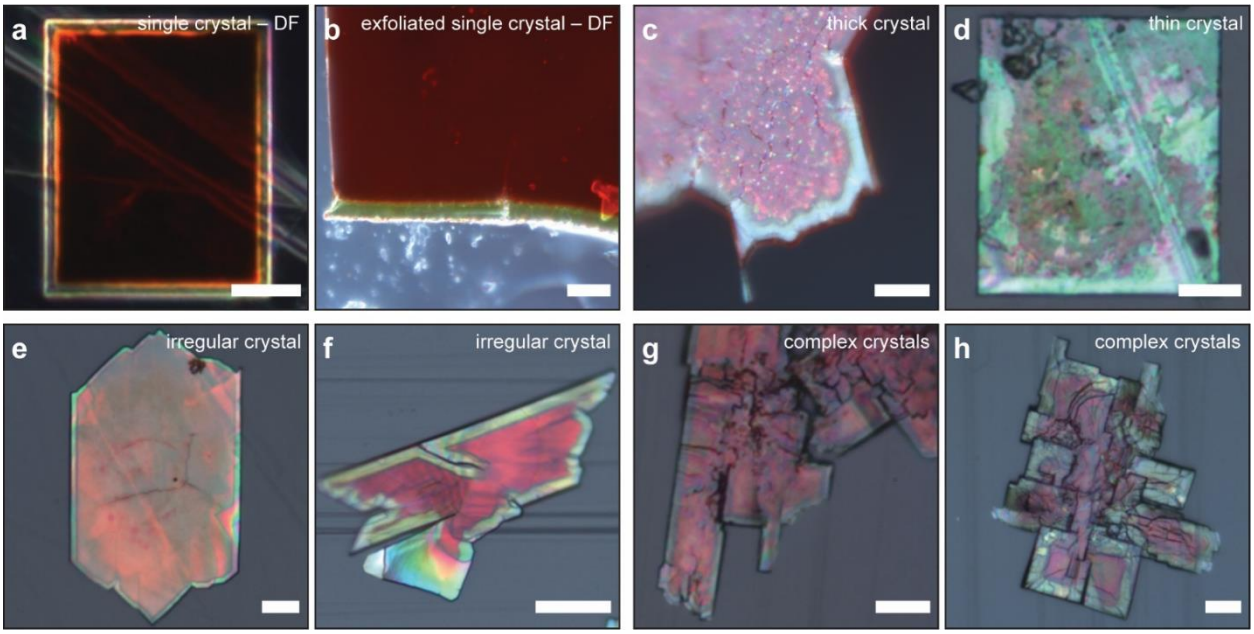

Figure A2.8. Additional optical micrographs of exchanged $(HA)_2(FA)Pb_2I_7$ RPP structures with various morphologies. **(a)** Monocrystalline microplate (dark field image), **(b)** layer exfoliated from a large single crystal (dark field image), **(c)** an unexfoliated thick crystal, **(d)** a thin microplate that has been completely exchanged, **(e,f)** irregularly shaped microplates, **(g,h)** polycrystalline aggregates of microplates. Scale bars are 10 μm.

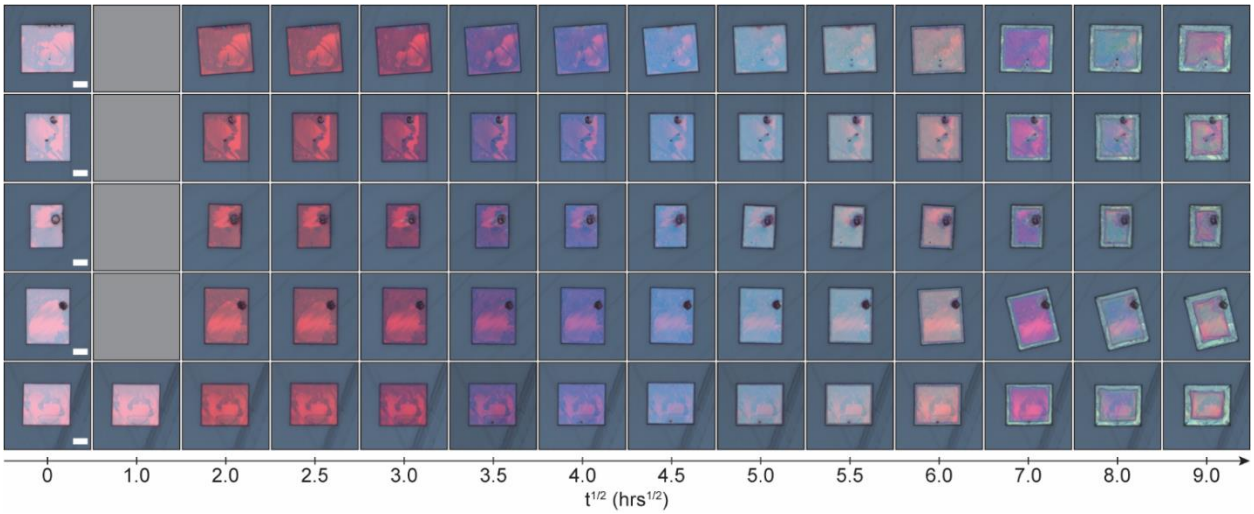

Figure A2.9. Image matrix for the anion exchange of five $(HA)_2(FA)Pb_2I_7$ microplates as a function of exchange time. Each row follows an individual $(HA)_2(FA)Pb_2I_7$ microplate from a single sample as it undergoes exchange reaction with HBr vapor. All scale bars are 10 μm.

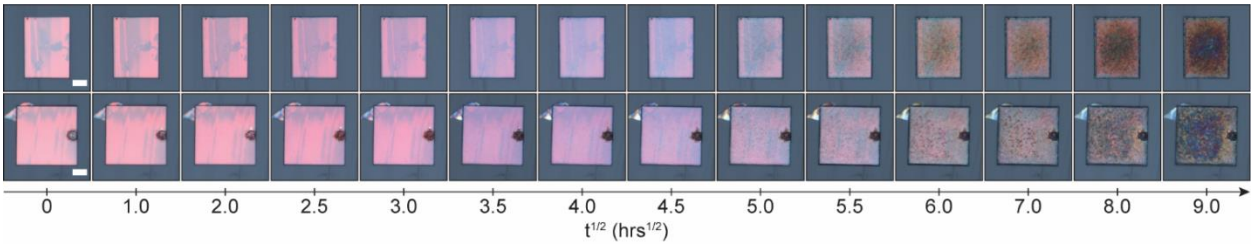

Figure A2.10. Image matrix for the environmental exposure of two $(HA)_2(FA)Pb_2I_7$ microplates as a function of exposure time. Each row follows an individual $(HA)_2(FA)Pb_2I_7$ microplate over time in ambient conditions. All scale bars are 10 μm.

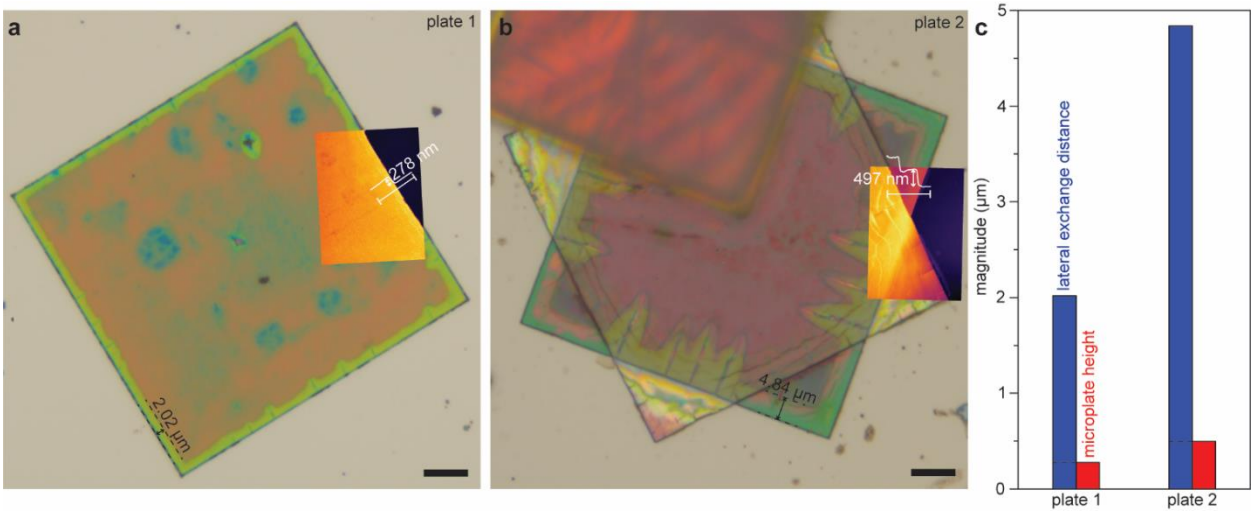

Figure A2.11. Direct comparison of the height and lateral exchange distance in $n = 2$ HA-FA-Pb-I/Br heterostructures. **(a,b)** Optical micrographs of two $n = 2$ HA-FA-Pb-I–Br heterostructures prepared via solution transport and vapor-solid anion exchange with HBr vapor with overlaid AFM topography images and height profiles (inset false-color images). Scale bars are 10 µm. **(c)** Comparison of the lateral exchange distance to the microplate height (measured by AFM) for the microplates imaged in a & b.

Additional discussion of vertical vs. lateral anion exchange rates

The directly measured heights of the microplates in Figure A2.7a-b represent the upper bounds of vertical anion exchange for $(HA)_2(FA)Pb_2I_7$. If vertical anion exchange proceeds to completion, the entire $(HA)_2(FA)Pb_2I_7$ microplate would be converted to $(HA)_2(FA)Pb_2Br_7$ and no lateral interface would be visible. Therefore, the observable lateral interfaces in the microplates shown indicate that the vertical exchange depth is less than the height of the microplate. Since the heights of each microplate are nearly an order of magnitude smaller than the widths of the exchanged $(HA)_2(FA)Pb_2Br_7$ at the microplates' edges, it can be concluded that the vertical anion

exchange rate is over an order of magnitude slower than the lateral anion exchange rate in $(HA)_2(FA)Pb_2I_7$.

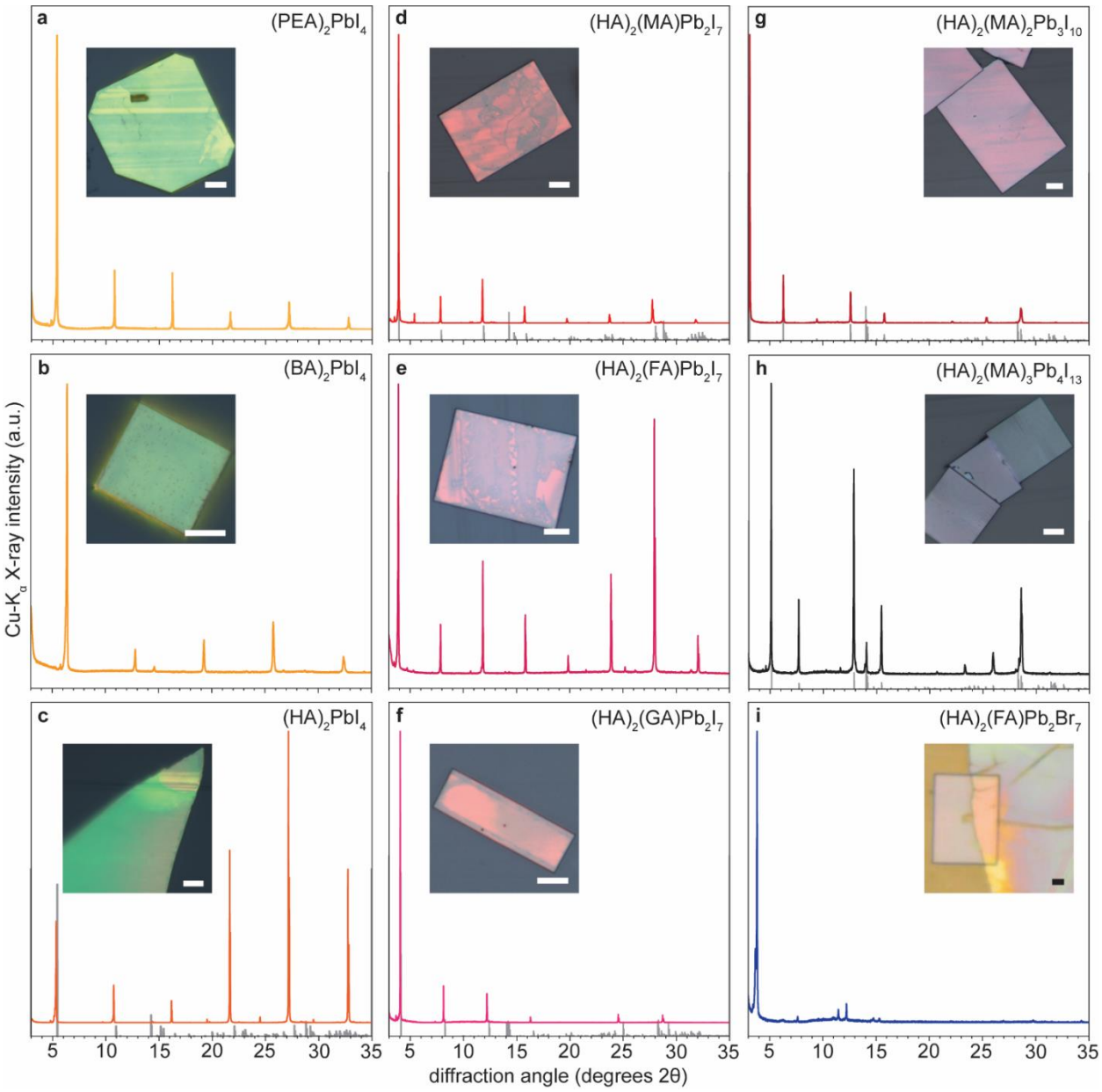

Figure A2.12. PXRD patterns confirming the crystalline phases of the RPP microplates. Powder X-ray diffraction patterns for all compounds studied in this work. Calculated reflection intensities from available CIFs (CCDC refs.: **(a)** 200737[3], **(b)** 665690, **(c)** 665695[4], **(d)** 1904716[5], **(f)**

1888368[6], **(g)** 1904714, **(h)** 1904715[5]) are presented as gray lines below the experimental patterns. Inset images are optical micrographs of representative microplates. All scale bars are 10 μm.

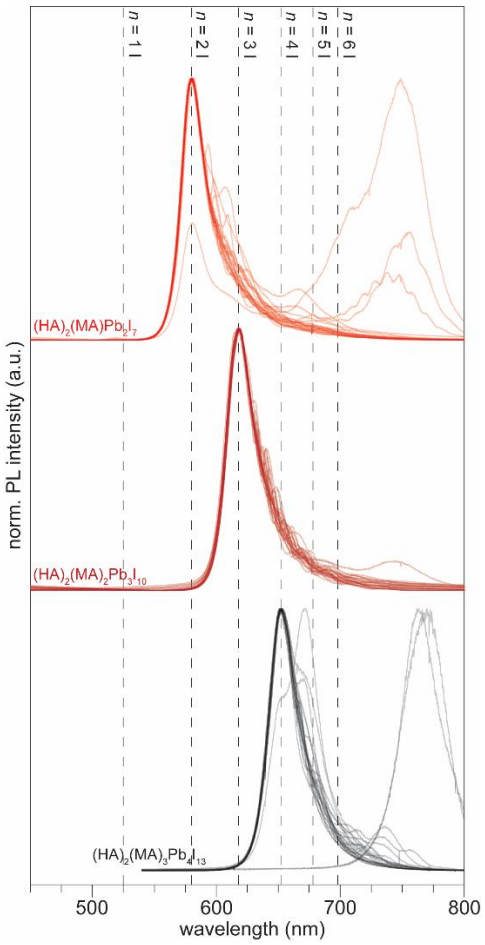

Figure A2.13. Phase purity and distribution of $n > 1$ HA-MA-Pb-I RPP microplates. Confocal PL spectra collected from 25 individual microplates each among samples of $n = 2 – 4$ HA-MA-Pb-I. Reference lines mark emission wavelengths for common lead iodide RPPs of different n.

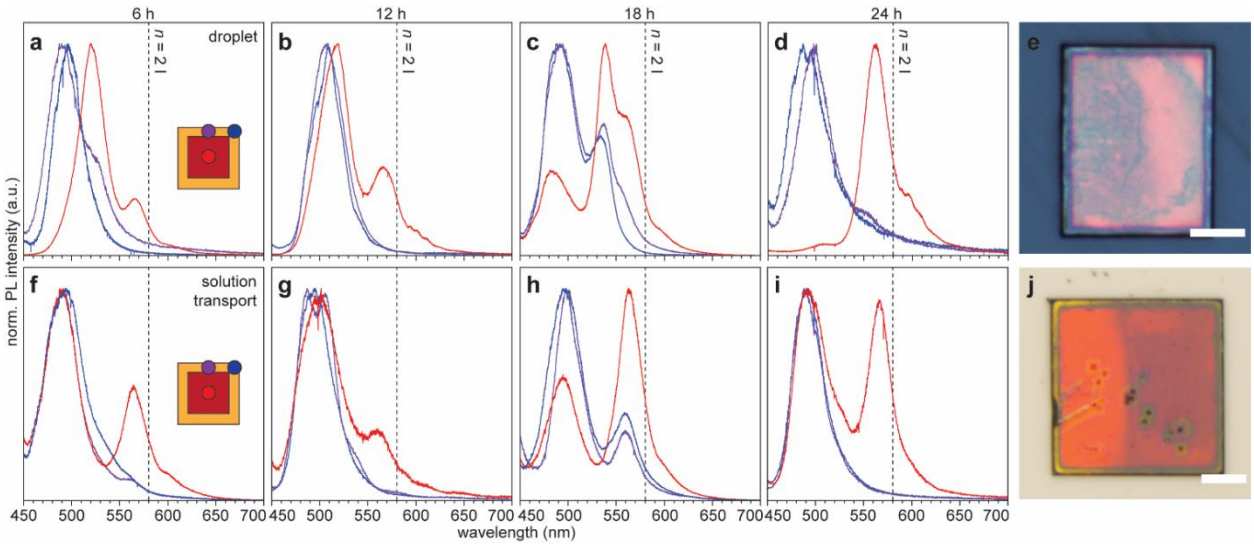

Figure A2.14. Comparison of exchange behaviors as a function of the synthetic methods used to prepare the starting $(HA)_2(FA)Pb_2I_7$ microplates. Confocal PL spectra collected from different sections of $(HA)_2(FA)Pb_2I_7$ microplates after incremental anion exchange reaction times with HBr vapor using **(a-d)** microplates prepared via aqueous droplet growth, and **(f-i)** microplates prepared via solution transport growth. Excitation sections are indicated in the inset cartoons of a & e with colored spots. Reference lines are at the characteristic emission wavelength of $n = 2$ iodide RPPs. **(e,j)** Optical micrographs of representative $n = 2$ HA-FA-Pb-I/Br heterostructures prepared via anion exchange with HBr vapor from starting microplates synthesized via **(e)** aqueous droplet growth and **(j)** solution transport growth. Scale bars are 10 μm. Some samples of $(HA)_2(FA)Pb_2I_7$ had to be synthesized using solution transport to yield intact microplates on a conductive surface because the aqueous droplet method is limited to hydrophobic polymer substrates. This comparison shows that the anion exchange behaviors are qualitatively consistent regardless of how the starting microplates were synthesized.

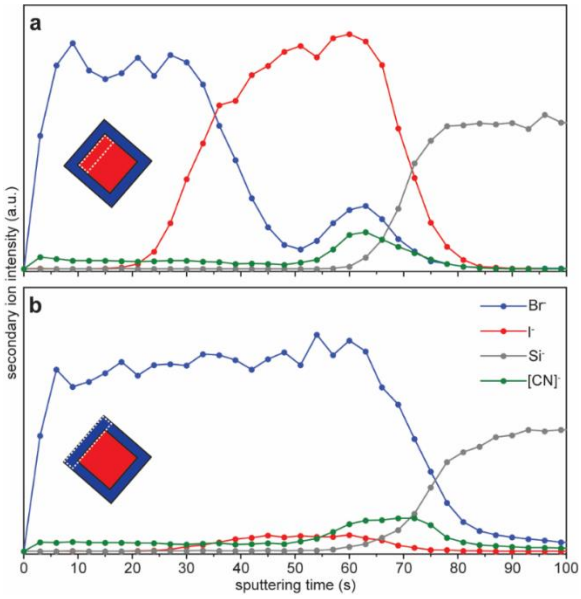

Figure A2.15. Full SIMS sputtering profiles including the organic ion signals collected on the n = 2 HA-FA-Pb-I/Br lateral heterostructure. Extended data for the SIMS sputtering profiles collected at the **(a)** inner and **(b)** outer components of the heterostructure imaged in Figure 3.4e,f. Inset cartoons indicate the sputtering areas as white dashed boxes.

Additional interpretation of SIMS sputtering profiles

There is a secondary bromide signal deeper into the plate and just above the silicon substrate in the center sputtering profile, which implies that HBr can permeate beneath the specimens as prepared here, but to a lesser extent than the exposed top surface. The second bromide peak's correlation with organic ion signals implies that this portion of the sputtering profile is from the interface between the microplate and the substrate, not the microplate itself. This is likely because the surface of the silicon substrate becomes contaminated by traces of the organic reagents in the solution during the dissolution-reprecipitation growth, leaving a layer of organic residue between the plate and the substrate.

A2.3. References

(1) Salvador, M.; Motter, C. E.; McCulloch, I. Hidden Perils of Lead in the Lab: Guidelines for Containing, Monitoring, and Decontaminating Lead in the Context of Perovskite Research. *Chem. Mater.* **2020**, *32* (17), 7141–7149.
(2) Billing, D. G. Bis(1-phenylethylammonium) tetraiodoplumbate(II). *Acta Crystallogr. Sect. E* **2002**, *58* (11), m669–m671.
(3) Billing, D. G.; Lemmerer, A. Synthesis, Characterization and Phase Transitions in the Inorganic-Organic Layered Perovskite-Type Hybrids [(C*n*H2*n*+1NH3)2PbI4], *n* = 4, 5 and 6. *Acta Crystallogr. Sect. B* **2007**, *63* (5), 735–747.
(4) Spanopoulos, I.; Hadar, I.; Ke, W.; Tu, Q.; Chen, M.; Tsai, H.; He, Y.; Shekhawat, G.; Dravid, V. P.; Wasielewski, M. R.; Mohite, A. D.; Stoumpos, C. C.; Kanatzidis, M. G. Uniaxial Expansion of the 2D Ruddlesden–Popper Perovskite Family for Improved Environmental Stability. *J. Am. Chem. Soc.* **2019**, *141* (13), 5518–5534.
(5) Fu, Y.; Hautzinger, M. P.; Luo, Z.; Wang, F.; Pan, D.; Aristov, M. M.; Guzei, I. A.; Pan, A.; Zhu, X.; Jin, S. Incorporating Large A Cations into Lead Iodide Perovskite Cages: Relaxed Goldschmidt Tolerance Factor and Impact on Exciton–Phonon Interaction. *ACS Cent. Sci.* **2019**, *5* (8), 1377–1386.

Appendix 3. Supplementary Information for Chapter 4

A3.1. Experimental Methods

Materials & Chemicals

Unfrosted glass microscope slides used in syntheses were cleaned in 3 x 30 min ultrasonication steps in alkaline detergent (1), ethanol (2), and deionized water (3) before being dried in an oven for at least 1 hour. They were stored in a covered container prior to use. 17-mil polydimethylsiloxane (PDMS) on polyethylene was purchased from GelPak (part no. PF-65x65-0170-X4). p-type Si wafer (<100>, native oxide) was purchased from University Wafer.

Methylammonium iodide (MAI, 99%), methylammonium-^{13}C chloride (^{13}C-MACl, 99 atom% ^{13}C), *n*-butylammonium iodide (BAI, 98%), *n*-butylamine (BA, 99.5%), *n*-pentylamine (PA, 99%), *n*-hexylamine (HA, 99%), lead(II) iodide (PbI_2, 99%), lead(II) oxide (PbO, ≥99.0%), trichloro(1H, 1H, 2H, 2H-perfluorooctyl)trichlorosilane (PFOCTS, 97%), hydroiodic acid (HI, 47 wt. % in H_2O, stab. 1.5% H_3PO_2), hypophosphorous acid (H_3PO_2, 50 wt. % in H_2O), and γ-butyrolactone (GBL, 99.9%) were purchased from Sigma Aldrich. Methylammonium chloride (MACl) and phenethylamine (PEA) were purchased from Acros Organics. Formamidinium iodide (FAI), guanidinium iodide (GAI), and *n*-hexylammonium iodide (HAI) were purchased from GreatCell Solar. HI was reduced by mixing with H_3PO_2 in a 10:1 volumetric ratio to remove residual I_2/I_3^- prior to use. GBL was dried and stored over 3Å molecular sieves prior to use. All other chemicals were used as purchased.

Synthesis of methylammonium-^{13}C iodide (^{13}C-MAI) Precursor Salt

A 1 M aqueous solution of ^{13}C-MAI was prepared in a 10 mL beaker by dissolving 3 mmol (205 mg) of ^{13}C-MACl in 3 mL 10:1 (v/v) HI/H_3PO_2. The solvent was then slowly evaporated on

a hot plate set to 125°C, leaving a slurry of the off-white precipitate ^{13}C-MAI. The precipitate was isolated via vacuum filtration through paper under liberal washes of diethyl ether. The ^{13}C-MAI was then purified via recrystallization from IPA by preparing a supersaturated solution on a hot plate set to 75°C, reducing the solution to a third of its original volume (~2 mL), then cooling it to -10°C in a freezer for 3 h. The recrystallized ^{13}C-MAI was isolated via vacuum filtration through paper, washed thoroughly with diethyl ether, and dried under vacuum overnight (0.1-2 mm colorless flakes, yellow before washing, 41% yield).

Growth of 3D Perovskite Single Crystals

Single crystals of $MAPbI_3$ and $(FA_{0.9}Cs_{0.1})PbI_3$ were grown in between hydrophobic glass or Si substrates using modifications of previously reported space-confined, inverse temperature crystallization techniques.[1,2]

Glass and Si growth substrates were functionalized with a hydrophobic surface using an adaptation of a common glassware silanization technique.[3] Cleaned glass microscope slides or cleaved rectangles of Si wafer were dusted with air and arranged standing in a vacuum bell jar around a small beaker containing 200 µL of PFOCTS. Care was taken to ensure all substrate surfaces were not in contact with another material so all surfaces would be functionalized. The bell jar was then evacuated of air on a Schlenk line until the PFOCTS began to boil, at which point the valve was closed off from vacuum and allowed to sit for 15 min. This process was repeated two more times before re-opening the chamber to air. The silanized slides were then cured in an oven for 3 h at 80°C, allowed to cool to room temperature, then twice washed/wiped using DI water and cleanroom wipes.

For $MAPbI_3$, a vial containing a 1.5 M solution of $(MA)PbI_3$ (1:1 PbI_2:MAI) in GBL was heated on a hot plate to 80°C under stirring until all visible solids were dissolved (~30 min). A 7.5 µL bead of the precursor solution was then pipetted onto the center of a ~1 cm x 1 cm piece of silanized glass or Si wafer, then a piece of silanized glass was gently laid atop the substrate to press the solution into a thin layer at the interface. The substrate/solution stack was then heated to 130°C in 10°C increments every 30 min and allowed to grow at 130°C for ~1-2 h, typically yielding 10s of 500 µm – 1 mm-wide hexagonal plates of $MAPbI_3$ on each substrate surface. When the crystals were of desired quality (large and specular), the substrate stack was removed from the hot plate and immediately submerged in a bath of acetonitrile (Me)CN in a Petri dish, delaminating the substrates and washing the surface of residual precursor solution in the process. The substrate was gently swished in the bath for ~3 s before removing and quickly drying under a stream of nitrogen. The samples were then immediately stored in an inert atmosphere until heterostructure assembly.

For $(FA)_{0.9}Cs_{0.1}PbI_3$, a vial containing a 1.5 M solution of $(FA_{0.9}Cs_{0.1})PbI_3$ (0.9:0.1:1 FAI:CsI:PbI_2) in GBL was prepared by dissolving the precursor salts in GBL under stirring at room temperature overnight. A 7.5 µL bead of the room temperature solution was then pipetted onto the center of a ~1 cm x 1 cm piece of silanized glass or Si wafer preheated to 100°C to induce rapid nucleation of small 3D LHP crystals. We observed that the LHP phase preferentially nucleates under the rapid perturbation at edges of the droplet when exposed to air. By pre-nucleating the LHP phase, the crystallites seed the growth of the black perovskite phase for the remainder of the reaction, minimizing formation of the non-perovskite yellow phase of $FAPbI_3$. Immediately following the nucleation event, a piece of silanized glass was pressed onto the substrate to press the solution into a thin layer at the interface and distribute the LHP crystallites across the substrates. The substrate/solution stack was then heated to 130°C in 10°C increments every 30 min and

allowed to grow at 130°C for ~1-2 h, typically yielding 10s of 100 µm – 500 µm -wide hexagonal plates of $(FA_{0.9}Cs_{0.1})PbI_3$. The crystals were then isolated and dried in the same fashion as $MAPbI_3$.

Growth of 2D and R–P Perovskite Microsheets

Thin (10-100 nm) sheets of 2D and R–P perovskites were grown from the aqueous/air interface of a drop of HI-based precursor solution as previously reported.[4,5]

In this work, the floating sheets were picked up using small (~1 mm x 1 mm) PDMS stamps adhered to a piece of silanized glass. The glass substrates used for growth were tested beforehand for high wettability by visually inspecting the wetting of a water droplet. All sheet growth was performed at room temperatures and relative humidities ranging from 21°C - 25°C and 19% - 40%, respectively. We emphasize that the sheet nucleation characteristics vary significantly at high humidity, on low-wettability substrates, and when intact crystals are inadvertently drawn with the heated precursor solution. It is also noteworthy that the phase dispersity increases if multiple retrievals are performed from the same droplet – this is especially problematic with higher *n* target phases, but is unimportant for $n = 1$ phases where phase dispersity is impossible. Precursor concentrations and supersaturation temperatures for the phases grown in this work are listed in Table A3.1.

Table A3.1) Precursor concentrations and growth temperatures for the 2D LHPs studied in this work.

Compound	$[LA^+]$ (M)	$[A^+]$ (M)	$[Pb^{2+}]$ (M)	T_{growth} (°C)
$(BA)_2PbI_4$	0.300	-	0.300	36-40
$(PA)_2PbI_4$	0.200	-	0.200	36-40
$(HA)_2PbI_4$	0.100	-	0.100	36-40
$(PEA)_2PbI_4$	0.030	-	0.100	38-42
$(BA)_2(MA)Pb_2I_7$	0.251	0.289	0.450	36-40
$(HA)_2(MA)Pb_2I_7$	0.150	0.250	0.500	36-40
$(HA)_2(FA)Pb_2I_7$	0.050	0.125	0.450	36-40

$(HA)_2(GA)Pb_2I_7$	0.052	0.696	0.500	36-40
$(BA)_2(MA)_2Pb_3I_{10}$	0.202	0.378	0.450	38-42
$(BA)_2(MA)_3Pb_4I_{13}$	0.134	0.550	0.450	38-42

Growth of Bulk Mixed-Cation 2D & 3D Perovskite Crystals

Bulk crystals of $(HA)_2(MA)_2Pb_3I_{10}$, $(HA)_2((MA)_{1-x}(FA)_x)_{n-1}Pb_nI_{3n+1}$, and $(HA)_2((MA)_{1-x}(GA)_x)_{n-1}Pb_nI_{3n+1}$, were grown via cooling of supersaturated perovskite precursor solutions in concentrated HI. The concentrations for each 2D precursor were adopted from those used to synthesize the targeted parent phase $(HA)_2(MA)_2Pb_3I_{10}$ in a previous report.[6]

For each 2D sample, 1 mmol (223 mg) PbO powder and 1 mL HI were added to a glass scintillation vial and heated on a hot plate at 130°C. In separate vials, 1.333 M stock solutions of MAI, FAI, and GAI were each prepared by dissolving the respective precursors in the appropriate volume of 10:1 (v/v) HI/H_3PO_2. In another vial, a 0.945 M stock solution of HA in H_3PO_2 was prepared by slowly adding HA to the appropriate volume of H_3PO_2. A mixture of the AI stock solutions (MA/FA or MA/GA) totaling 500 µL in volume (386 mmol of total AI, exact concentrations listed in Table A3.2) were added to the PbO/HI mixture. The reaction vial was agitated, then allowed to sit for 30 min at 130°C before adding 225 µL of the HA stock solution and agitating the vial again. The samples were then allowed to sit at 130°C for an additional hour, being agitated at ~15 min intervals to ensure thorough mixing, then cooled naturally to room temperature overnight.

The precipitates were isolated via suction filtration through paper, then liberally washed of residual HI via 3 rounds of steeping in pools of chilled diethyl ether followed by suction filtration. The washed filtrates were then dried under vacuum on a Schlenk line for 24 h.

Table A3.2) Precursor concentrations and volumes used for the growth of bulk crystals of $(HA)_2(MA)_2Pb_3I_{10}$, $(HA)_2((MA)_{1-x}(FA)_x)_{n-1}Pb_nI_{3n+1}$, and $(HA)_2((MA)_{1-x}(GA)_x)_{n-1}Pb_nI_{3n+1}$.

Target Compound (nominal)	$[Pb^{2+}]$ (M)	$[MA^+]$ (M)	$[FA^+]$ (M)	$[GA^+]$ (M)	$[HA^+]$ (M)	V_{total} (mL)
$(HA)_2(MA)_2Pb_3I_{10}$	0.579	0.386	-	-	0.123	1.725
$(HA)_2((MA)_{0.75}(FA)_{0.25})_2Pb_3I_{10}$	0.579	0.290	0.097	-	0.123	1.725
$(HA)_2((MA)_{0.50}(FA)_{0.50})_2Pb_3I_{10}$	0.579	0.193	0.193	-	0.123	1.725
$(HA)_2((MA)_{0.25}(FA)_{0.75})_2Pb_3I_{10}$	0.579	0.097	0.290	-	0.123	1.725
$(HA)_2(FA)_2Pb_3I_{10}$	0.579	-	0.386	-	0.123	1.725
$(HA)_2((MA)_{0.75}(GA)_{0.25})_2Pb_3I_{10}$	0.579	0.290	-	0.097	0.123	1.725
$(HA)_2((MA)_{0.50}(GA)_{0.50})_2Pb_3I_{10}$	0.579	0.193	-	0.193	0.123	1.725
$(HA)_2((MA)_{0.25}(GA)_{0.75})_2Pb_3I_{10}$	0.579	0.097	-	0.290	0.123	1.725
$(HA)_2(GA)_2Pb_3I_{10}$	0.579	-	-	0.386	0.123	1.725

Assembly of 2D/3D Heterostructures

2D perovskite microsheets (grown as described above) on PDMS stamps were dry-transferred onto the 3D crystal surfaces using a home-built van der Waals heterostructure assembly rig consisting of a reflective optical microscope (Olympus BX51M), a transfer z-stage (base, neck, and stage mount of an Olympus BX53) to which the transparent stamps were mounted on a microscope slide, and a mechanical x-y-θ stage at the bottom, on which the 3D crystal substrates were mounted. The 2D sheets were lowered onto the pre-positioned 3D surface until first contact (evidenced by visible wetting of the PDMS stamp), then the stamp was slowly retracted to yield a 2D/3D heterostructure. We observed the highest transfer yield with thinner 2D sheets (<100 nm), slow stamp removal, and when 2D sheets were picked up directly from the growth solution with the PDMS stamp (vs. exfoliated). If the contact area of the stamp on the 3D crystal is very large, there is some chance that the 3D crystal is picked up by the stamp, rather than the 2D sheet transferring onto the 3D crystal.

Basic Sample Characterization (Optical Microscopy, SEM, AFM, PXRD, Contact Angle)

Optical microscope images were collected under episcopic (reflective) illumination from a tungsten-halogen lamp using an Olympus BX51M widefield optical microscope with a RGB sCMOS camera (ThorLabs Kiralux CM895CU) at the trinocular head.

Cross section samples of 3D SCs were prepared by growing 3D SCs on silanized p-type Si and cleaving the wafer substrate to expose fresh 3D SC edges at the cleavage plane. SEM cross-sections were collected in a Zeiss Leo Supra 55V scanning electron microscope at a 5 kV accelerating voltage. The secondary electron signal was collected using an Everhart–Thornley detector.

AFM topography was collected in tapping mode using an Agilent Keysight 5500 atomic force microscope with Bruker NCHV-A tips (spring constant: 40 Nm^{-1}). The samples were in an environmental chamber under a dry N_2 atmosphere for the duration of the topography acquisition to prevent surface degradation. Topography images were processed in Gwyddion SPM data analysis software. Each topography image (trace) was row-aligned using the median of differences method before subtracting a 2^{nd} order 2D polynomial background. Topography profiles were further flattened by subtracting lines of median gradient.

Powder X-ray diffraction patterns were collected using a Bruker D8 Advance powder diffractometer configured in Bragg–Bentano geometry with a Cu-K_α source. Incident X-ray background at low diffraction angles was attenuated using a knife edge.

Contact angles of RODI water on glass substrates were measured via the sessile drop method, using a custom-built transmissive optical microscope with a horizontal (parallel to ground) optic axis as an impromptu contact angle goniometer.

(Time-Resolved) Photoluminescence Microscopy

PL spectra and TRPL transients were collected in a custom-built widefield hyperspectral microscope under pulsed 370 nm excitation.

The 370 nm beam from a pulsed laser diode (Horiba DeltaDiode DD375L, variable rep. rate, 50 ps pulse duration) was filtered using a 370±10 nm excitation (bandpass) filter (ThorLabs FBH370-10) before being relayed onto the microscope's optic axis using a 400 nm longpass dichroic mirror (Nikon DM400). The filtered beam was condensed through a microscope objective (Olympus UMPlanFl 10×, NA 0.30) to produce a focused spot in the sample plane. Epi-directional photoluminescence was collected through the same objective and twice filtered of the excitation light through the dichroic mirror and a 450 nm longpass filter (ThorLabs FELH0450, OD5+) before being imaged through a tube lens and passed through a slit into an imaging spectrograph (Princeton Instruments Acton sp2300i). For spectra, the PL spot was dispersed onto a sCMOS camera (Andor Neo 5.5) with a ruled grating (150 grooves/mm, 800 nm blaze). For TRPL, the PL spot was diverted onto an avalanche photodiode (IDQ ID100-20-STD) using a mirror on the spectrograph's grating turret. TRPL transients were generated using a time-correlated single photon counting module (Becker & Hickl SP130). All PL spectra were denoised with a 3x3 median filter and subtracted of dark counts using an unilluminated portion of each camera frame before binning the frame into a spectrum. For TRPL acquisitions, dark counts were subtracted using the experimental dark current of the avalanche photodiode.

Widefield Photoluminescence Imaging

Widefield spectral images of photoluminescence were collected in a custom-built hyperspectral microscope under episcopic illumination from a 405 nm CW laser diode.

The excitation beam from a 405 nm CW laser diode was diverged with a plano-convex lens before being transmitted through a 405±20 nm excitation (bandpass) filter into an optical fiber. A small fraction of the 405 nm light was relayed from the fiber output onto the microscope's optical axis using a 400 nm longpass dichroic mirror, then condensed through a microscope objective (Olympus UMPlanFl 10×, NA 0.30) to yield a uniform excitation field across the sample plane. Epi-directional photoluminescence was collected through the same objective, filtered of the excitation light through a 450 nm longpass filter and a selection of secondary filters (see Figure 4.2 for selected wavelength ranges), then imaged through an infinity-corrected tube lens onto a sCMOS camera (Andor Neo 5.5) in an imaging spectrograph (Princeton Instruments Acton sp2300i).

Photoluminescence Excitation (PLE) Spectroscopy

PLE spectra were collected in a custom-built hyperspectral microscope under pulsed excitation from a tunable optical parametric oscillator.

A small fraction of the tuned output of a Nd:YAG optical parametric oscillator (Ekspla NT300, 10 Hz rep. rate, 5 ns pulse duration) was relayed onto the microscope's optical axis using a 400 nm longpass dichroic mirror (Nikon DM400) and condensed onto the sample through a microscope objective (Olympus UMPlanFl 10×, NA 0.30) in a reflective geometry. Epi-directional photoluminescence was collected through the same objective and filtered of the excitation light using a longpass filter (ThorLabs FELH0750, OD5+) before being imaged onto an sCMOS camera using an infinity-corrected tube lens. The PLE spectrum is the binned intensity of a real-space image of the PL spot at each excitation wavelength. A background exposure was collected prior to the measurement to subtract mean dark count from the PLE datapoints.

Micro-transmittance Spectroscopy

Micro-transmittance spectra of 2D LHPs were collected in a custom-built hyperspectral microscope with front and back objectives under diascopic illumination from a tungsten-halogen lamp (Dolan-Jenner Fiber Lite MI-150, 3250K). A neighboring region of glass substrate was used as a reference for I_0 to compute transmittance as $T = I/I_0$. Light from the sample plane was collected and dispersed in the same fashion as PL spectra. Dark counts were subtracted from the data using unilluminated (blocked by an OD5 filter) portions of each camera frame as references, and matched regions of the sample frame occupied only by substrate were used as an internal reference for I_0 to correct for illumination intensity variations between sample and background frames. The absorbance spectra are averages over a range of the hyperspectral trace occupied by a single, homogeneous microcrystal surface.

Ambient and Accelerated Ageing of 2D/3D Heterostructures

Ambient ageing of 2D/3D HSs occurred at room temperature under a dry N_2 atmosphere in custom-built optical environmental chambers during and in-between PL measurements. The chamber consisted of a clamped stack of machined plates interfaced by cut-to-shape FEP gaskets with a front-side borosilicate optical window and enclosed by a flanged steel backplate. The chambers were purged with dried N_2 overnight after sample insertion, then plugged at the outlet to retain a positive pressure over the duration of the study. For accelerated ageing, samples were adhered to a hot plate in an Ar glovebox using double-sided Kapton® tape. The hotplate surface temperature was held at 65°C for the desired ageing time.

Time-of-Flight Secondary Ion Mass Spectrometry (ToF-SIMS) Depth Profiling

^{13}C-labelled 2D/3D heterojunctions were prepared on silanized p-type Si (100)/native oxide in the same fashion as their non-labelled counterparts, using ^{13}C-MAI instead of standard MAI. A portion of the 2D/3D heterojunctions underwent accelerated ageing for different durations at 65°C according to the protocol described above. The control samples (no accelerated ageing) were analyzed via AFM under a dry N_2 atmosphere prior to ToF-SIMS analysis. All ToF-SIMS samples were analyzed 9d after fabrication and packed/stored under argon prior to analysis.

ToF-SIMS analysis was conducted using a TOF-SIMS5 instrument (IONTOF GmbH, Műnster, Germany). An interlaced mode dual beam depth profiling strategy was used to perform 3D SIMS imaging analysis. The details have been described in a previous work with some minor modifications.[7] In brief, a 10 keV Ar cluster ($Ar_{1500\pm300}^+$) sputtering ion beam was used with a beam current of about 4.0 nA to remove sample layer-by-layer while the molecular information can be preserved. The scanning size of the Ar cluster ion beam was 1000 μm × 1000 μm, and the sputtering rate for typical organic materials was about 0.5 nm/s. A Bi_3^+ primary ion beam was focused to around 0.4 μm diameter and scanned over 150 × 150 μm^2 areas with 128 × 128 pixels per scan. The current of the Bi_3^+ beam was about 0.20 pA with 10 kHz pulse frequency, and data collection time was about 819 s (500 scans) per set of images. Delay extraction mode was used in image collection to ensure that both high mass resolution and high lateral resolution could be achievable. During data collection, a low energy electron flood gun was used to compensate any potential surface charging. Depth profiles were extracted from the SIMS images only in regions of uniform 2D/3D overlap, which were identified by positive contrast of $[HA]^+$ signal in ToF-SIMS images and registered to corresponding optical microscope images of each HS.

A3.2. Supplementary Figures

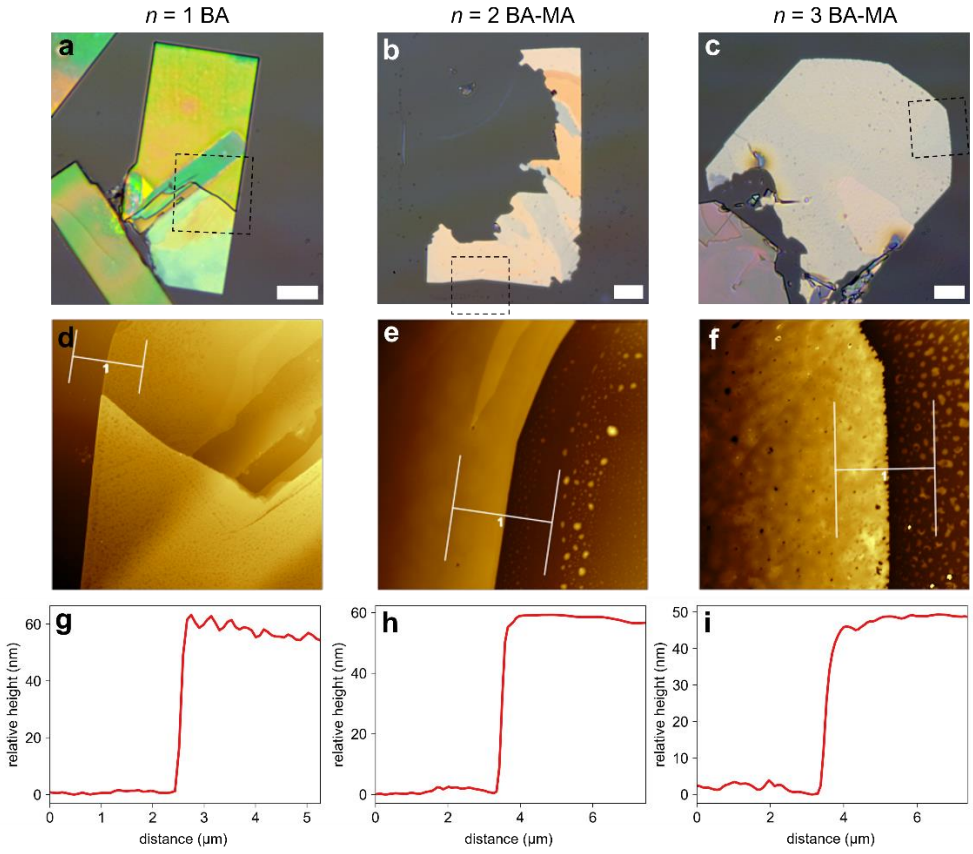

Figure A3.1) Basic optical and physical characteristics of 2D LHP microsheets. **(a-c)** Optical microscope images of n = 1 **(a)**, 2 **(b)**, & 3 **(c)** $(BA)_2(MA)_{n-1}Pb_nI_{3n+1}$ microsheets synthesized via droplet growth and dry-transferred onto glass. **(d-f)** AFM topography of regions of the microsheets in (a-c) (indicated by dashed boxes). **(g-i)** AFM topography traces of 2D microsheet edges corresponding to the annotations in (g-i). Scalebars are 10 μm.

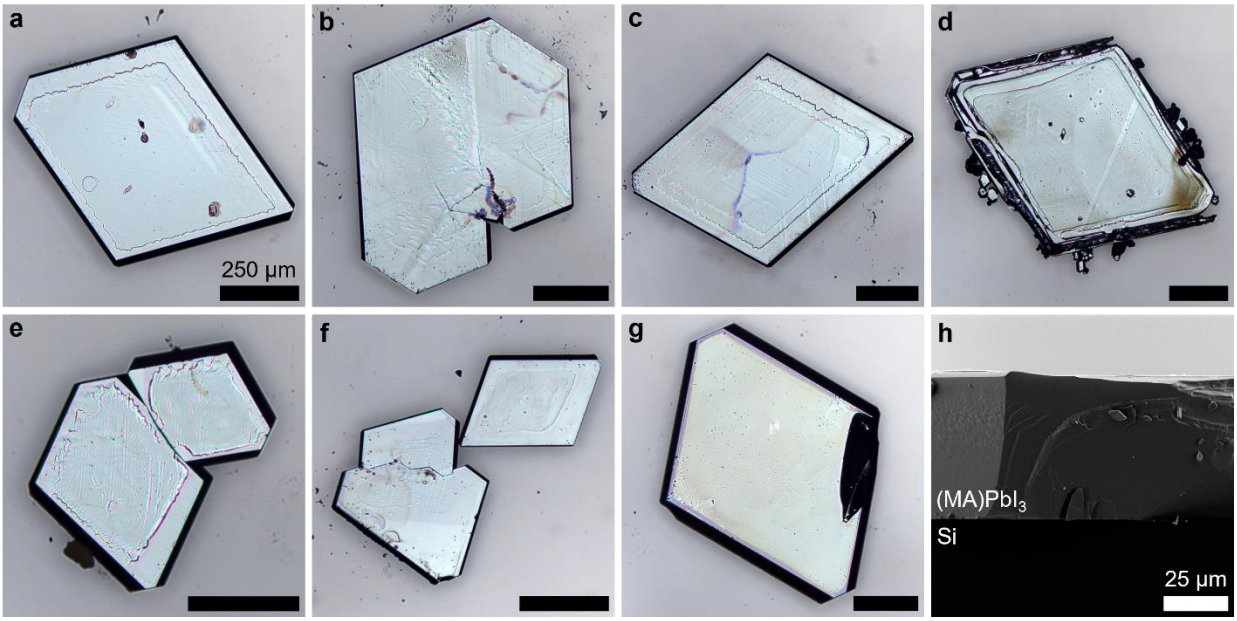

Figure A3.2) Optical microscope **(a-g)** and cross-sectional SEM **(h)** images of $MAPbI_3$ SCs grown via space-confined inverse temperature crystallization. All optical image scalebars are 250 µm.

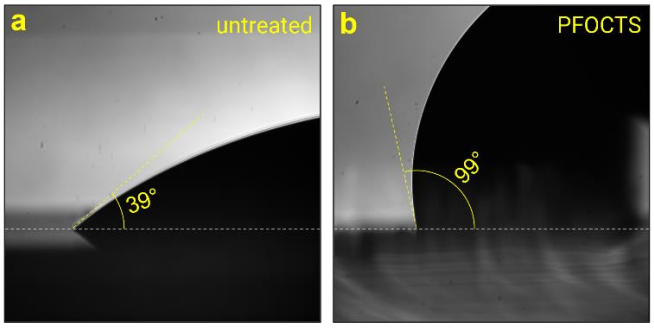

Figure A3.3) Water contact angle on untreated **(a)** and silanized **(b)** glass substrates.

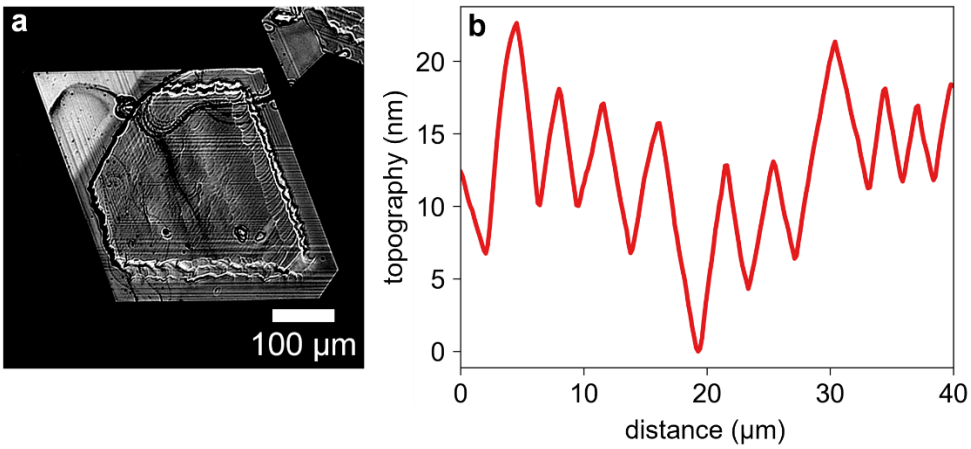

Figure A3.4) Characterization of etched striations on (Me)CN-washed 3D SC surfaces. **(a)** High contrast optical microscope image (green channel) of a $MAPbI_3$ SC after a 3s (Me)CN wash. **(b)** AFM topographical trace running perpendicular to (Me)CN-etched striations on a $MAPbI_3$ (100) surface.

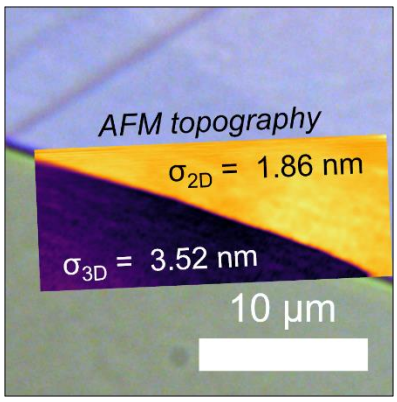

Figure A3.5) Zoomed optical microscope image and AFM topography (false color inset) of the *n* = 3 BA-MA|$MAPbI_3$ HS shown in Figure 4.1b, with annotated RMS roughness for the 2D and 3D regions.

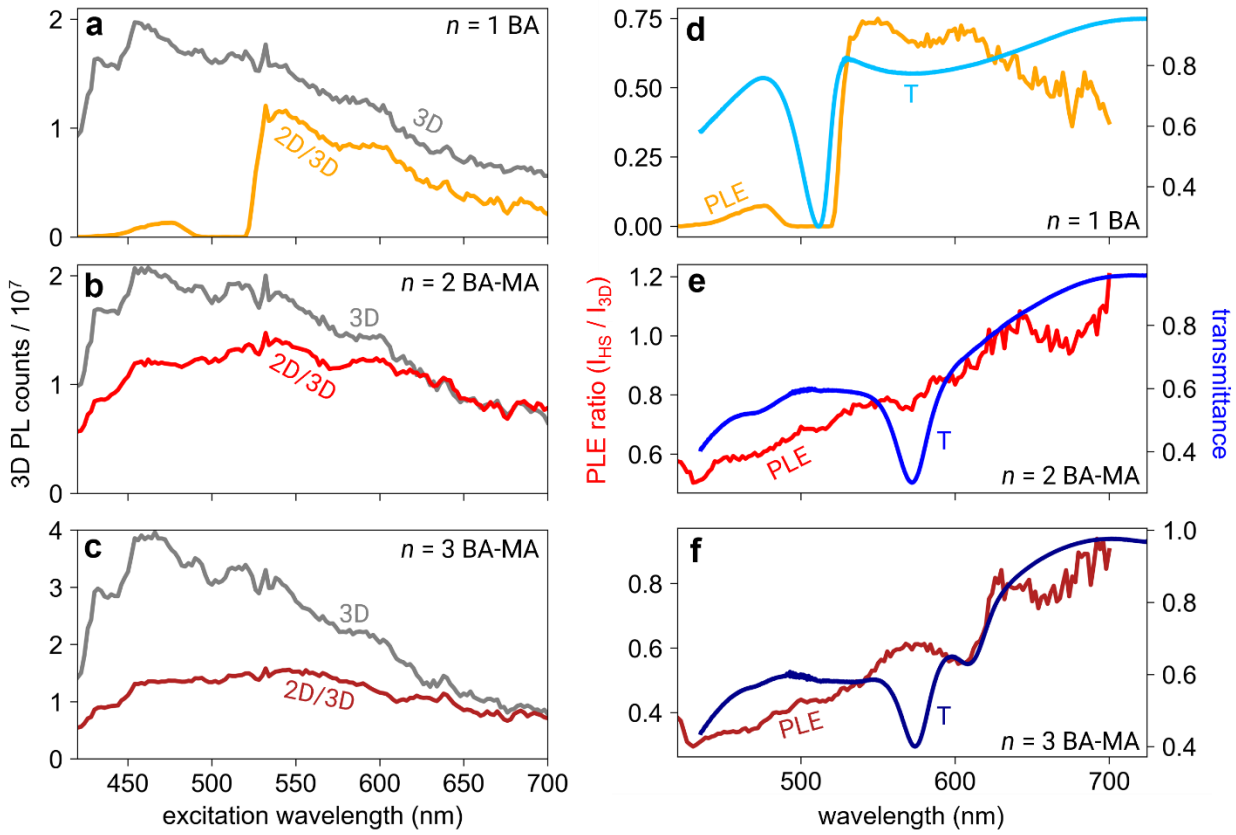

Figure A3.6) Characterization of light attenuation by 2D overlayers. **(a-c)** PLE spectra comparing $(MA)PbI_3$ emission intensity in uncovered vs 2D-covered regions of a common HS: *n* = 1 BA|$MAPbI_3$ **(a)**, *n* = 2 BA-MA|$MAPbI_3$ **(b)**, *n* = 3 BA-MA|$MAPbI_3$ **(c)**. **(d-f)** Ratio of HS vs. bare PLE intensities from a-c compared to transmittance of equivalent 2D LHP microsheets on glass.

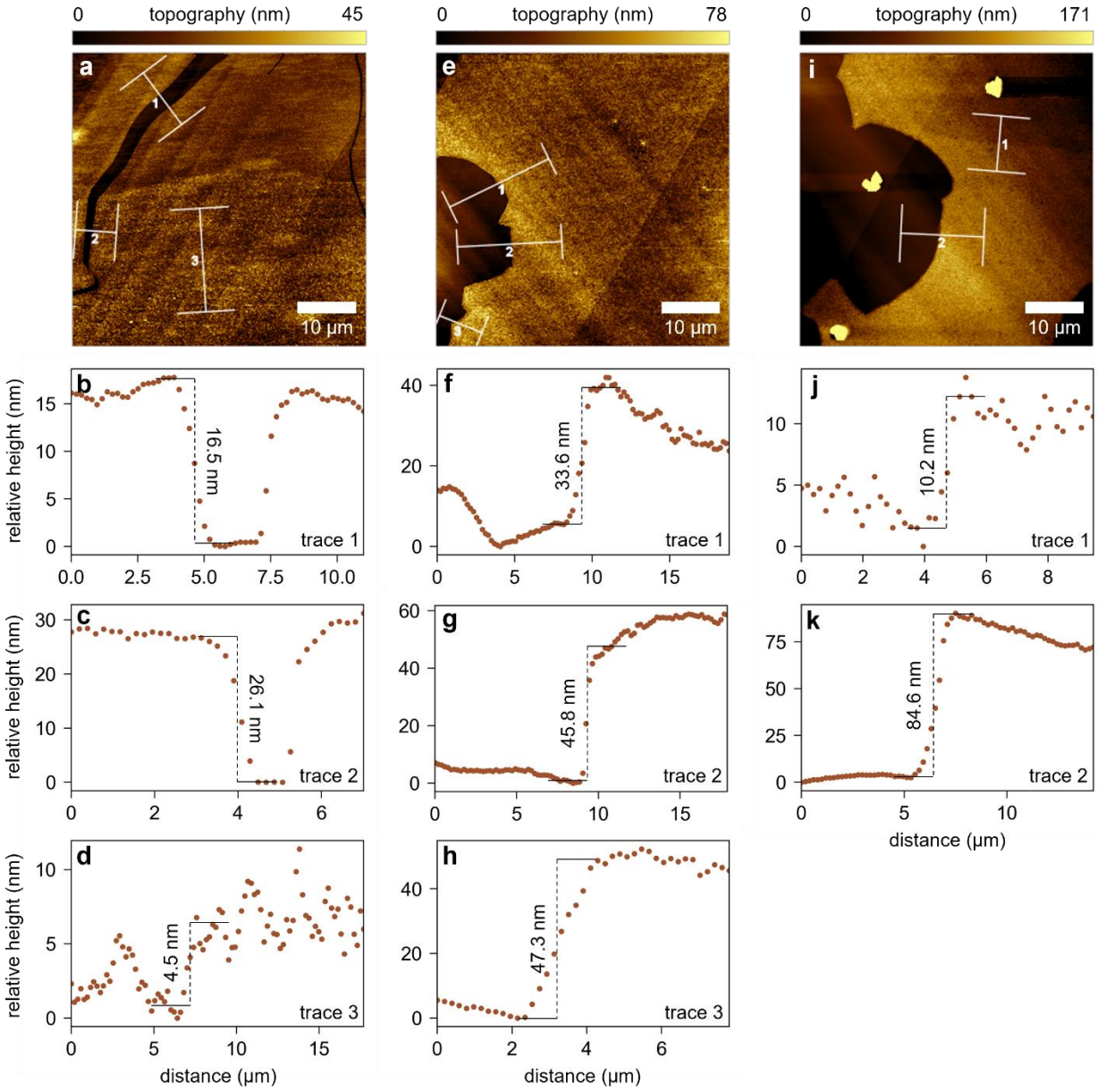

Figure A3.7) Determination of overlayer thicknesses of the $n = 1$ HA|$MAPbI_3$ HS studied in Figure 4.2g,h. **(a,e,i)** AFM topography of multiple 2D terraces on the HS. **(b-d,f-h,j,k)** Topography traces corresponding to the annotations in a **(b-d)**, e **(f-h)**, and i **(j,k)**.

Table A3.3) 2D overlayer thicknesses at each PL measurement point in Figure 4.2g,h, computed from the step heights measured in Figure A3.7.

PL Measurement Point	Overlayer Thickness (nm)	Overlayer Thickness (layers)
1	84.6	52
2	74.4	45
3	47.3	29
4	45.8	28
5	33.6	20
6	30.6	19
7	26.1	16
8	16.5	10

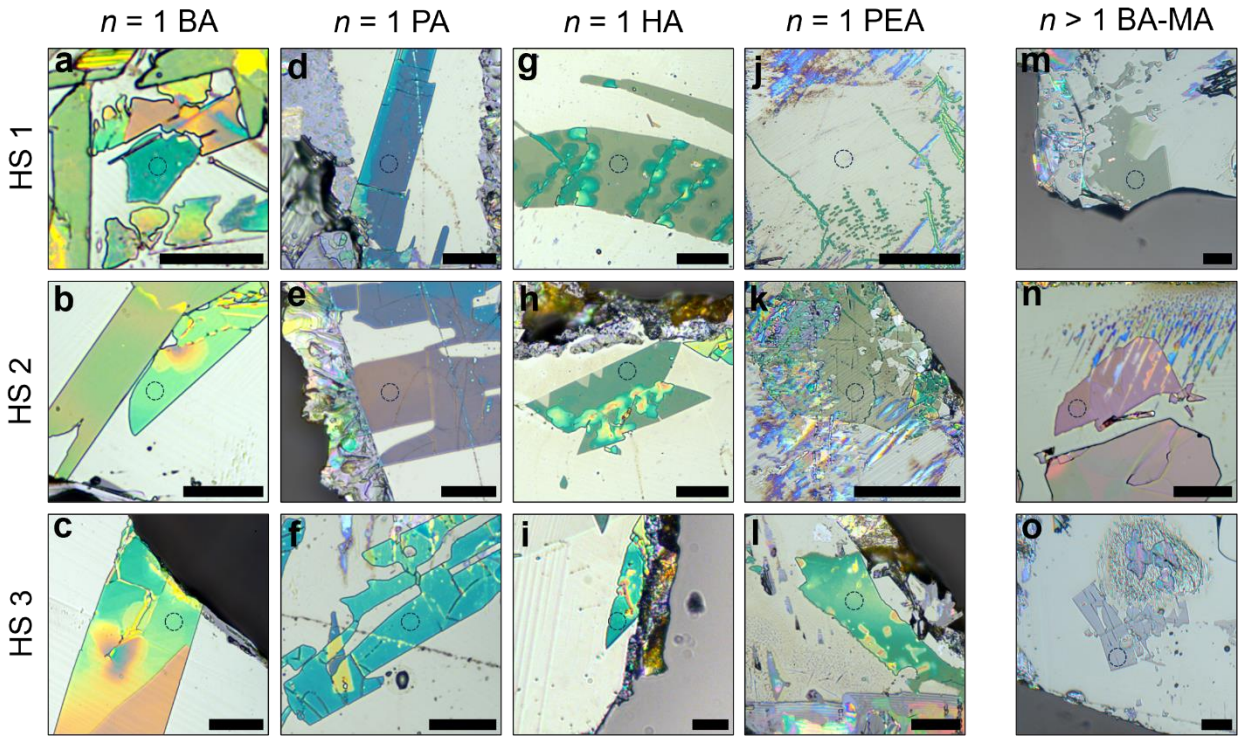

Figure A3.8) Optical microscope images of the 2D/3D HSs studied in the ambient ageing experiments in Figure 4.3 and Figure A3.9. **(a-c)** n = 1 HA|$MAPbI_3$, **(d-f)** n = 1 PA|$MAPbI_3$, **(g-i)** n = 1 HA|$MAPbI_3$, **(j-l)** n = 1 PEA|$MAPbI_3$, **(m-o)** n = 2-4 BA-MA|$MAPbI_3$. All scalebars are 25 μm. Circles indicate the PL measurement point on each HS.

Table A3.4) $<010>_{2D}/<110>_{3D}$ twist angles (measured using facet edges and/or 3D surface striations) for the HSs measured in Figure 4.3 and Figure A3.x.

HS	2D/3D twist angle (deg.)
n = 1 BA|(MA)PbI_3 – HS1	7.3 ± 0.5
n= 1 BA|(MA)PbI_3 – HS 2	3.9 ± 0.5
n= 1 BA|(MA)PbI_3 – HS 3	27.8 ± 0.5
n= 1 HA|(MA)PbI_3 – HS 1	1.2 ± 0.5
n= 1 HA|(MA)PbI_3 – HS 2	34.5 ± 0.5
n= 1 HA|(MA)PbI_3 – HS 3	35.4 ± 0.5
n= 1 PA|(MA)PbI_3 – HS 1	8.5 ± 0.5
n= 1 PA|(MA)PbI_3 – HS 2	42.9 ± 0.5
n= 1 PA|(MA)PbI_3 – HS 3	64.3 ± 0.5
n= 1 PEA|(MA)PbI_3 – HS 1	0.5 ± 0.5
n= 1 PEA|(MA)PbI_3 – HS 2	54.6 ± 0.5
n= 1 PEA|(MA)PbI_3 – HS 3	1.7 ± 0.5

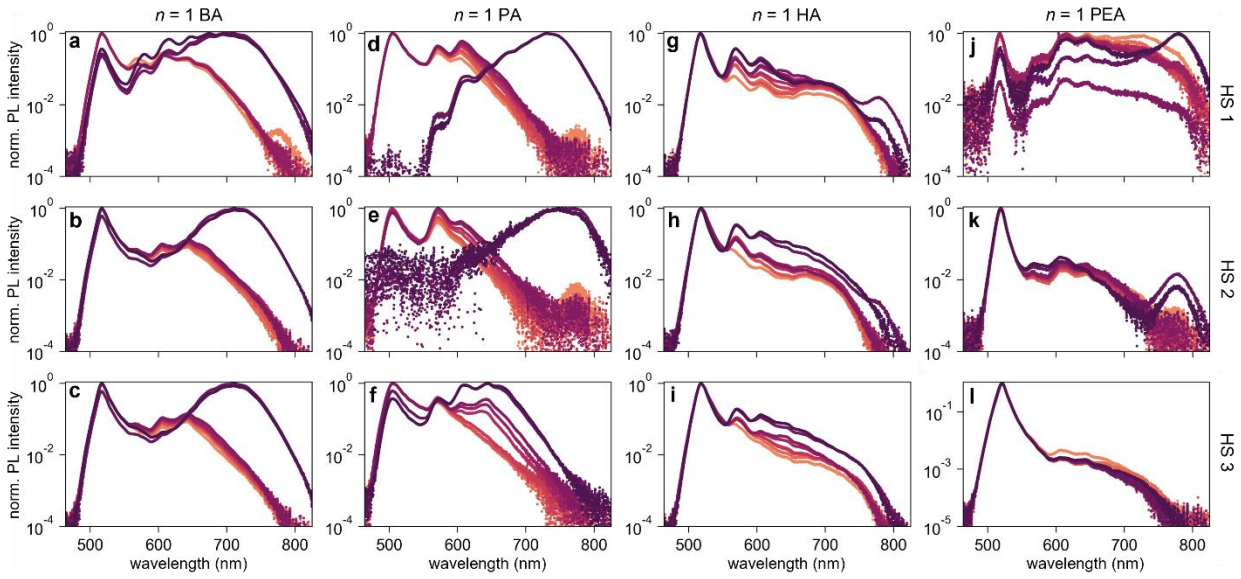

Figure A3.9) All ambient ageing analyses of the n = 1 LA|$MAPbI_3$ HSs depicted in Figure A3.8. **(a-c)** n = 1 HA|$MAPbI_3$, **(d-f)** n = 1 PA|$MAPbI_3$, **(g-i)** n = 1 HA|$MAPbI_3$, **(j-l)** n = 1 PEA|$MAPbI_3$. Line color does not map onto ageing time.

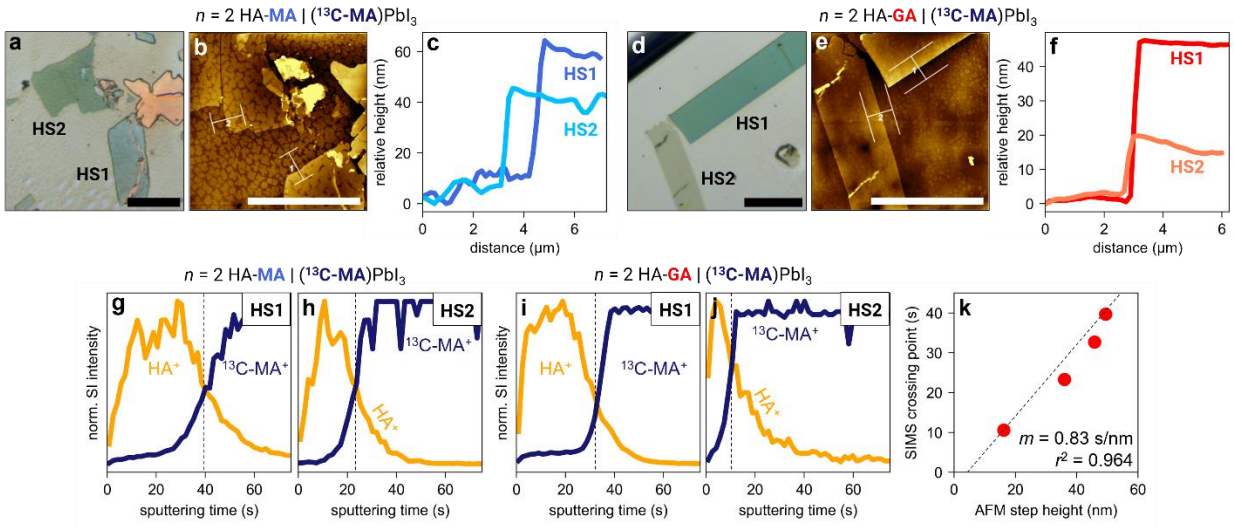

Figure A3.10) Calibration of SIMS sputtering time to true sputtering depth for 2D/3D HSs. **(a-c,d-f)** Optical microscope images **(a,c)**, AFM topography images **(b,e)**, and topography profiles **(c,f)** for control HSs (no accelerated ageing) of n = 2 HA-MA|(^{13}C-MA)PbI$_3$ **(a-c)** and n = 2 HA-MA|(^{13}C-MA)PbI$_3$ **(a-c)** analyzed via SIMS depth profiling. **(g,h,i,j)** SIMS depth profiles of 2D LA and 3D A cations for the HSs shown in (a-c) **(g,h)** and (d-f) **(i,j)**. **(k)** HA$^+$/^{13}C-MA$^+$ crossing point from SIMS depth profiles as a function of step height from AFM topography profiles. The dashed line is best fit (least squares).

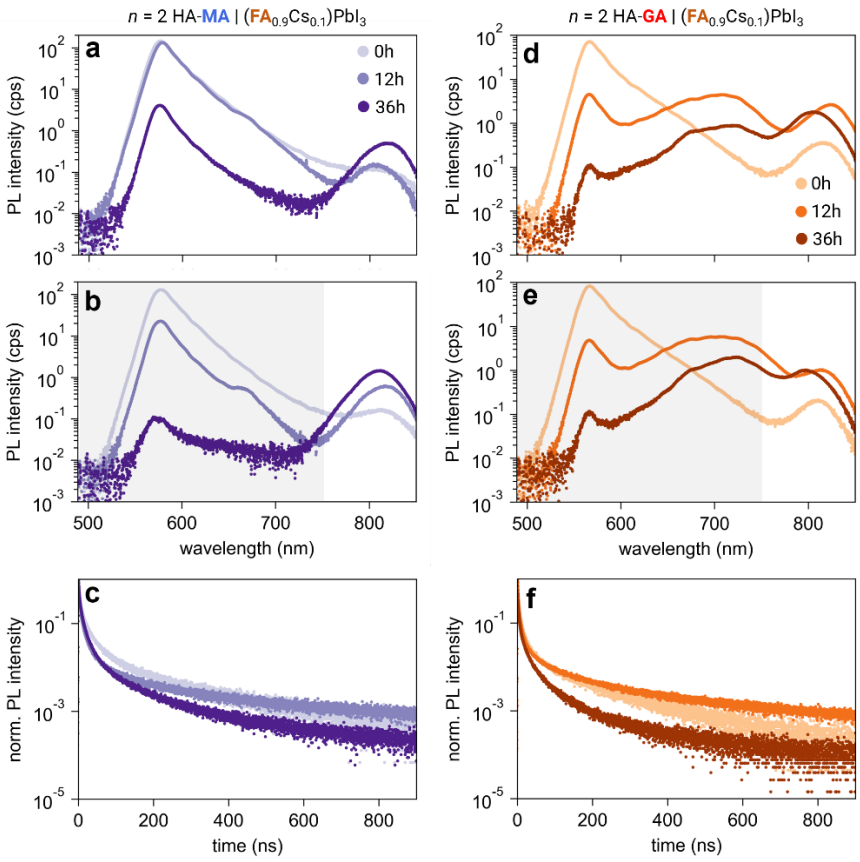

Figure A3.11) PL characterization of $n = 2$ HA-A|$(FA_{0.9}Cs_{0.1})PbI_3$ HSs at different time points under accelerated ageing conditions (65°C, Ar, dark). **(a,b,d,e)** PL spectra of $n = 2$ HA-MA|$(FA_{0.9}Cs_{0.1})PbI_3$ HSs **(a,b)** and $n = 2$ HA-GA|$(FA_{0.9}Cs_{0.1})PbI_3$ **(d,e)** after increasing amounts of accelerated diffusion at 65°C. Tinted regions of (b,e) indicate the range of the spectrum that was blocked for TRPL measurements. **(c,f)** TRPL transients of 3D emission for the HSs in (b,e) after increasing amounts of diffusion at 65°C.

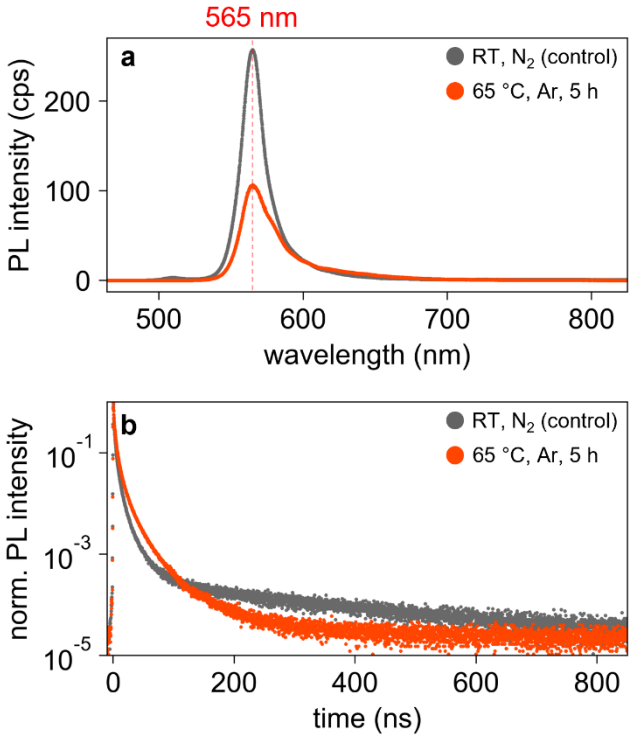

Figure A3.12) (Time-resolved) photoluminescence characterization of $(HA)_2(GA)Pb_2I_7$. PL spectra **(a)** and TRPL transients **(b)** of $n = 2$ HA-GA microplates before and after accelerated ageing.

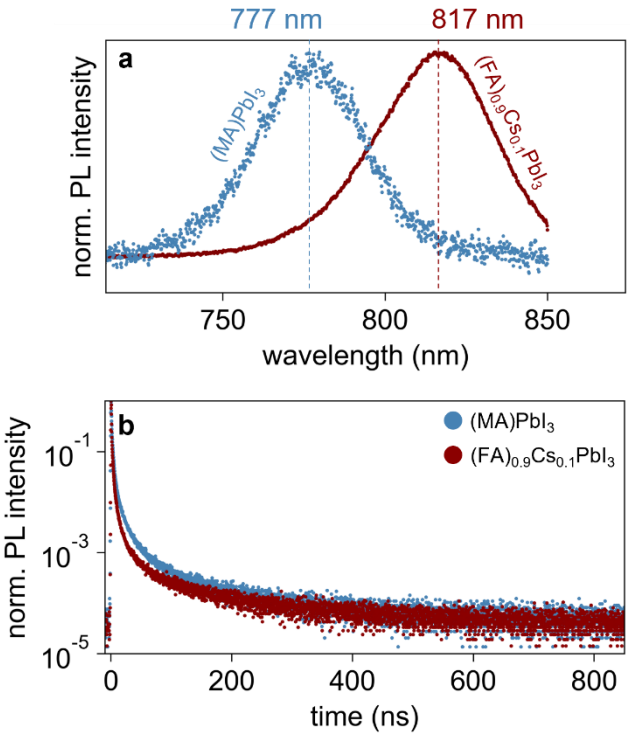

Figure A3.13) (Time-resolved) photoluminescence characterization of the 3D perovskite SCs. **(a)** PL spectra of fresh $MAPbI_3$ and MA-free $(FA_{0.9}Cs_{0.1})PbI_3$. **(b)** TRPL decays of the crystals measured in (a).

A3.3. References

(1) Saidaminov, M. I.; Abdelhady, A. L.; Murali, B.; Alarousu, E.; Burlakov, V. M.; Peng, W.; Dursun, I.; Wang, L.; He, Y.; Maculan, G.; Goriely, A.; Wu, T.; Mohammed, O. F.; Bakr, O. M. High-Quality Bulk Hybrid Perovskite Single Crystals within Minutes by Inverse Temperature Crystallization. *Nat. Commun.* **2015**, *6* (1), 7586.

(2) Chen, Z.; Dong, Q.; Liu, Y.; Bao, C.; Fang, Y.; Lin, Y.; Tang, S.; Wang, Q.; Xiao, X.; Bai, Y.; Deng, Y.; Huang, J. Thin Single Crystal Perovskite Solar Cells to Harvest Below-Bandgap Light Absorption. *Nat. Commun.* **2017**, *8* (1), 1890.

(3) Seed, B. Silanizing Glassware. *Current Protocols in Cell Biology* **2000**, *8* (1), A.3E.1-A.3E.2.

(4) Pan, D.; Fu, Y.; Spitha, N.; Zhao, Y.; Roy, C. R.; Morrow, D. J.; Kohler, D. D.; Wright, J. C.; Jin, S. Deterministic Fabrication of Arbitrary Vertical Heterostructures of Two-Dimensional Ruddlesden–Popper Halide Perovskites. *Nat. Nanotechnol.* **2021**, *16* (2), 159–165.

(5) Roy, C. R.; Pan, D.; Wang, Y.; Hautzinger, M. P.; Zhao, Y.; Wright, J. C.; Zhu, Z.; Jin, S. Anion Exchange of Ruddlesden–Popper Lead Halide Perovskites Produces Stable Lateral Heterostructures. *J. Am. Chem. Soc.* **2021**, *143* (13), 5212–5221.

(6) Spanopoulos, I.; Hadar, I.; Ke, W.; Tu, Q.; Chen, M.; Tsai, H.; He, Y.; Shekhawat, G.; Dravid, V. P.; Wasielewski, M. R.; Mohite, A. D.; Stoumpos, C. C.; Kanatzidis, M. G. Uniaxial Expansion of the 2D Ruddlesden–Popper Perovskite Family for Improved Environmental Stability. *J. Am. Chem. Soc.* **2019**, *141* (13), 5518–5534.

(7) Li, Y.; Zhou, Y.; Guo, W.; Zhang, X.; Huang, Y.; He, E.; Li, R.; Yan, B.; Wang, H.; Mei, F.; Liu, M.; Zhu, Z. Molecular Imaging Reveals Two Distinct Mixing States of PM2.5 Particles Sampled in a Typical Beijing Winter Pollution Case. *Environ. Sci. Technol.* **2023**, *57* (15), 6273–6283.